

INSTITUTO DE QUÍMICA
Programa de Pós-graduação em Química

GABRIEL NEGRÃO MELONI

**Fabrication, characterization and applications of
multifunctional probes for scanning electrochemical
probe microscopy techniques**

Versão original da tese defendida

São Paulo

Data de depósito na SPG:

10 de outubro de 2017

GABRIEL NEGRÃO MELONI

Fabricação, caracterização e aplicação de pontas de prova eletroquímicas multifuncionais para técnicas de microscopia de varredura de ponta de prova eletroquímica

Tese apresentada ao Instituto de Química da Universidade de São Paulo para obtenção de título de Doutor em Ciências (Química)

Orientador: Prof. Dr. Mauro Bertotti

São Paulo - 2017

Ficha Catalográfica
Elaborada pela Divisão de Biblioteca e
Documentação do Conjunto das Químicas da USP

MM528f Meloni, Gabriel Negrão
Fabrication, characterization and applications
of multifunctional probes for scanning
electrochemical probe microscopy techniques /
Gabriel Negrão Meloni. - São Paulo, 2017.
195 p.

Tese (doutorado) - Instituto de Química da
Universidade de São Paulo. Departamento de Química
Fundamental.

Orientador: Bertotti, Mauro

1. Eletroquímica . 2. Microscopia eletroquímica de
varredura. 3. Microeletrodo. 4. Microscopia de
Condutividade Iônica. 5. Nanopipeta. I. T. II.
Bertotti, Mauro, orientador.

Aos meus avós, Walter e Orphila

Aos meus pais Luiza e Luis.

Ao meu irmão Luis.

Ao meu primo Yan.

À minha família.

Abstract

Meloni, G. N. **Fabrication, characterization and applications of multifunctional probes for scanning electrochemical probe microscopy techniques**. 2017. 194p. Thesis (Doctor of Philosophy) - Graduate Program in Chemistry. Instituto de Química, Universidade de São Paulo, São Paulo.

This thesis presents the findings and advances made on fabrication, characterization and application of multifunctional electrochemical probes to acquire space resolved electrochemical information on diverse surfaces/interfaces employing Scanning Electrochemical Probe Microscopy (SEPM) techniques. Different multifunctional probes designs were investigated and new and innovative methods for fabrication and characterization of those probes were developed, which was necessary due to the unconventional nature of most of the probes studied. The benefits of using multifunctional probes for space resolved electrochemical measurements was clear during “proof-of-concept” experiments, where the increased density of information allowed the study of complex systems and the acquisition of topography-free electrochemical information of rough surfaces. The hybridization of different SEPM techniques in a single probe tip was also investigated, and this was found to be extremely beneficial, especially for acquiring high-resolution, topography-free, electrochemical images employing Scanning Ion Conductance Microscopy as a topography feedback. Finally, a new SICM technique, based on the use of a multifunctional probe tip fabricated from a single barrel nanopipette, was developed. This new technique was found to be extremely powerful, capable of acquiring information on topography and map active sites over substrates using a single barrel pipette with high spatial and temporal resolution at a rate of approx. 4000 pixels per second.

Keywords: Microelectrodes, Nanoelectrodes, Scanning Electrochemical Microscopy, Scanning Ion Conductance Microscopy, Nanopipette, SECM, SICM.

Resumo

Meloni, G. N. **Fabricação, caracterização e aplicação de pontas de prova eletroquímicas multifuncionais para técnicas de microscopia de varredura de ponta de prova eletroquímica**. 2017. 194p. Tese (Doutorado) - Programa de Pós-Graduação em Química. Instituto de Química, Universidade de São Paulo, São Paulo.

Esta tese apresenta os achados e avanços obtidos na fabricação, caracterização e aplicação de pontas de prova eletroquímicas multifuncionais para a obtenção de informações eletroquímicas resolvidas no espaço em diversas superfícies/interfaces por meio de técnicas de microscopia de varredura de ponta de prova eletroquímica (SEPM, em inglês). Diferentes designs de pontas de prova multifuncionais foram investigados e, devido a natureza não convencional destas, novos métodos para fabricação e caracterização foram desenvolvidos. Os benefícios da utilização de pontas de prova multifuncionais para a obtenção de informações eletroquímicas resolvidas no espaço ficaram evidente durante a realização de experimentos “prova de conceito”, onde a maior densidade de informação obtida permitiu o estudo de sistemas mais complexos e a aquisição de informações eletroquímicas livre de interferência topográfica mesmo em superfícies não planas. A hibridização de diferentes técnicas de microscopia de varredura de ponta de prova eletroquímica em uma única ponta de prova também foi investigada o que se provou extremamente útil para a aquisição de imagens eletroquímicas de alta resolução, livres de influências topográficas, quando utilizada a técnica de microscopia de condutividade iônica (SICM, em inglês) como sensor de topografia do substrato investigado. Por ultimo, uma nova técnica, baseada na microscopia de condutividade iônica, que se utiliza de pontas de prova eletroquímicas multifuncionais fabricadas a partir de uma nanopipeta de um único canal, foi desenvolvida. Esta nova técnica se mostrou extremamente ponderosa, capaz de obter informações a respeito da topografia e mapear sítios ativos sobre um substrato utilizando uma nanopipeta de um único canal com alta resolução espacial e temporal a uma taxa de aproximadamente 4000 pixels por Segundo.

Palavras-chave: Microeletrodo, Nanoeletrodos, Microscopia Eletroquímica, Microscopia de Condutividade Iônica, Nanopipetas, SECM, SICM

Acknowledgments

I would like to start by apologizing to the possible unadvised reader that dared to go this far and past the cover of this thesis. English, as will be obvious throughout the forthcoming text, is not my mother tongue and as such I am not nearly as fluent in it as I am in Portuguese. As accrediting people who have helped you or somehow favored your achievements is a key aspect of science, a moral duty and, quite honestly, an exercise in humility, I cannot afford any loss of meaning by translation and hence should conduct my acknowledgements in Portuguese. It suffices to say to the English reader that all proper acknowledgments, scientific and, most important, non-scientific are made on the lines that follow. It is an understatement, and paradoxically an overstatement at the same time, to say (borrowing from the great Sir Isaac Newton) that if I have seen further, it is by standing on the shoulders of giants.

Agradeço primeiramente meus pais Luiza e Luís por possibilitarem que eu esteja aqui. Obrigado pelo carinho, pelo amor e pelas infinitas oportunidades que vocês me proveram.

Aos meus avôs Walter, Orphila, Maisa e Luis pelo amor, aconselhamento, criação e por me presentarem com uma maravilhosa família.

A Carla Santana Santos, por ser o mais sincero espelho, minha maior incentivadora e minha maior crítica. Obrigado pelo amor, carinho e companheirismo.

Ao Professor Dr. Mauro Bertotti por todos os (muitos anos) de aconselhamento, convívio e supervisão. Obrigado pelo apoio, direcionamento e ensinamentos.

Ao Professor Dr. Thiago R. L. C. Paixão que, tendo me acolhido e me orientado durante meu estágio de iniciação científica, deve ser considerado o único culpado pela minha permanência e eventual apego à carreira científica. Obrigado pela amizade e pela orientação oficial e extraoficial.

Ao Professor Dr. Patrick Unwin por abrir as portas de seu laboratório e me acolher tanto cientificamente como pessoalmente em seu grupo de pesquisa.

Aos companheiros e ex companheiros do LSEME por todos esses anos de convívio e colaboração. Em especial Carla Santana Santos (novamente), Dr. Alex da Silva Lima, Prof. Dr. Tiago L. Ferreira (Pé) e sua esposa Dra. Helena Junqueira, Prof. Dr. Thiago R. C. L. Paixão (novamente) e sua esposa Profa. Dra. Juliana Naozuka, Profa. Dra. Maiara O. Salles e seu marido Ms. André G. Oliveira e Ms. Victor Ferreira por tornarem até os piores dias de trabalho nos melhores dias de convivência.

Aos companheiros do laboratório LAIA e L₂ESQ, especialmente Ms. André G. Oliveira (novamente), Dr. Eric C. Tavares (Pop), Dr. Fernando Lopes (Fernandinho), Thalita S. Guedes, Dr. Willian R. de Araujo. Prof. Dr. Ivano G. Gutz e Prof. Dr. Claudemir L. do Lago.

Aos amigos de graduação (07.), sou grato por estarem ao meu lado nos anos que precederam e me prepararam para este doutorado. Especialmente Alfredo Bonfá, Dr. Daniel Grasseschi, Dr. José M. C. Junior, Dr. Felipe A. Augusto (Panda, que é 07 sim!).

Aos colegas da gestão de 2009 da A.A.A.A.R.K., fica minha mais profunda gratidão por vestirem a camisa do nosso instituto e embarcarem, sob o meu mais despreparado comando, em um sonho de um IQ melhor.

Aos colegas do Warwick Electrochemistry and Interfaces Group, em especial Dr. Andrew Bassile, Dr. Robert Lazemby and Dr. Minkyong Kang por terem feito um ano passar como se fosse uma semana.

À minha família por opção, meus irmãos e irmãs do colégio São Domingos com os quais convivo (quase) que diariamente pelos últimos 14 anos. Qualquer conquista minha é sem nenhuma dúvida uma conquista de todos vocês. Especialmente André Marchina (Deco), Thiago Picos, Paula Sato (Polly), Julia Sotilli (Loira), Vanessa Lima (Vani), Ricardo Fortunato (Dente), Daniel Pescatore (Bam-bam) e Ricardo Arrojo (Rick).

À minha afilhada Helena Picos (lêle), por me inspirar em ser alguém melhor. Espero que estas simples páginas ajudem a justificar minhas não tão breves ausências.

Aos irmãos do Hermanos de Pelé, por diariamente me ensinarem que futebol nunca foi e nem nunca vai ser apenas um esporte.

À minha família pelo incansável suporte, amor, carinho e dedicação. Por terem aberto tantas oportunidades na minha vida e possibilitado todas as minhas (humildes) conquistas. Sem vocês, eu (literalmente) não estaria aqui.

Ao Instituto de Química da Universidade de São Paulo (IQ-USP) e as agências de foment (CNPq, CAPES e FAPESP) pelo auxílio financeiro e com infraestrutura. Em especial ao CNPq pelas bolsas concedidas de doutorado (48383/2012-2) e estagio no exterior (203506/2014-6).

“Let’s try to teach generosity and altruism, because we are born selfish. Let us understand what our own selfish gene are up to, because we may then at least have the chance to upset their design, something that no other species have ever aspired to.”

Richard Dawkins

Extracted from *The Selfish Gene*

TABLE OF CONTENT

List of Figures	xiv
List of Tables	xxiii
List of Equations	xxiv
Declaration	xxv
Chapter 1. Introduction	1
1.1 Aim of the Thesis	1
1.2 Scanning Electrochemical Probe Microscopy	3
1.3 SEPM techniques operation: behind the curtains.....	6
1.3.1 SECM	6
1.3.2 SICM	16
1.3.3 Multifunctional electrochemical probes and Hybrid techniques.....	24
1.4 SEPM spatial resolution: A tale of probe sizes	29
Chapter 2. Characterization of multifunctional electrochemical probes with nanometer dimensions	34
2.1 Abstract	35
2.2 Introduction	35
2.3 Material and methods	37
2.4 Results	38
2.4.1 Electric conductivity of 3D printed parts	38
2.4.2 3D printed SEM sample holders	41
2.4.3 Nanopipette radius calculation	45
2.4.4 3D printed sample holders durability	47
2.4.5 3D printed sample holders price.....	48
2.5 Conclusion	48
2.6 Acknowledgments.....	48
Chapter 3. Ring-disc microelectrode towards glutathione electrochemical detection	50
3.1 Abstract	51
3.2 Introduction	51
3.3 Material and methods	53
3.3.1 Chemicals	53
3.3.2 instrumentation.....	53
3.3.3 Ring-disc microelectrode fabrication	54
3.4 Results	55
3.4.1 Ring-disc microelectrodes	55
3.4.2 Glutathione detection	58
3.4.3 Space resolved detection	63
3.5 Conclusion	67
3.6 Acknowledgments.....	67
Chapter 4. Controlled Fabrication and Characterization of Multifunctional SEMC-SICM Carbon Nanoprobes for Electrochemical Microscopy	68
4.1 Abstract	70

4.2 Introduction	70
4.3 Materials and methods	73
4.3.1 Chemicals	73
4.3.2 Fabrication of SECM-SICM probes.....	73
4.3.3 Characterization of the SECM-SICM probes.....	74
4.3.4 SECM-SICM instrumentation and imaging technique	75
4.4 Results	76
4.4.1 SECM-SICM probe fabrication	76
4.4.2 Electrochemical characterization and imaging	81
4.5 Conclusions	84
4.6 Acknowledgments.....	85
Chapter 5. Multifunctional electrochemical probe at a single barrel nanopipette	86
5.1 Abstract	88
5.2 Introduction	89
5.3 Materials and methods	91
5.3.1 Chemicals	91
5.3.2 Nanopipette probes.....	91
5.3.3 Scanning ion conductance microscopy (SICM) setup	91
5.3.4 Numerical simulations.....	92
5.4 Results	93
5.4.1 Operational principles	93
5.4.2 Electrical setup configuration and influence of substrate size	96
5.4.3 Measurements near active reaction sites	98
5.4.4 Dynamic Voltammetric Imaging.....	102
5.4.5 Effects of nanopipette tip on measured substrate current	106
5.4.6 High-Speed Imaging	107
5.5 Conclusions	111
5.6 Acknowledgments.....	112
Appendix.....	113
A1. Building a Microcontroller based potentiostat: An Inexpensive and versatile platform for teaching electrochemistry and instrumentation.	115
A1.1 Abstract	115
A1.2 Introduction	115
A1.3 Materials and methods	116
A1.3.1 Potentiostat fabrication.....	116
A1.3.2 Power supply	119
A1.3.3 Digital to analog converter (DAC).....	119
A1.3.4 Scan rate	121
A1.3.5 Analog to digital converter (ADC).....	122
A1.4 Results	124
A1.4.1 Resistors polarization curve	124
A1.4.2 Diffusion coefficient determination	125
A1.5 Conclusion.....	126
A1.6 Acknowledgments.....	127

A2. 3D printed and Microcontrolled: The one hundred dollars Scanning Electrochemical Microscope	128
A2.1 Abstract	128
A2.2 Introduction	129
A2.3 Materials and methods	130
A2.3.1 Chemicals	130
A2.3.2 3D printed parts	131
A2.3.3 Electrochemical measurements	131
A2.3.4 EC-SPM electronics construction	133
A2.3.5 Potentiostat specifications	136
A2.3.6 EC-SPM mechanical construction.....	137
A2.3.7 Tip positioning control	137
A2.3.8 Software.....	138
A2.4 Results	139
A2.4.1 Electrochemical measurements using microelectrodes	139
A2.4.2 Space resolved electrochemical measurements.....	140
A2.5 Conclusions	147
A2.6 Acknowledgments	147
Summary	148
Curriculum Vitae.....	151
References.....	159

List of Figures

Figure 1.1. Schematic representation of generic SEPM equipment used to probe substrates (surfaces/interfaces) showing its principal components: Potentiostat, electrochemical probe, investigated substrate and positioning system. QRCE stands for Quasi-Reference Counter Electrode.....	4
Figure 1.2. Optical microscopy image (top view) of a 15 μm diameter platinum microelectrode encapsulated on a quartz capillary.....	7
Figure 1.3. Schematic representation of a cross section view of a microelectrode showing the radius of the insulating glass and the radius of the electrodic surface. The ratio of these radius is known as RG	8
Figure 1.4. Representation of the influence of the electrode RG on the diffusion of species towards the electrodic surface. (Left) No back diffusion is observed. (Right) Back diffusion is observed.....	10
Figure 1.5. Representation of a biased microelectrode on a solution bath at bulk solution and in close proximity to a substrate.....	11
Figure 1.6. (Left) Simulated data for approach curves of a properly biased microelectrode towards substrates with different rate constants. Constant values ranging from 10^{-4} to 10^2cm.s^{-1} . $RG = 10$. (Right) Simulated data for approach curves towards an “insulator” substrate with microelectrodes of different RG values. RG values ranging from 50 to 1.5. I_{Bulk} is the current recorded at the electrode at bulk solution (without interference of the substrate). d is the microelectrode/substrate distance and r the electrodes radius.....	13
Figure 1.7. Impact of electrode RG on the minimal working distance for an electrode approaching towards the substrate at a slight angle θ (exaggerated).....	15
Figure 1.8. Schematic representation of (Left) Substrate Generation/Tip Collection and (Right) Tip Generation/Substrate Collection SECM S/G modes.	16
Figure 1.9. Representation of a pipette (sliced along its main axis) and typical SICM setup showing important pipette geometry parameter such as the opening radius (r_i), outer tip radius (r_o) tip base radius (r_p), pipette inner semi cone angle (β), and taper length (h).	18

Figure 1.10. Representation of the equivalent circuit for the current flow through a pipette (left) at a bulk solution and (right) close to a substrate.....	20
Figure 1.11. Simulated SICM normalized approach curves for (Left) different pipette RG values (1.3,2,3,5 and10) and (Right) different pipette inner semi-cone angle, β ($1^\circ, 5^\circ, 10$ and 15°). L is the normalized pipette/substrate distance (d/r_i) and i_{norm} is the normalized ionic current (i/i_{max}).....	21
Figure 1.12. Electron transmission images of the side of a nanopipette showing opening diameter and wall thickness. $RG = 1.3$. Accelerating Voltage= 12 kV.	22
Figure 1.13. Schematic representation of an amplitude modulated SICM experiment showing the pipette vertical oscillation (z axis) and the corresponding approach curves for the direct (i_{DC}) and alternated (i_{AC}) components of the recorded current. d is the pipette/substrate separation and r the pipette radius.....	23
Figure 1.14. Representation of (Top) electrochemical probes for SECM and SICM and (Bottom) multifunctional electrochemical probes highlighting the nature of the electrochemical information recorded.	26
Figure 1.15. Fabrication procedure for double-barrel carbon SECM-SICM multifunctional electrochemical probes.	27
Figure 1.16. Photos of the same object and with same dimension for different pixel densities (pixel size) expressed in dots per inch (dpi).	31
Figure 1.17. On the left, photographs of the same object reproduced at two different pixel densities 10 dpi (top) and 100 dpi (Bottom). On the right, expanded fragment (with the same area) of both photos illustrating the difference in density of information (in this case in the red chromaticity channel).	32
Figure 1.18. Light spot size and brightness dependence on the separation between the flashlight and a substrate (d), which is analogous to the spot size and current contrast dependence on the working distance in SEPM.....	33
Figure 2.1. Schematic representation of the 3D printed 1 cm^3 test pieces. (a) Representation of a test piece with an open top showing the internal infill geometry. (b) Schematic representation of the printing path during the printing of the test pieces, highlighting the staggered layers. (c) Different pairs of opposite faces whose orientation regarding the internal infill geometry are shown in blue.....	40

Figure 2.2. 3D printed test pieces with different infill percentages for electrical resistivity calculation showing faces painted with conductive silver ink to avoid contact resistance on (a) faces perpendicular to the printed layers and (b) face parallel to the printing layers. (c) setup for connecting the test pieces to a potentiostat to measure the electrical resistivity. Copper sheets act as a contact between the silver painted faces and the potentiostat. Spring clamp ensures constant pressure on the aces during all the measurements.41

Figure 2.3. (a) and (b) custom designed 3D printed conductive 45° SEM sample holder for UME and nanopipettes. Nanopipettes attached using conductive carbon tape. (c) Couple of custom designed and 3D printed SEM sample holders showing specific features for holding UMEs and nanopipettes.....43

Figure 2.4. SEM images of nanopipettes and nanoelectrodes. (a) and (b) top view of a double barrel pipette showing both openings unblocked. (c) Side view of a double barrel pipette. (d) Top view of a dual-function pipette based electrode showing selective carbon deposition in only one barrel. Accelerating voltage = 5 kV.44

Figure 2.5. (a) and (b) SEM images of a 300 nm alumina powder used for polishing electrodes at different magnification. (c) Close-up of a single particle cluster showing the details of the particle surface. (d) 3D printed SEM stub sample holders used for acquiring the alumina powder images. Accelerating voltage = 3kV.45

Figure 2.6. (a) Representation of a cross section of a nanopipette showing the opening radius and the inner semi cone angle, β . (b) Polarization curves recorded with 5 different nanopipettes in a 0.1 mol L⁻¹ KCl solution using a pair of AgCl coated silver wires as Quasi-reference counter electrodes (QRCE). Scan rate = 0.1 V s⁻¹. (c) Transmission-SEM image of a nanopipette. Accelerating voltage = 15 kV.46

Figure 3.1. Ring-disc microelectrode fabrication process (A). Optical microscopy image (B) and SEM image (C) of the ring-disc microelectrode fabricated by the proposed method.56

Figure 3.2. Generation/Collection experiment recorded with a ring-disc microelectrode in a 15 mmol L⁻¹ potassium ferricyanide + 0.1 mol L⁻¹ KCl solution with the microelectrode positioned at (a) the bulk solution and (b) at 5 μm from an inert substrate. Potential scanned at the disc in the range 0.5 to -0.2 V. Ring polarized at 0.5 V. Scan rate: 5 mV s⁻¹.58

Figure 3.3. SECM DG/RC collection efficiency values at different tip-substrate separations. Experiments were carried out in 15 mmol L ⁻¹ potassium ferricyanide + 0.1 mol L ⁻¹ KCl solution. $E_{disc} = -0.1$ V, $E_{ring} = 0.5$ V.....	59
Figure 3.4. Schematic representation of the indirect detection of GSH at a ring-disc microelectrode positioned over an inert substrate. Tip-substrate separation denoted as “d” on the representation.	60
Figure 3.5. (A) Collection current recorded at the ring as a function of GSH concentration for two different tip-substrate separation values: (i) 30 and (ii) 5 μm. $E_{disc} = 0.9$ V, $E_{ring} = -0.2$ V. (B) Collection current recorded at the disc vs. GSH concentration in experiments performed with the tip far from the substrate. $E_{disc} = -0.2$ V, $E_{ring} = 0.9$ V. Experiments performed in a 1 mmol L ⁻¹ APAP + 10 mmol L ⁻¹ PBS solution (pH 7.4).....	62
Figure 3.6. Normalized approach curve recorded in 1 mmol L ⁻¹ APAP + 10 mmol L ⁻¹ PBS solution. Dots: In presence of GSH 50 mmol L ⁻¹ and absence of GSH. Both data are superimposed. Black line: Theoretical curve. $E_{disc} = 0.9$ V. Radius of the microelectrode, $a = 12.5$ μm.....	65
Figure 3.7: (A) Schematic drawing of the electrochemical cell used during the electrochemical imaging experiments showing the separated compartments and the separating membrane. Electrochemical image of GSH transport across an orifice in the separating membrane showing normalized ring current (B) and normalized collection efficiency (C); $E_{disc} = 0.9$ V, $E_{ring} = -0.2$ V.....	67
Figure 4.1. Schematic of the setup used to fabricate pyrolytically deposited carbon electrodes showing: (a) side view representation of the coil carriage assembly (heating coil, servomotor and thermocouple sensor) and (b) coil movement through the pipet (from position 1 to 2), showing argon and butane gas inlets and a carbon plug deposited in one barrel only.....	73
Figure 4.2. TEM images to show common problems faced when using poor control of the heat source. (a) Misshapen tip geometry and reduced tip diameter as a consequence of partial melting of the pipet quartz body. (b) Blocked tip due to complete melting of the pipet quartz body. (c) Carbon layer recession in the order of micrometers.	76
Figure 4.3. TEM images to effect of temperature and deposition time on carbon pyrolysis. (a) Hollow profile ($T_p = 750$ °C, $t_p = 250$ s). (b) Completely filled carbon	

barrel and an unblocked SICM barrel ($T_p = 800\text{ }^\circ\text{C}$, $t_p = 200\text{ s}$). (c) Recession cavity caused by carbon oxidation due to high pyrolysis temperature and time ($T_p = 800\text{ }^\circ\text{C}$, $t_p = 300\text{ s}$).....77.

Figure 4.4. TEM image (a) and Raman spectrum (b) of the SECM-SICM probe made using a lower T_p . TEM image (a) and Raman spectrum (b) of the SECM-SICM probe made using a higher T_p78

Figure 4.5. Histogram showing the distribution of carbon layer recession of carbon nanoprobe fabricated by two methods: the manual blow torch method (■), as described by Takahashi et al., and the “heating coil method” (■) as described in this manuscript80

Figure 4.6. Electrochemical characterization of the fabricated probes in 2 mM ruthenium hexamine chloride, 0.1 M KCl solution. (a) Cyclic voltammogram performed on the SICM barrel, at 100 mV s^{-1} scan rate. (b) Cyclic voltammogram performed on the carbon filed barrel, at 100 mV s^{-1} scan rate. (c) Topographic image (SICM) and (d) electrochemical (SECM) image of Pt UME ($d = \sim 2\text{ }\mu\text{m}$). Pixel size = $100 \times 100\text{ nm}$81

Figure 4.7. (Dots) Voltammogram performed on the Carbon filled barrel, at 100 mV s^{-1} scan rate. (Solid line) Simulation using the DigiElch software for an 83 nm radius electrode and a standard rate constant (k^0) of 1.7 cm s^{-1} . 2 mM ruthenium hexamine chloride, 0.1 M KCl solution82

Figure 4.8. Optical image of a Multifunctional SECM-SICM electrochemical probe approaching a $2\text{ }\mu\text{m}$ radius platinum microelectrode substrate for the experiments portrayed on Figure 4.683

Figure 5.1. a) Schematic representation of the experimental setup for reaction mapping with SICM. b), c) TEM images of nanopipette probes of $\sim 200\text{ nm}$ and $\sim 100\text{ nm}$ opening radius, respectively.....94

Figure 5.2. Electrical circuit representation of the SICM setup used for mapping reactions. Gray line indicates additional parts of the circuit (compared to classical SICM) for the control of substrate potential.96

Figure 5.3. Probing the diffusion (concentration-boundary) layer with a nanopipette. a) Schematic representation of the ion redistribution at the diffusion layer of generated Fc^+ adjacent to an Au UME. b), c) Experimental (red and blue traces) and simulated (solid black lines) SICM current-distance curves acquired with a nanopipette (biased at

-0.1 and +0.1 V, respectively) positioned over an inert (blue) and Fc^+ generating (diffusion-controlled rate) 12.5 μm radius Au UME (red). Experimental conditions (1.95 mM and 1.45 mM Fc for (b) and (c), with 10 mM KNO_3 in bulk solution, and nanopipettes of 175 nm opening radii as determined by TEM) were mimicked in the simulation with the best fit with an f parameter of 0.925. d) Experimental (red, reaction on, and blue, reaction off) and theoretical (black and red dashed lines) AC amplitude – distance relationships for a nanopipette positioned over an inert and Fc^+ generating UME. Note that the theoretical curves with the electrode on and off essentially coincide. e), f) Simulated conductivity distributions (magnified view) with a nanopipette (biased at ± 0.1 V) positioned at 1 μm distance from an Fc^+ generating substrate electrode (Au UME)98

Figure 5.4. Dynamic reaction imaging with SICM. a) Schematic representation of the experimental setup employed for mapping hydrazine oxidation and proton reduction at ~ 600 nm radius Pt UME. b) Topography map (45 by 45 pixels, 125 nm step size) during a hopping scan. The nanopipette, biased at -0.25 V, was approached to the substrate (held at -0.2 V vs Ag/AgCl QRCE in bulk) at every pixel at a speed of 250 nm s^{-1} and then retracted by 1 μm before being repositioned above the next location. c) Substrate (red) and nanopipette probe (blue) voltammograms acquired with the nanopipette at the central part of the substrate electrode during the potential sweep at the Pt UME (-1.2 V to 0.75 V) at a scan rate 0.5 V s^{-1} . The electrolyte solution contained hydrazine sulphate $\text{N}_2\text{H}_4 \cdot \text{H}_2\text{SO}_4$ and KNO_3 at 20.5 mM and 10 mM, respectively. The arrows on the graph indicate the direction of the potential sweep. d) EC images (6 frames) from a 380-snapshot image sequence, constructed from a voltammetric data resolved at each image pixel. The nanopipette current has been normalized by the value at the point of the closest approach (at each individual pixel) with the substrate potential held at -0.2 V.103

Figure 5.5. The effect of a nanopipette tip on the mass-transport at the substrate. Maps of a) normalized tip current and b) corresponding map of substrate current as a function of nanopipette position at 0.75 V (mass transport-limited hydrazine oxidation. c) Substrate current profiles extracted from substrate current map at positions indicated by dashed lines in b).106

Figure 5.6. The relationship between the normalized current at 600 nm radius disk UME and the tip/substrate distance (nanopipette radius 200 nm).107

Figure 5.7. a) High-speed electrochemical imaging of reactions with SICM. a) Electrochemical image of ~ 430 nm radius Pt UME (held at 0.4 V) recorded with a ~ 95 nm radius nanopipette biased at -0.25 V vs QRCE in bulk solution during a topographical prescan at $5.2 \mu\text{m s}^{-1}$ in electrolyte solution containing 2 mM FcTMA^+ (diffusion-limited oxidation) and 10 mM KNO_3 . b) A set of high speed images constructed from both forward and reverse scans (for improved image quality) recorded at $180 \mu\text{m s}^{-1}$ probe translational speed at different substrate potentials. The probe currents are normalized with respect to the average ion current for every snapshot. c) Nanopipette current profiles (along the dashed white line on the images) depicting the comparison between high-speed (red) and slow prescan (blue) imaging of diffusion-controlled FcTMA^+ oxidation (substrate held at 0.4 V). d) Normalized tip current profiles, demonstrating the effect of the substrate potential on the normalized tip current. Red, green, blue and black lines correspond to substrate electrode potentials of 4, 52, 76 and 400 mV vs QRCE in solution bulk, respectively. White dashed line on a) and b) denotes the position of the current profiles shown on c) and d). Scale bar $2 \mu\text{m}$. Note, the current data was smoothened using Gaussian filter.109

Figure A1.1. i) Possible construction of the device using a custom etched printed circuit board ii) Analog circuit of the potentiostat with highlighted A: summing amplifier; B: electrochemical cell and electrochemical cell potential controlling amplifier; and C: transimpedance amplifier (current to voltage converter)117

Figure A1.2. Pictures of the device used on the experiments showing its breadboard construction. Highlighted are the jumper wire connections to the ADC and DAC (top left image) and to the reference, counter and working electrodes (bottom left picture)118

Figure A1.3. Full schematic design of the potentiostat including the Arduino board pin connections118

Figure A1.4. E vs. t plot of the DAC output (black line) and summing amplifier output (grey line)121

Figure A1.5. Dots: Polarization curves for A: $1 \text{ k}\Omega$ resistor, B1: $10 \text{ k}\Omega$ resistor, and B2: $5 \text{ k}\Omega$ parallel resistor association. Line: Linear fit for the obtained curves with $R^2 = 0.9996, 0.9984, \text{ and } 0.9933$ for $1 \text{ k}\Omega, 5 \text{ k}\Omega, \text{ and } 10 \text{ k}\Omega$, respectively124

Figure A1.6. Cyclic voltammogram recorded on a platinum working electrode in 19.35 mM potassium ferricyanide in 0.1 M potassium chloride solution with scan rates of 0.01

Vs^{-1} , $0.02 Vs^{-1}$, $0.05 Vs^{-1}$, $0.10 Vs^{-1}$, $0.20 Vs^{-1}$, $0.25 Vs^{-1}$, and $0.30 Vs^{-1}$. Inset B: Linear fit of the anodic peak currents against the square root of the scan rate126

Figure A2.1. Diagram of the principal electronic components of the proposed EC-SPM setup showing the microcontroller board connected to the custom built potentiostat and to the “off-the-shelf” stepper controller boards used to fine control the linear stages during space-resolved electrochemical experiments. Highlighted are (A) the summing amplifier, (B) potential control circuit and electrochemical cell and (C) transimpedance amplifier of the custom built potentiostat132

Figure A2.2. Multiple pictures of the proposed potentiostat design fabricated using a custom etched PCB showing the current shields (small PCBs) that allow for fast and easy change of the current limits134

Figure A2.3. Photos of the potentiostat shield and current shield PCBs with component labels without any component solder. Red rectangles correspond to the connection site between the two shields135

Figure A2.4. Pictures of two 3D printed linear stages fully assembled showing the placement of the electrochemical cell and the 3D printed UME holder137

Figure A2.5. Exploded and assemble views of the linear stages used during SECM experiments showing both the 3D printed and “off-the-shelf” parts. Assembled view shows the 2-axes setup used during the SECM experiments138

Figure A2.6. (A) Cyclic voltammograms recorded using the proposed equipment. Red and black dots represent two different cycles, before and after the approach curves. Scan rate = $50 mV.s^{-1}$ (B) Normalized approach curve recorded over an insulating substrate. Black dots: approaching the substrate. Red dots: retracting from the substrate. Black line: theoretical curve. $E_{tip} = -0.2V$. Step = $2 \mu m$. All experiments performed in $200 mmol.L^{-1}$ potassium ferricyanide solution using a $15 \mu m$ diameter platinum UME as the working electrode and a Ag/AgCl QRCE.....142

Figure A2.7. (A) Schematic representation of the substrate (attached to the electrochemical cell bottom) showing the insulating substrate and the polyimide tape step. Arrows indicate the scanning direction over the step edge. (B) Line scans performed up to the step edge. (C) Line scans performed down the step edge. Scans were performed in duplicate (red and black dots) using a $50 mmolL^{-1}$ MV solution. $E_{tip} = -0.9 V$, Step = $10 \mu m$, Scan speed = $10 \mu ms^{-1}$ 143

Figure A2.8. (A) Representation of the electrode “hopping” path (blue dotted line) across the substrate step edge. (B) Resulting current map obtained during the array scan over the zx plane. (C) Line scans across the substrate step edge recovered from the current map data at two distinct tip heights (tip separation from the polyimide step), (i) $12\ \mu\text{m}$ and (ii) $24\ \mu\text{m}$. $E_{\text{tip}} = -0.9\text{V}$, Pixel size = $12\ \mu\text{m} \times 12\ \mu\text{m}$, Scan speed = $12\ \mu\text{m s}^{-1}$ 145

List of Tables

Table 1.1. “X” value for common used electrode RGs.....	10
Table 2.1. Electrical resistivity measured in 3D printed 1 cm ³ test pieces with different infill percentages. Measurements were taken between different faces of the cubes.....	41
Table A1.1. Truth table for the summing amplifier, showing its voltage output as a function of the DAC voltage/PWM level	120
Table A1.2. Truth table of the current to voltage converter, showing its voltage output and ADC level as a function of the current flowing through the counter electrode.....	123
Table A1.3. Component values used during the electrochemical experiments on the main manuscript. Components are labeled as on Figure A1.3	123
Table A1.4. Current and voltage limits for the potentiostat used during the experiments performed in the main manuscript	123
Table A2.1. Resistance values for R ₅ , R ₆ , and voltage divider resistors and the resulting voltage divider voltage for different current limits. Values are the expected on the Arduino sketch on Section SI-5.....	135
Table A2.2. Current, voltage and scan rate limits for the potentiostat used during the experiments performed in the main manuscript	136
Table A2.3. Component values used during the electrochemical experiments on the main manuscript. Components are labelled as on Figure A2.1	136

List of Equations

<i>Equation 1.1. Current at diffusion limiting conditions for a disk microelectrode embedded into an infinite thick insulator</i>	<i>8</i>
<i>Equation 1.2. General equation for the current at diffusion limiting conditions for a disk microelectrode accounting for back diffusion.....</i>	<i>9</i>
<i>Equation 1.3. Analytical approximation for the value of the X constant with regard to the RG value</i>	<i>10</i>
<i>Equation 1.4. Pipette opening resistance</i>	<i>18</i>
<i>Equation 1.5. Current due to the ionic flow through a pipette opening in function of the bias potential</i>	<i>18</i>
<i>Equation 1.6. Analytical approximation for the ionic current during a SICM approach curve</i>	<i>19</i>
<i>Equation 1.7. Analytical approximation for the ionic current during a SICM approach curve taking in account the influence of the pipette geometry</i>	<i>20</i>
<i>Equation 2.1. Pipette access resistance as a function of pipette geometry</i>	<i>45</i>
<i>Equation 5.1. Pipette current as a function of the equivalent circuit components on Figure 5.2</i>	<i>96</i>
<i>Equation A1.1. Summing amplifier output voltage.....</i>	<i>121</i>
<i>Equation A1.2. Maximum scan rate</i>	<i>122</i>
<i>Equation A1.3. Current to voltage converter output voltage</i>	<i>122</i>
<i>Equation A1.4. Randles-Sevick equation.....</i>	<i>125</i>
<i>Equation A2.1. Summing amplifier output voltage accounting for the bias potential</i>	<i>133</i>

Declaration

The work presented in this thesis is entirely original and my own work, excepted when acknowledged in the text. All supporting authors and fellows who contributed to the work herein presented are duly acknowledged and/or properly identified as authors. I confirm that this thesis has not been submitted for a degree at another University. This work is being submitted for thesis by publication.

Chapter 2 was published as:

3D printing scanning electron microscopy sample holders: A quick and cost effective alternative for custom holder fabrication

Meloni, G. N.; Bertotti, M. *PLoS One* **2017**, *12* (7)

Chapter 3 was published as:

Ring-disc Microelectrodes towards Glutathione Electrochemical Detection

Meloni, G. N.; Bertotti, M. *Electroanalysis* **2016**, 1–8.

Chapter 4 is in preparation and *will be* submitted to *Anal. Chem.* as:

Controlled Fabrication and Characterization of Carbon Nanoprobes for Electrochemical Microscopy

Meloni, G. N.; Kang, M.; Lazenby, R. L.; Ravenhill, E.; Unwin, R. P. *Anal. Chem.* **2017**

Chapter 5 was published as:

Simultaneous Interfacial Reactivity and Topography Mapping with Scanning Ion Conductance Microscopy

Momotenko, D.; McKelvey, K.; Kang, M.; **Meloni, G. N.**; Unwin, P. R. *Anal. Chem.* **2016**, *88* (5), 2838–2846. Parts of this manuscript also are featured on Minkyong Kang's thesis as she actively participated on the manuscript elaboration.

Appendix 1 was published as:

Building a Microcontroller Based Potentiostat: A Inexpensive and Versatile Platform for Teaching Electrochemistry and Instrumentation

Meloni, G. N. *J. Chem. Educ.* **016**, *93* (7), 1320–1322.

Appendix 2 was published as:

3D Printed and Microcontrolled: The One Hundred Dollars Scanning Electrochemical Microscope

Meloni, G. N. *Anal. Chem.* **2017**, *89* (17), 8643–8649.

Additionally, I have contributed to the following papers whose results are not presented in this thesis:

Determination of Paracetamol in Presence of Ascorbic Acid in Pharmaceutical Products by Scanning Electrochemical Microscopy

Lima, A. S.; Meloni, G. N.; Bertotti, M. *Electroanalysis* **2013**, 25 (6), 1395–1399.

Explosive colorimetric discrimination using a smartphone, paper device and chemometrical approach

Salles, M. O.; Meloni, G. N.; de Araujo, W. R.; Paixão, T. R. L. C. *Anal. Methods* **2014**, 6 (7), 2047–2052.

Use of plastic-based analytical device, smartphone and chemometric tools to discriminate amines

Bueno, L.; Meloni, G. N.; Reddy, S. M.; Paixão, T. R. L. C. *RSC Adv.* **2015**, 5 (26), 20148–20154.

Synthesis and Characterization of ZrO₂/C as Electrocatalyst for Oxygen Reduction to H₂O₂

Carneiro, J. F.; Trevelin, L. C.; Lima, A. S.; Meloni, G. N.; Bertotti, M.; Hammer, P.; Bertazzoli, R.; Lanza, M. R. V. *Electrocatalysis* **2017**, 8 (3), 189–195.

Chapter 1. Introduction

1.1 Aim of the Thesis

This thesis is concerned with the development, fabrication, characterization and application of multifunctional electrochemical probes on Scanning Electrochemical Probe Microscopy (SEPM) techniques. The fabrication of such probes is challenging and somewhat unconventional, requiring the use and the development of unconventional tools for both fabrication and proper characterization of the fabricated probes. Hence, this thesis encompasses the development of new techniques, tools and instrumentation aimed towards the fabrication and characterization of multifunctional probes, with a special interest in nanometer sized probes. The application of multifunctional probes is beneficial for a broad range of subjects covered by SEPM, justifying the efforts towards reproducible fabrication methods and precise characterization. The developments herein presented includes new tools to facilitate the imaging of multifunctional probes by Scanning Electron Microscopy (SEM) and to enable the imaging by electron Transmission Microscopy (TEM), the development of simple end reliable tools for fast fabrication of multifunctional probes and the application of multifunctional probes for the investigation of complex systems towards the acquisition of topography-free electrochemical information on Scanning Electrochemical Microscopy (SECM) experiments.

Each chapter of this thesis corresponds to a manuscript, together with supporting information, where relevant, from work that was published in peer reviewed journals. Unpublished material is also presented in Chapter 4. Chapter 2 introduces the novel fabrication method developed for custom SEM sample holder that enables high resolution imaging of nanometer sized electrodes and pipettes and even the acquisition

of electron transmission images of nanopipettes. Chapter 3 shows the fabrication and application of a multifunctional, ring-disk, electrochemical probe to investigate complex systems (of biological interest) through the acquisition of topography-free electrochemical information. Chapter 4 regards the development of a new fabrication method for multifunctional electrochemical probes that combines (hybridize) two SEPM techniques and their application to investigate the surface of a substrate with nanometer spatial resolution. Chapter 5 moves to the development of a novel multifunctional electrochemical probe which relies solely on a nanopipette to acquire topographic information and to monitor electrochemical reactions occurring on a substrate.

Although not directly connected with the main subject of this thesis, the development and application of multifunctional electrochemical probes for scanning electrochemical microscopy, appendices 1 and 2, describe the efforts towards development of accessible electrochemical instrumentation, which can have potential application in electrochemistry teaching and in the development of a “low-cost” platform for the design of a research-oriented electrochemistry equipment. Appendix 1 regards to the development of a low-cost, microcontroller based potentiostat capable of performing electrochemical measurements through basic electrochemical techniques, such as cyclic voltammetry. Appendix 2 moves to the development of a scanning electrochemical microscope (SECM) based on the microcontroller potentiostat. This work builds upon the previous findings (described in Appendix 1) and relies on the use of a 3D printer to fabricate a fully functional SECM equipment capable of performing basic space resolved electrochemical measurements using a microelectrode as a probe tip. The findings presented in both Appendix 1 and Appendix 2 are not only important for a fare dissemination and application of electrochemistry, as both are accessible

alternatives, but they also showcase the importance of instrumentation in electrochemical measurements and how the impact of the instrument on the experimental outcome cannot be neglected by users.

As mentioned above, these findings are not (at a first glance) strictly connected to the main subject of this thesis, but the understanding of electrochemical instrumentation and the instrumental impact on the acquired data is a key aspect for good electrochemistry and is in the core of any good electrochemical measurement, hence it cannot be overseen. Also, the impact of accessible instrumentation for teaching on society, which can be translated as accessible education, is undeniable and much needed. Thus, due to the clear importance, the findings of the Author on those subjects were added to this thesis as Appendix 1 and Appendix 2.

1.2 Scanning Electrochemical Probe Microscopy

Scanning Electrochemical Probe Microscopy (SEPM) techniques are powerful tools for investigating electrochemical activity and probing kinetics at the sub-micron level by acquiring space resolved electrochemical information over a wide range of surfaces and interfaces.¹⁻³ Under the umbrella of SEPM are versatile techniques such as Scanning Electrochemical Microscopy (SECM),⁴ Scanning Ion Conductance Microscopy (SICM),⁵ and Scanning Electrochemical Cell Microscopy (SECCM),⁶ which have been used for the investigation of single entities such as single cells and single nanoparticles,⁷⁻¹³ high-resolution topographic mapping,^{14,15} local ion flux, and local conductivity measurements, among others.¹⁶⁻¹⁹ All SEPM techniques record space-resolved electrochemical information (current or potential) through the use of small electrochemical probes that are precisely translated along the investigated surface/interface. When in close proximity to the substrate/interface, the

electrochemical information recorded by those electrochemical probes greatly depends on the substrate/interface characteristics as they, to a certain extent, disturb the electrochemical response of the probes. The nature and extension of this perturbation give information, or at least hints, about the substrate/interface characteristics. The nature of those probes varies with the experimental setup and the SEPM technique being used, but generally their fabrication allows for some of their characteristics, such as the size, to be easily tuned to a certain extent.^{18,20–25} A generic representation of a SEPM setup is presented in Figure 1.1. For most SEPM techniques, with the exception of SECCM, the substrate and electrodes are immersed in a solution bath; this was omitted from the figure to facilitate the visualization of the principal components of the system.

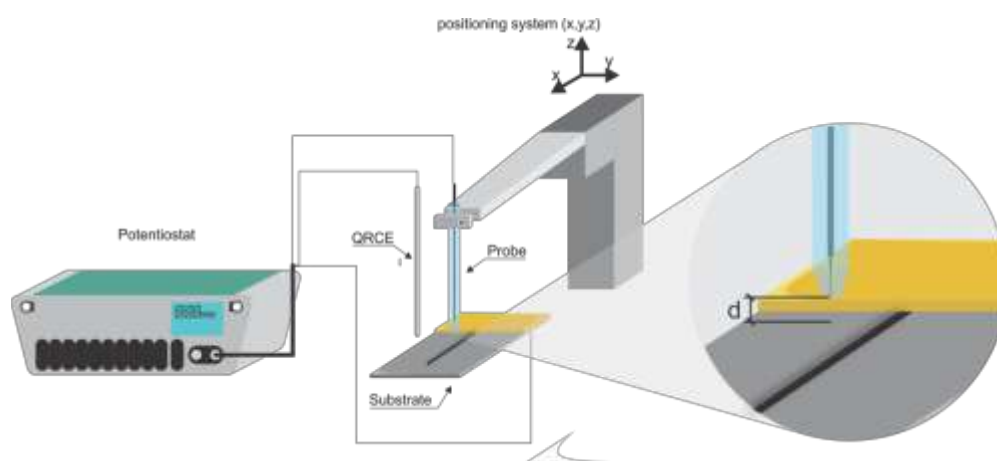


Figure 1.1. Schematic representation of a generic SEPM equipment used to probe substrates (surfaces/interfaces) showing its principal components: Potentiostat, electrochemical probe, investigated substrate and positioning system. QRCE stands for Quasi-Reference Counter Electrode.

The different nature of the electrochemical probes comes from the fact that distinct SEPM techniques acquire electrochemical information (potential or current) in different manners. Hence, they cannot be undistinguishably called electrodes as for some techniques there is no charge transfer or separation occurring at the probe, such as

for pipettes in SICM experiments. Although the probes might differ for each SEPM technique, their fabrication usually rely on similar procedures and are based on similar substrates, quartz crystal and borosilicate glass capillaries, which opens the possibility of fabricating electrochemical probes combining more than one SEPM technique, herein referred as multifunctional electrochemical probes.^{16,21,26}

A key aspect of a multifunctional electrochemical probe is its ability to record more than one electrochemical information at a given time. The nature of those electrochemical information, if current or potential, do not need to be the same, hence a multifunctional electrochemical probe can record both current and potential signals. The advantages of such probes may appear obvious as the ability to record more information from the same experiment drastically increases the density of information recorded, which is always desired as it can, potentially, help one to better elucidate the system being investigated. But one less obvious advantage is that by recording multiple information there is the possibility of surpassing one of the biggest limitations of SEPM in general, the fact the electrochemical information and the topographic information of the substrate/interface are usually entangled in the recorded signal. This entanglement will be better explored and explained in section 1.3, together with the principle of operation of the SEPM techniques used during the development of the work here summarized as a PhD thesis. Nevertheless, it should be clear that, due to the increased density of information recorded, the combination of multiple SEPM techniques through the use of multifunctional probes can further extend the experimental capabilities of these techniques, making them attractive for a broader range of research subjects including energy storage and conversion,^{27,28} nanomaterials characterization,^{11,29} and single cell investigation.^{10,30,31}

1.3 SEPM techniques operation: behind the curtains

1.3.1 SECM

The basic premise behind the operation of any SEPM technique is that the substrate or interface being investigated and their characteristics will interfere, somehow, on the information recorded by the electrochemical probe. The perturbation of the electrochemical response of electrochemical probes in close proximity to a substrate/interface arises, in the simplest case, from the substrate disturbing the mass transport of species (commonly electroactive) towards the electrochemical probe, with the mechanism for such being dependent on the electrochemical information recorded and thus on the SEPM technique being used. When a faradic process (i.e. reduction or oxidation of an electroactive species) is being monitored over a biased electrochemical probe, such as in a SECM experiment, the presence of a substrate in close proximity to the probe (small d in Figure 1.1) will affect the mass transport of the electroactive species towards the electrochemical probe.

The electrochemical probe used in all SECM experiments is usually an electrode, as charge separation (potentiometric mode) or transfer (amperometric mode) will take place on the surface of the probe, no matter if the recorded information is current or potential. One critical aspect of the use of electrodes as probes for SECM is that they have to have small physical dimensions. Electrode construction is normally based on the encapsulation of a metal or conductive material (commonly noble metals), which form the so called electrodic surface, inside an inert insulator.³² The insulator serves two purposes: to delimitate the exposed area of the electrodic surface and to give mechanical stiffness to the electrode. A picture of a 15 μm diameter platinum microelectrode, showing the electrodic surface (platinum disk) and insulating material (quartz) can be seen in Figure 1.2. For experiments carried out with SECM,

electrochemical probes should have small physical dimensions for two reasons, the more obvious one being related to spatial resolution, which will be further explored in section 1.4. The less obvious one is regarded to temporal resolution and based on the fact that the electrochemical information acquired at certain position with the probe needs to be independent of time, *i.e.* current should be recorded at steady-state conditions.

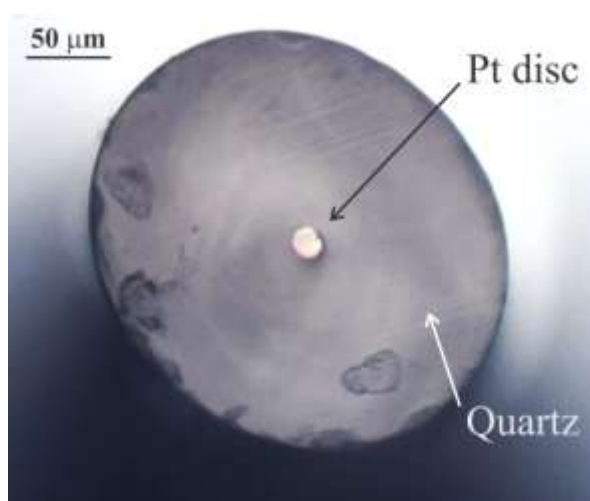


Figure 1.2. Optical microscopy image (top view) of a 15 μm diameter platinum microelectrode encapsulated in a quartz capillary.

Microelectrodes and nanoelectrodes, when properly polarized in a solution containing an electroactive species, show a diffusion limited current that does not change with time. This behavior has been extensively studied in the literature^{33,34} and is due to the high mass-transport rate characteristic of the hemispherical diffusion layer associated with electrodes with dimensions (at least one of them) at the same order of magnitude as the diffusion layer thickness.³⁵ Although this is a time-dependent feature, for most of the applications electrodes with a critical dimension of 10s of micrometers or less will present a steady-state behavior. The current at diffusion limiting conditions for a disk microelectrode embedded into an infinite thick insulator is mathematically described by Equation 1.1.³⁶

$$I_{disk}^{SS} = 4nFDCr \quad (\text{Equation 1.1})$$

Where I_{disk}^{SS} is the diffusion limited current at a disk electrode, F is the Faraday's constant (approx. 96485 Coulombs mol⁻¹), D the diffusion coefficient of the electroactive species, C is the concentration of the electroactive species and r the radius of the disk electrode. Equation 1.1 is commonly used to characterize microelectrodes as, for most applications, the fabrication process of microelectrodes results in the electroactive area being embedded in a thick insulator, which can be considered as "infinite" when compared to the radius of the electroactive disk. This is not true for electrodes that have a thinner insulator layer around the electrodic surface, such as small microelectrodes and nanoelectrodes intended to be used as electrochemical probes for SECM experiments. Such electrodes normally have a small ratio between the radius of the electrode body and the radius of the electroactive disc (Figure 1.3), which is commonly referred to as the radius of glass (RG)³⁷.

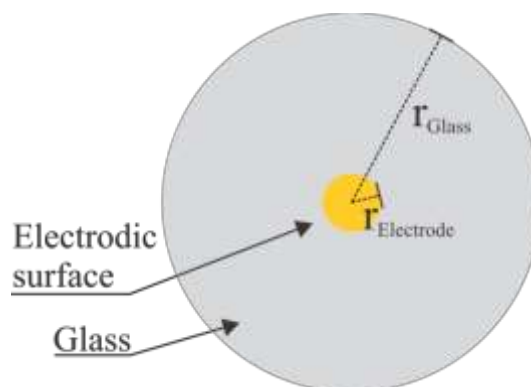


Figure 1.3. Schematic representation of a cross section view of a microelectrode showing the radius of the insulating glass and the radius of the electrodic surface. The ratio of both radii is known as RG.

A more general form of Equation 1.1, valid for electrodes that are not embedded in an "infinite" insulator, is presented in Equation 1.2.

$$I_{disk}^{SS} = XnFDCr \quad (\text{Equation 1.2})$$

The presence of the term “ X ” arises from the need to account for the diffusion of material towards the electrodic surface originated from the solution behind the electrodic surface plane.³⁶ This phenomenon is known as back diffusion and has a significant impact on the mass transport for microelectrodes and nanoelectrodes with small RG. For electrodes with $RG > 10$, the mass transport behavior is similar to that of a disc electrode encapsulated in an infinite insulator plane, thus no back diffusion can occur. In these situations, the term “ X ” is assumed to be 4 and Equation 1.2 becomes Equation 1.1. For $RG < 10$, “ X ” takes different values in order to account for the increase in mass transport rate due to the back diffusion (Figure 1.4) and can be approximated by the analytical expression shown in Equation 1.3.³⁸ As microelectrodes and nanoelectrodes present steady-state diffusion limiting currents and also a small physical dimension, they are the appropriate probes for SECM experiments.

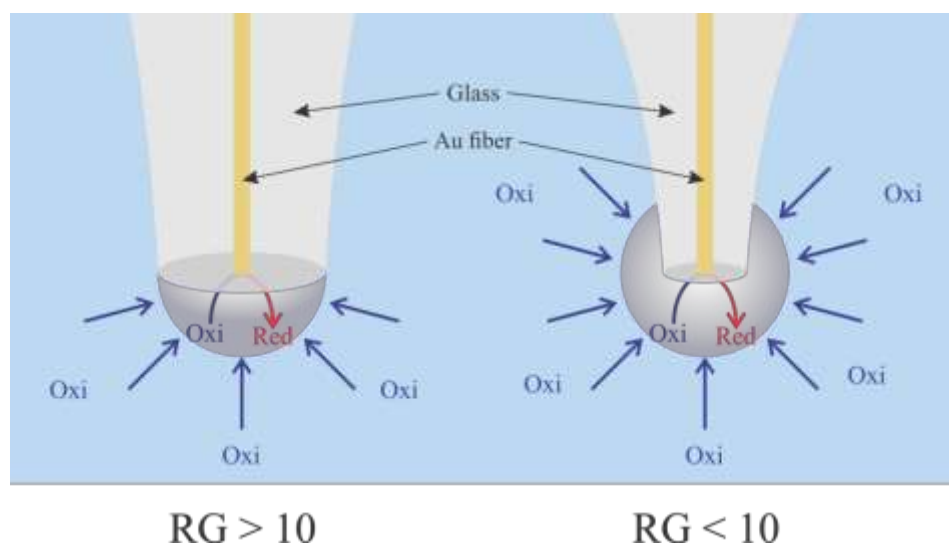


Figure 1.4. Representation of the influence of the electrode RG on the diffusion of species towards the electrodic surface. **(Left)** No back diffusion is observed. **(Right)** Back diffusion is observed.

$$X = 4 + 0.552(RG - 0.6723)^{-0,8686} \quad (\text{Equation 1.3})$$

“**X**” values for a few radii ratios (RG), for common used micro and nanoelectrodes are presented in Table 1.1.

Table 1.1. “X” values for common used electrode RGs.

RG	X
1.5	4.651
3	4.265
5	4.155
10	4.08

By inspecting Table 1.1 and Equation 1.2, it is clearly seen that the impact of the thickness of the glass insulator on the electrode steady-state current should not be neglected when the insulator is very thin. This is important for nanoelectrodes and pipette based electrodes, which can have RG values under 1.5. For such electrodes, the back diffusion effect will increase the steady-state current by more than 10%, in comparison to the value predicted by Equation 1.1.

The presence of a substrate within the diffusion region of a properly biased microelectrode, immersed in a solution bath, will affect the transport of electroactive material towards the electrodic surface. This phenomenon is known as *feedback* and it is used in SECM experiments to investigate substrates and interfaces.³⁹ The presence of a substrate will hinder the diffusion of material towards to and from the electrodic surface, effectively blocking the arrival of material from bulk solution and confining the electro-generated products of the electrodic reaction. The impact of this blocking/confinement on the current recorded over an electrode will depend on the nature of the substrate and two limiting conditions should be considered; *i*) The electron

transfer rate for the species being generated at the microelectrode is zero at the substrate (i.e., the substrate is an “insulator”, $k_s \rightarrow 0$). *ii*) The substrate has an infinitely large electron transfer rate for the species being generated at the microelectrode (i.e., the substrate is a “conductor”, $k_s \rightarrow \infty$). k_s is the rate constant at the substrate for the electron-transfer (ET) reaction of the species generated at the tip.⁴⁰ The two limiting situations, and their effect on the current recorded over the microelectrode, are illustrated in Figure 1.5.

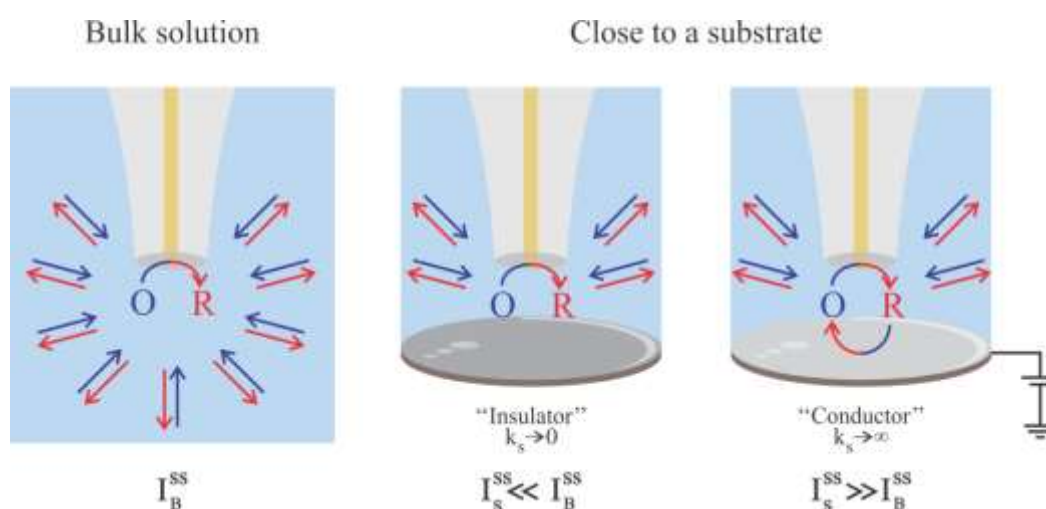


Figure 1.5. Representation of a biased microelectrode in a solution bath at bulk solution and in close proximity to a substrate.

In the first limiting situation ($k_s \rightarrow 0$), the hindering of material diffusion to the electrode acts towards limiting the rate, and thus the amount of material arriving at the electrodic surface. Hence, the recorded current should be lower when compared with the current recorded at bulk solution, $I_S^{SS} \ll I_B^{SS}$, where the subscript indexes S and B denote “at the substrate” and “at bulk solution”, respectively. Even though there is a confinement of the electrogenerated species (R on the example of Figure 1.5), as the substrate is an “insulator” (i.e. $k_s \rightarrow 0$) they have no influence on the recorded current at the tip. This phenomenon is known as *hindered diffusion* or *negative feedback*. It is important to note that despite the decrease in the *apparent* mass transport rate of the

microelectrode, a diffusion limited current will still be observed. For the second limiting situation, the same effect of the hindered diffusion takes place, but now the influence of the confinement should be taken into account as the substrate is a “conductor” (i.e. $k_s \rightarrow \infty$) and the electrogenerated species R can undergo an ET reaction at the substrate, being converted back to O. The O species being generated on the substrate can now undergo an ET reaction at the microelectrode. This feedback cycle will effectively increase the amount of material (O in the example presented in Figure 1.5) arriving at the microelectrode and the recorded current should be higher when compared with the current recorded at bulk solution (i.e. $I_S^{SS} \gg I_B^{SS}$). This phenomenon is known as *positive feedback*. The positive feedback is only observed when the species being monitored at the microelectrode can undergo a reversible ET reaction at the substrate.

Although we have only explored in the examples above the feedback phenomena with the electrode in very close proximity to a substrate, it is easy to understand that this is not a discreet phenomenon and has a continuous dependence with the microelectrode/substrate separation with the effects on the recorded current (both for positive and negative feedback) increasing with a decrease in the separation. The electrode is then sensitive not only to the nature of the substrate (if conductive or insulator), but is also sensitive to the microelectrode/substrate separation and hence, to substrate topography. It should be noted that the sensitivity to the substrate nature is also not discreet and the situations presented are the limiting conditions, i.e, substrates that present a rate constant (k_s) between 0 and infinite will also affect the current recorded by the microelectrode. Thus, when a biased microelectrode is continuously approached from bulk solution towards a substrate while the current is recorded, such value should increase (if the substrate is conductive) or decrease (if the substrate is an insulator) as the microelectrode/substrate separation decreases. Such experiment is

known as an approach curve and is used for both establishing the microelectrode/substrate separation and to investigate the substrate properties. In an approach curve experiment, the polarized microelectrode is brought from bulk solution towards the substrate at a constant speed (ranging from a few nm s^{-1} to a few $\mu\text{m s}^{-1}$) while current is recorded. A set of normalized approach curves towards substrates having different electron-transfer rate constants, simulated using the analytical approximation proposed by Lefrou *et al.*⁴¹, can be seen in Figure 1.6.

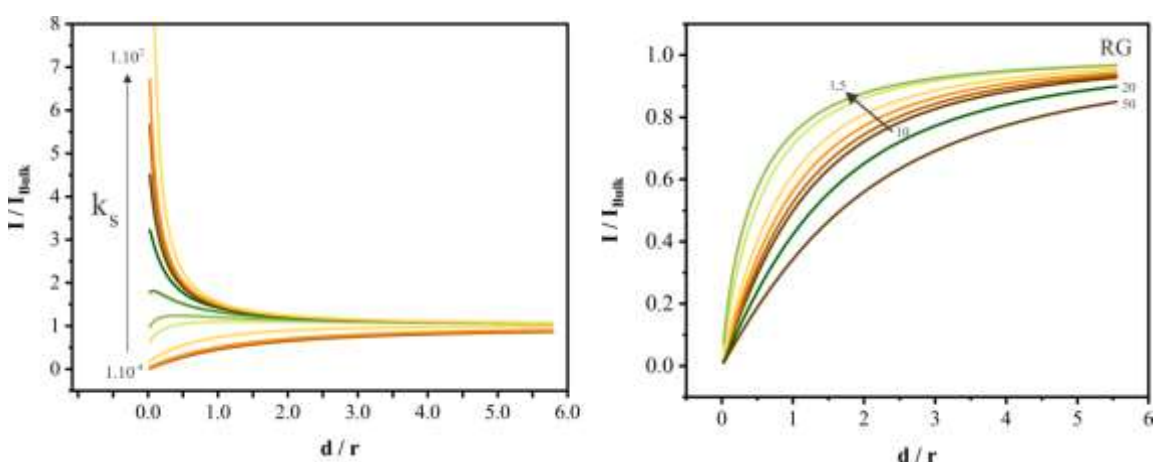


Figure 1.6. (Left) Simulated data for approach curves of a properly biased microelectrode towards substrates with different electron-transfer rate constants. Constant values ranging from 10^{-4} to 10^2 cm s^{-1} , $RG = 10$. (Right) Simulated data for approach curves towards an “insulator” substrate with microelectrodes of different RG values ranging from 50 to 1.5. I_{Bulk} is the current recorded at the electrode at bulk solution (without interference of the substrate). d is the microelectrode/substrate distance and r the electrode radius.

The approach curves shown in Figure 1.6 are normalized by dividing the recorded current at the electrode (I) by the recorded current at bulk solution (I_{Bulk}) and by dividing the microelectrode/substrate separation (d) by the electrode radius (r). Hence, values are independent of electrode radius and electroactive species concentration. It is easy to note that the influence of the substrate on the recorded current is accentuated with a decrease in microelectrode/substrate separation for both

positive and negative feedback phenomena. The influence of the substrate electron-transfer rate constant (towards the ET reaction of the products generated at the microelectrode) is also clear on the left graph and the limiting situation ($k_s \rightarrow 0$ and $k_s \rightarrow \infty$)⁴⁰ can be understood as both the upper and lower approach curves. The curves between those are for a wide range of rate constant values and demonstrate that not only the microelectrode is sensitive to its separation from the substrate, but also the current response, while approaching, gives information regarding the substrate nature. It is important to note that both information are included (together) in the single set of data acquired in an approach curve experiment, and hence they cannot be completely untangled. Without the aid of other techniques, it is impossible to assign the approach curve profile to either just the nature or topography of the substrate. The influence of the microelectrode RG on the recorded current (Figure 1.6, right graph) is due to the increase of the physical dimensions of the electrode body (with an increasing in RG), which favors the blockade/confinement of species and leads to the microelectrode being able to sense the substrate from further distances. Although a microelectrode with a large RG can sense the substrate from a large microelectrode/substrate separation, the approach curve is much more gradual (less steep) and the current change for a given microelectrode displacement is much smaller when compared to the same displacement for a microelectrode with a smaller RG, which have a much steeper approach curve. Another disadvantage of microelectrodes with a large RG value is the impossibility of approaching them very close to the substrate, as the electrodic plane will never be perfectly parallel to the substrate plane, even if absolute care is taken to align the electrode perpendicular to the substrate plane. As a result, the microelectrode will always approach towards the substrate in a slight angle and the microelectrode body (insulator sheet around the electrodic surface) will contact the substrate first, limiting

the minimal working distance (i.e. the minimal microelectrode/substrate separation) during a SECM experiment (Figure 1.7). The simulated data presented in Figure 1.6 does not account for this angle and hence all curves go towards a d / r value of zero, meaning that the electrodic face contacted the substrate.

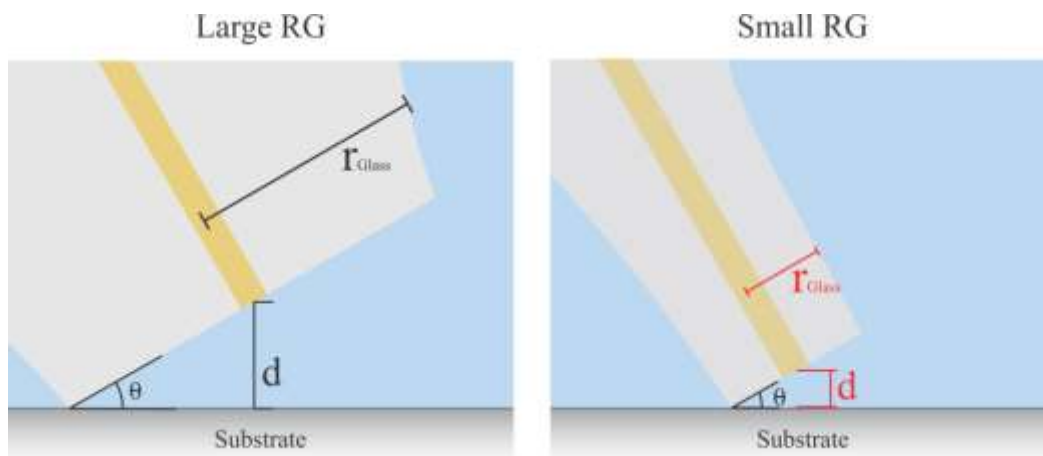


Figure 1.7. Impact of microelectrode RG on the minimal working distance for a microelectrode approaching towards the substrate at a slight angle θ (exaggerated).

Despite powerful, the feedback mode accounts for only one of the modes of operation of SECM.^{39,40,42,43} The variety of techniques and operation modes available grants SECM the status of a flexible and powerful tool capable of investigating a variety of substrates. One powerful SECM mode of operation is the Generation/Collection mode (G/C). Under SECM G/C mode there is a whole “family” of modes and techniques such as Substrate Generation/Tip Collection (SG/TC) and Tip Generation/Substrate Collection (TG/SC). For these techniques, as any other technique derived from the G/C modes, the recorded electrochemical information not only is affected by the interference of the substrate over the mass transport towards the electrochemical probe, but is also dependent on the collection efficiency of the system as the information is originated from the charge transfer reaction of an electrochemical species that is being generated, *in loco*, by either the probe or the substrate (Figure 1.8).

The effect of the substrate on the collection efficiency of the system is particularly useful for probing active sites (for a given reaction) over a substrate.^{44,45} Although other modes of operation for SECM exist, they are all based on either the feedback or G/C modes.

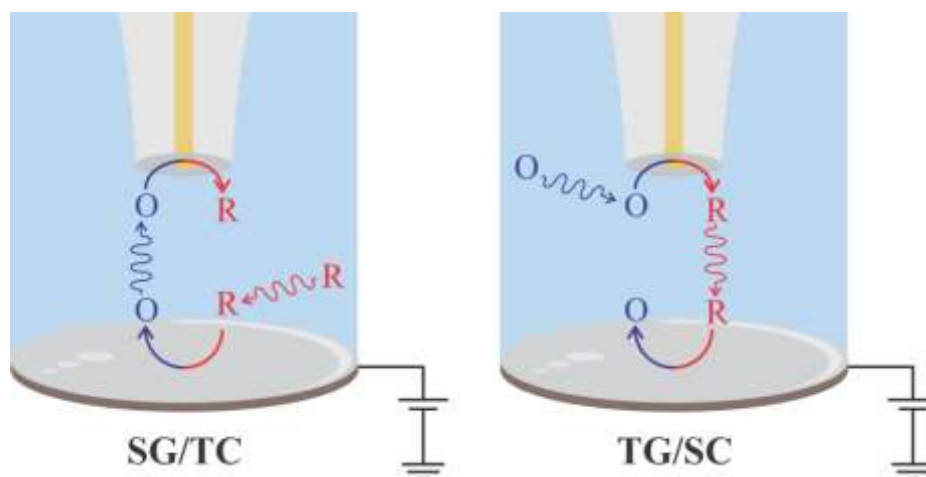


Figure 1.8. Schematic representation of (Left) Substrate Generation/Tip Collection and (Right) Tip Generation/Substrate Collection SECM S/G modes.

1.3.2 SICM

The Scanning Ion Conductance Microscopy (SICM) is a SEPM technique based on the monitoring of a current resulting from the passage of ions through a small opening at an electrochemical probe. The influence of a substrate over the mass transport at the electrochemical probe is highly dependent on the substrate/probe separation and hence, very sensitive to substrate topography. Accordingly, SICM has been widely explored for investigating and imaging (topography) sensible and fragile substrates such as single cells and biological tissues.^{46–48} SICM electrochemical probes are usually fabricated from quartz capillaries, which are pulled to a very sharp taper forming a micro or nanopipette (pipette opening radius in the micro or nanometer range, respectively). This fabrication procedure is easy and simple and allows the tailoring of the pipette opening radius from 100s of micrometers to 10s of nanometers. Although both SECM and SICM experimental setups are similar (instrumentation wise), the

techniques differ on the nature of the electrochemical information acquired during the experiments. In a SICM experiment, no charge transfer reaction takes place at the surface of the electrochemical probe and, for most situations, charge separation does not affect the probe response. The electrochemical response, for the simplest case, is due to the flow of ions between a QRCE immersed in an electrolyte solution bath and one inside the electrolyte filled pipette when a difference of potential is applied between those two QRCEs. The small pipette opening acts as a resistor and limits the ions flow, thus limiting the recorded current (Figure 1.9). Such current is constant and dependent on the pipette radius and geometry, solution conductivity and the potential difference applied between the two QRCEs, when the pipette is held at bulk solution, away from a substrate.

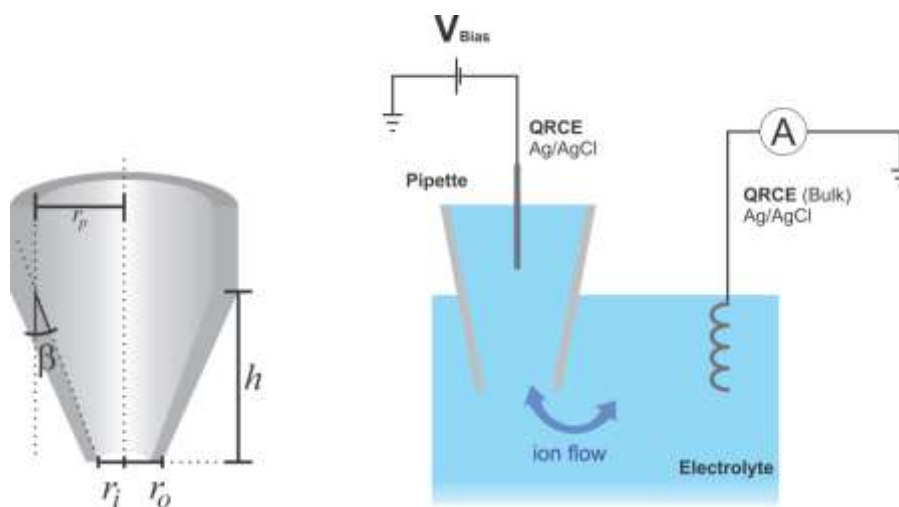


Figure 1.9. Representation of a pipette (sliced along its main axis) and typical SICM setup showing important pipette geometry parameters such as the opening radius (r_i), outer tip radius (r_o), tip base radius (r_p), pipette inner semi cone angle (β), and taper length (h).

The small opening at the pipette tip acts as a resistor by restricting the ion flow between the two QRCEs. The resistance of the opening can be estimated by Equation 1.4:

$$R_p = \frac{1}{K \pi r_i \tan\beta} + \frac{1}{4 K r_i} \quad (\text{Equation 1.4})$$

Where R_p is the resistance to ionic flow across the pipette opening, K is the electrolyte solution conductivity, r_i is the pipette opening radius and β is the inner semi cone angle (Figure 1.9). At adequate electrolyte concentration, where no current rectification is observed,^{49,50} *i.e.* the charge separation effect at the pipette opening walls does not impact the recorded current, the pipette opening behaves like an ideal resistor and the current, due to the ionic flow, at a pipette in bulk solution of an electrolyte bath can be estimated by Equation 1.5.

$$i_p = V_{bias} / \left(\frac{1}{K \pi r_i \tan\beta} + \frac{1}{4 K r_i} \right) \quad (\text{Equation 1.5})$$

Where i_p is the current due to the ionic flow through the pipette opening and V_{bias} is the potential applied between the two QRCEs.

Equation 1.5 is only valid for pipettes at bulk solution as it does not account for the separation between the pipette opening and the substrate. Similar to SECM, the presence of a substrate in close proximity to the pipette will affect the mass transport towards the pipette opening, affecting the recorded current. Not only the pipette opening resists to ion flow, but the solution resistance also accounts for resisting the current flow. When the pipette is at bulk solution, the solution resistance (R_s) is much smaller than the pipette opening resistance (R_p) and the current is limited by the latest (Figure 1.10, left). When the pipette approaches the substrate, the solution becomes confined between the substrate and the pipette, hence the apparent solution resistance increases until a point in which it becomes larger than the pipette opening resistance. This effect takes place when the thickness of the solution layer confined between the pipette and the substrate is approximately the same as the pipette opening diameter. At this point,

the ionic flow is not limited by the pipette opening, but by the resistance of the solution layer between the pipette and the substrate, which increases with a decrease in the pipette/substrate separation (Figure 1.10, right). Hence, the pipette is able to sense the substrate and substrate topography as the current only depends on the pipette/substrate separation.

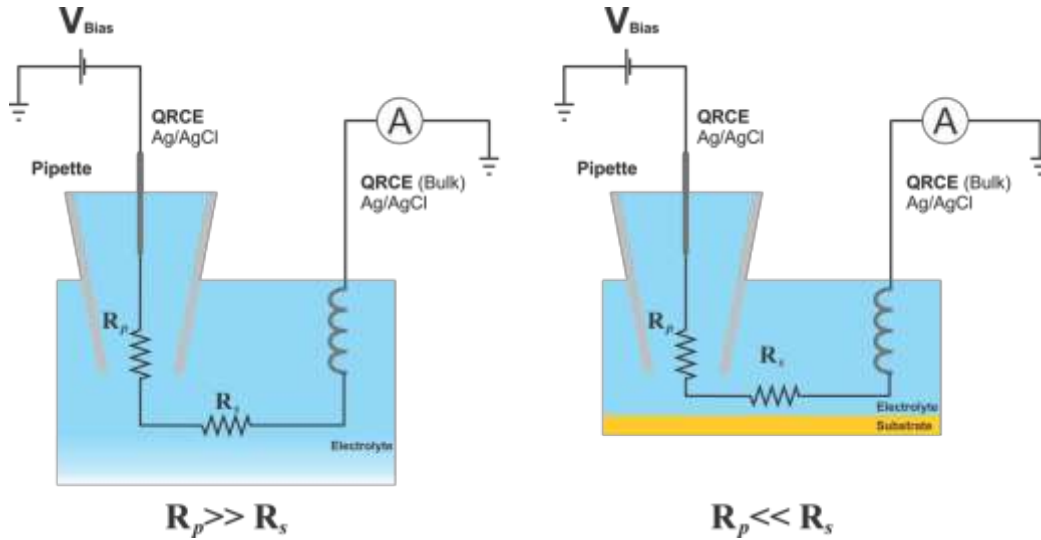


Figure 1.10. Representation of the equivalent circuit for the current flow through a pipette (**left**) at a bulk solution and (**right**) close to a substrate.

The ionic current dependence on the pipette/substrate separation is similar to the one observed in a SECM experiment with hindered diffusion (negative feedback), as the phenomena influencing the recorded current is the same, the blockage of material transport towards (or through) the electrode. This ionic current/separation dependence can be mathematically described, in terms of the pipette geometry (Figure 1.9), according to Equation 1.6.⁵¹

$$i = i_{max} \left(1 + \frac{3/2 \ln\left(\frac{r_o}{r_i}\right) r_p r_i}{d h} \right)^{-1} \quad (\text{Equation 1.6})$$

Where i is the recorded ionic current, i_{max} is the ionic current when the pipette is at bulk solution, r_o is the outer tip radius, r_i the pipette opening radius, r_p the tip base

radius, d the pipette/substrate separation and h the pipette taper length. The ionic current recorded at bulk solution (i_{max}) is given by Equation 1.5.

Unlike in SECM, the nature of the substrate (usually) does not interfere in the recorded current and the hindered ion migration is the only effect that influences the recorded current. Thus, the profile of an approach curve for an SICM experiment will be independent of the substrate characteristics and a decrease in current with a decrease in pipette/substrate separation will always be observed. As the separation influence on the recorded current is due to a blockage in material arriving towards the pipette, it is easy to imagine that the approach curve profile will be somehow affected by the pipette RG, which is defined as the ratio between the tip outer radius (r_o) and the pipette opening radius (r_i). Using simple trigonometry relations, Equation 1.6 can be rewritten as Equation 1.7, which expresses the normalized ionic current ($i_{norm} = i/i_{max}$), as a function of the normalized pipette/substrate distance ($L=d/r_i$).

$$\frac{i}{i_{max}} = \left(1 + \frac{3}{2} \ln(RG) \tan\beta L^{-1}\right)^{-1} \quad (\text{Equation 1.7})$$

Where $i_{norm} = i/i_{max}$, $L=d/r_i$, $RG= r_o /r_i$ and β is the inner semi cone angle.

A set of normalized SICM approach curves, calculated using Equation 1.7, for different pipette RG values and different pipette inner semi-cone angles, can be seen in Figure 1.11.

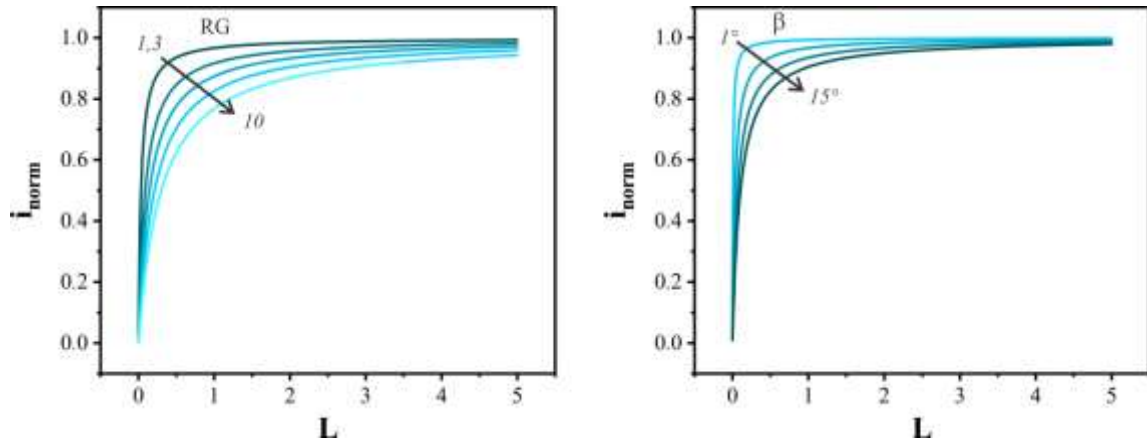


Figure 1.11. Simulated SICM normalized approach curves for (**Left**) different pipette RG values (1.3,2,3,5 and 10) and (**Right**) different pipette inner semi-cone angles, β ($1^\circ, 5^\circ, 10$ and 15°). L is the normalized pipette/substrate distance (d/r_i) and i_{norm} is the normalized ionic current (i/i_{max}).

Although it is true that the RG value impacts the approach curve, as seen in Figure 1.11, pipettes usually have very small RG, close to the unit value (Figure 1.12), which is intrinsic from its fabrication procedure. The inner semi-cone angle (β) is also an important parameter, with a huge impact on the ionic current response of a pipette. Both of those parameters are not easy to be accessed, especially for nanometer sized pipettes, and usually require the use of electron transmission imaging techniques.

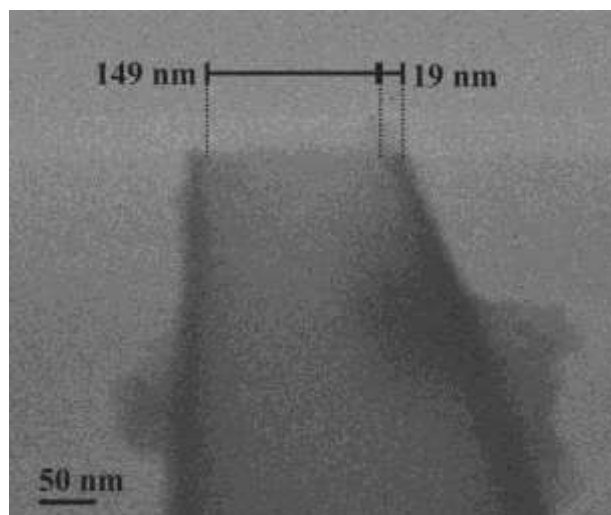


Figure 1.12. Electron transmission images of the side of a nanopipette showing the opening diameter and the wall thickness. $RG = 1.3$. Accelerating Voltage = 12 kV.

Although, according to Equation 1.5, the current monitored with a pipette at bulk solution should be unchanged as a function of time, this does not hold to be true in an actual experiment as the response of both employed QRCEs is not completely stable. This change in the monitored current (due to the change in potential), while an experiment is performed, could be naively assigned to a change in pipette/substrate separation and hence, a change in substrate topography. To overcome this potential (and current) drift, a periodic perturbation is usually added to the recorded current, inducing an alternated component (AC) to the ionic current. The amplitude of the AC component, as it is a relative measurement, is not influenced by current and potential drifts and can be used as a stable signal to access pipette/substrate separation. The perturbation is usually performed by oscillating the pipette in the z axis (perpendicular to the substrate plane) with small amplitude, typically 1/10 of the pipette opening. This small oscillation is not enough to impact the mass transport across the pipette opening when the pipette is far from the substrate, where the resistance limiting the ionic current is the pipette opening resistance. When the pipette is in close proximity to a substrate, and the resistance of the solution layer between the pipette and the substrate is limiting the ionic

current, the small oscillation in the z axis will periodically change the thickness of this solution layer thus periodically changing the resistance and inducing an AC component to the recorded current. As such, the amplitude of the AC component is close to zero when the electrode is far from the substrate and will increase with a decrease in the pipette/substrate separation. This type of AC modulation is known as amplitude modulation and a schematic representation of the pipette oscillation and the resulting approach curves for the recorded ionic current (i_{DC}) and the AC induced component (i_{AC}) can be seen in Figure 13.

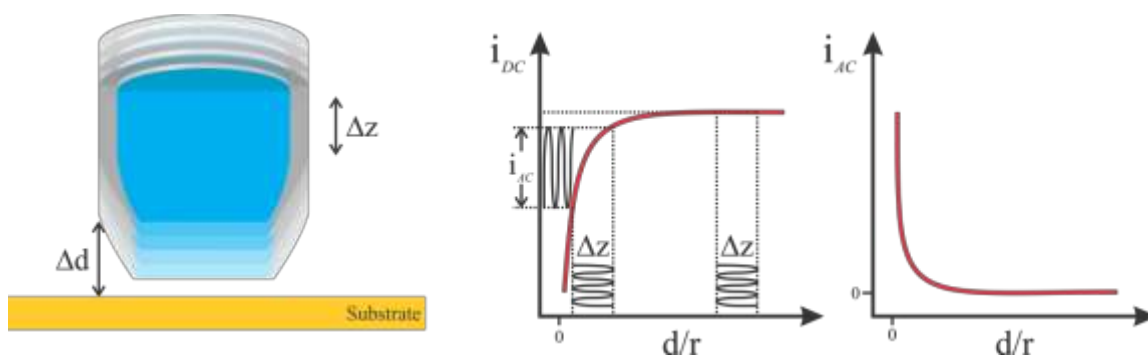


Figure 1.13. Schematic representation of an amplitude modulated SICM experiment showing the pipette vertical oscillation (z axis) and the corresponding approach curves for the direct (i_{DC}) and alternated (i_{AC}) components of the recorded current. d is the pipette/substrate separation and r the pipette radius.

This ability to approach a pipette to close proximity to a substrate/interface (approx. the pipette opening diameter) and hold at the same separation independent of perturbation in the system (QRCE potential drift, changes in conductivity due to thermal fluctuation and etc.)⁵¹ makes SICM an extreme capable technique to image topography, especially on soft and fragile samples, which justify the increased attention given to this technique for imaging single cells and biological tissues. Although somewhat limited when compared to SECM, SICM can also be used to investigate the nature and monitor reactions which are occurring over a substrate.^{12,19,49} Even though, SICM is still the best

technique for investigating topography of a substrate/interface in a solution bath and, when a positional feedback system is added to the instrumentation, the value of the i_{AC} amplitude can be used as the set-point of a loop control system for the z axis, enabling the pipette to be scanned over a rough substrate at a constant pipette/substrate separation.

1.3.3 Multifunctional electrochemical probes and Hybrid techniques

Despite being a versatile SEPM technique capable of investigating a variety of substrates/interfaces, SECM struggles with the entanglement of topography and substrate characteristics in the recorded electrochemical information (as explored in Section 1.2). This is the biggest limitation of SECM and reduces its application to substrates with little topographic features (with low aspect ratio) and increases the minimal working distance, affecting the spatial resolution and acquired information density (see Section 1.4 below). In contrast, SICM is a powerful technique when it comes to tracking rough topographies with high aspect ratio, its working distance is set by the pipette opening diameter (which can be easily tailored to 10s of nanometers), but struggles in investigating substrate/interfaces properties as it is somewhat unselective. As one technique complements the shortcomings of the other, it is easy to see how hybridizing them would be beneficial, generating an SEPM technique that excels in both tracking topography and investigating substrate/interfaces properties.

This is only possible using an electrochemical probe that is capable of recording currents due to ion migration and faradaic currents due to ET reactions, *i.e.* a multifunctional electrochemical probe is required. Multifunctional electrochemical probes can be defined as probes used in SEPM techniques that, differently from

conventional electrochemical probes, *are capable of acquiring multiple space resolved electrochemical information through one or more electrodic surfaces*. This general definition reflects the general nature of multifunctional electrochemical probes which the type, shape, size and form depends on the information being acquired simultaneously. Hence, multifunctional probes can be a single electrode,⁵² a single pipette,¹⁹ a double or quad barrel pipette,^{53–55} two or more electrodes in a side-by-side⁴⁴ or ring-disc^{22,45,56} configuration or any combination of the those (Figure 1.14).^{16,57}

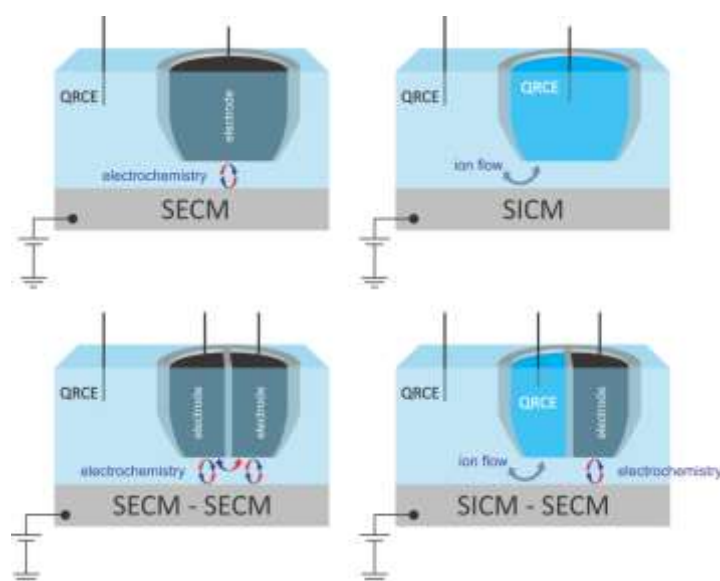


Figure 1.14. Representation of (Top) electrochemical probes for SECM and SICM and (Bottom) multifunctional electrochemical probes highlighting the nature of the electrochemical information recorded.

As SICM and SECM depend on electrochemical probes that are intrinsically different in nature (pipette and electrode), the coupling of those two techniques requires a multifunctional probe that has an electrolyte filed compartment with a small opening (pipette) and also a solid electrodic surface (electrode). One way to make such probes is by using double-barrel micro and nanopipettes and selectively fill one of the barrels with a conductive material (usually pyrolytic carbon) to form the solid electrodic surface, while the unfilled barrel can be used as a SICM pipette. The fabrication of

those probes starts with double barrel quartz capillaries (also known as theta-capillaries), which are pulled to a sharp taper forming a micro or nanopipette. The selective deposition of pyrolytic carbon can be accomplished by filling one of the barrels with a fluid carbon source fuel (usually butane) and heating the pipette under a low oxygen atmosphere to favor pyrolysis over combustion. The carbon deposited on the pipette walls, under the appropriate circumstances, completely fills one of the barrels while keeping the other one unfilled and unblocked. A representation of the fabrication method, proposed by Takahashi *et al.*,¹⁶ is presented in Figure 1.15.

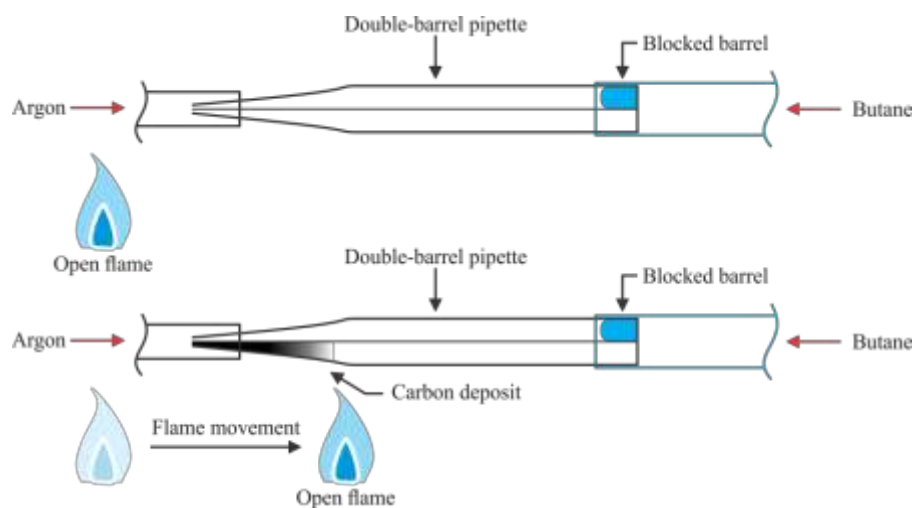


Figure 1.15. Fabrication procedure for double-barrel carbon SECM-SICM multifunctional electrochemical probes.

By using the SICM signal as a positional (z axis) feedback, electrochemical information can be collected over the SECM electrode at a constant electrode/substrate separation allowing pure electrochemical information, free from topography influences, to be acquired. This permits the direct interpretation of the electrochemical information obtained along a substrate as the multifunctional probe, through the SICM positional feedback, can track the substrate topography while scanning it. Also, by having a strong positioning feedback system, the electrode can be approached toward sensible and soft substrates without the risk of crashing the tip, thus damaging the substrate. Although

SICM excels in topography tracking (some times more so than Atomic Force Microscopy (AFM)),⁴⁷ substrate/interface information can also be acquired by the SICM probe,¹⁹ as it can also specific delivery materials and modify the surface/interface.^{10,54}

Even though the hybridization of different SEPM techniques is an obvious application for multifunctional electrochemical probes, different modes of operation for the same SEPM technique, or even the same mode of operation but with different setups, can be implemented through the use of multifunctional probes without violating its definition which is to be *capable of acquiring multiple space resolved electrochemical information*. And, despite being hugely desirable, not all multifunctional probes are capable of acquiring electrochemical information free from substrate topography influences, at least not in a quantitative manner as it will be explored in chapter 3 (Ring-disc). Hence, an electrode capable of sensing two different species (acquiring two different electrochemical information) can, and should be, considered a multifunctional electrochemical probe. In the simplest scenario, a multifunctional electrochemical probe can consist of a single electrode (one electrodic surface) that can acquire different electrochemical information, usually regarding different substrate/interface characteristics, which can be simply achieved by polarizing the electrode at distinct potentials in order to selectively (or not⁵⁸) detect different electroactive species. A more elegant way to record multiple electrochemical information on the same electrodic surface is to partially modify the electrode with a material that enables (or increases) the electrode response (current or potential) towards a specific chemical species. The partially modification results in electrodic surface areas that are unmodified, effectively transforming one electrodic surface in two. Santos *et al.* demonstrated the viability of such approach to fabricate a amperometric/potentiometric

multifunctional electrochemical probe to investigate pH changes at the vicinity of a copper substrate during the cathodic reduction of nitrate.⁵² One intrinsic disadvantage of using only one electrodic surface is the loss of temporal resolution as the different electrochemical information cannot be accessed simultaneously.

The use of multiple electrodic surfaces enables the acquisition of multiple electrochemical information simultaneously, increasing the temporal resolution and the information density. On its simplest configuration, a side by side electrode configuration (Figure 1.14) can be used where each of the electrodic surfaces is responsible for acquiring a distinct electrochemical signal. In such configuration, the substrate topography/properties entanglement can be partially solved by either monitoring (in one of the electrodes) an electroactive species that is insensitive to substrate properties (a species that undergoes an irreversible ET reaction at the substrate, for positive feedback related measurements) or, if the species being monitored is sensitive to substrate properties, monitoring the collection efficiency of a G/C system between the different electrodic surfaces on the multifunctional probe, as it will be explored in Chapter 3.^{22,26} Those are only a few examples of multifunctional electrochemical probes that are not aimed at hybridizing SEPM techniques, but rather in increasing the density of acquired information or mitigating the influence of substrate topography on the electrochemical response of the probe. It is important to note that other multifunctional probes can be used to achieve similar goals by hybridizing other, non-electrochemical, techniques with SEPM, such as shear-force and AFM based SEPM probes.⁵⁹⁻⁶³ As those probes rely on the acquisition of a secondary non-electrochemical information, they cannot be considered multifunctional electrochemical probes and hence, are not within the scope of this thesis.

One aspect common to all multifunctional probes for SEPM experiment is the requirement of a multi-step and, normally, time demanding, intricate fabrication procedure, which greatly differs from the fabrication of regular SEPM probes. As the nature of the multifunctional probe depends on the information being acquired, different specific fabrication procedures need to be developed/applied to each different probe. Thus, the fabrication of multifunctional probes is more an “art form” than a technique and requires from the person fabricating the probes ingenuity to develop innovative fabrication techniques and experimental procedures to produce and apply them. As the multifunctional probes are usually unconventional and need to have very specific features incorporated (different electrodic surfaces, small openings, among others), not only their fabrication processes pose a challenge but also the precise characterization is complicated and usually requires the use of specific tools and techniques. This is even more critical when the size of the probes is significantly decreased, requiring the use of custom tools for a proper probe characterization.

1.4 SEPM spatial resolution: A tale of probe sizes

In any SEPM experiment the electrochemical information is acquired through the electrochemical probe used, disregarding its nature; if an electrode or a pipette. As such, it is easy to understand that the spatial resolution of any SEPM technique strongly depends on the probe size with an increase in resolution with a decrease in probe size. This is straightforward to understand as the electrochemical information being collected by a probe is sampled from the whole (electrodic) surface and hence it is an average of every single electrochemical process happening along the electrodic surface extension, thus, the electrodic surface can be seen as the smallest spatial unit where electrochemical information can be resolved *i.e.* the smallest pixel size on an electrochemical image. Decreasing probe size will not only increase the spatial

resolution, but will also increase the density of information acquired. One easy analogy would be to compare the pixels in an electrochemical imaging experiment with the pixels in a photo and the electrochemical information acquired (current or potential) with the chromaticity values in the photo pixels. Figure 1.16 illustrates this analogy by showing a photo of the same object (a rose), with the same dimensions, but varying the pixel density (*i.e.* pixel size).

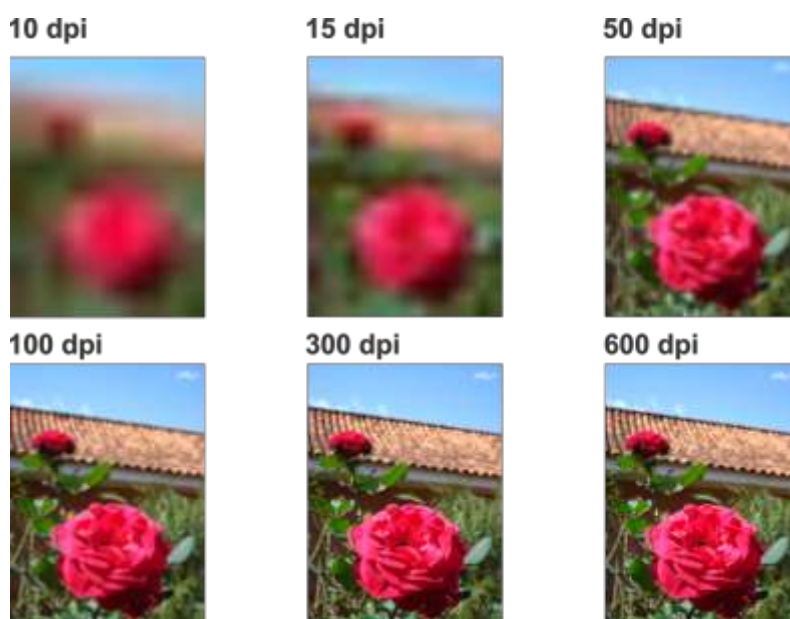


Figure 1.16. Photos of the same object and with same dimension for different pixel densities (pixel size) expressed in dots per inch (**dpi**).

Decreasing the pixel size (increasing pixel density) greatly improves the resolving power of the photo which is much sharper and the object is much better defined (less blurry) at a small pixel size (600 dpi). A decrease in pixel size not only helps to define the object being portrayed, but also increases the density of information (in the red chromaticity channel of this example) with areas that seemed homogeneous on a low-density image (10 dpi) showing a big heterogeneity on higher pixel density images (100 dpi), as demonstrated in Figure 1.17.

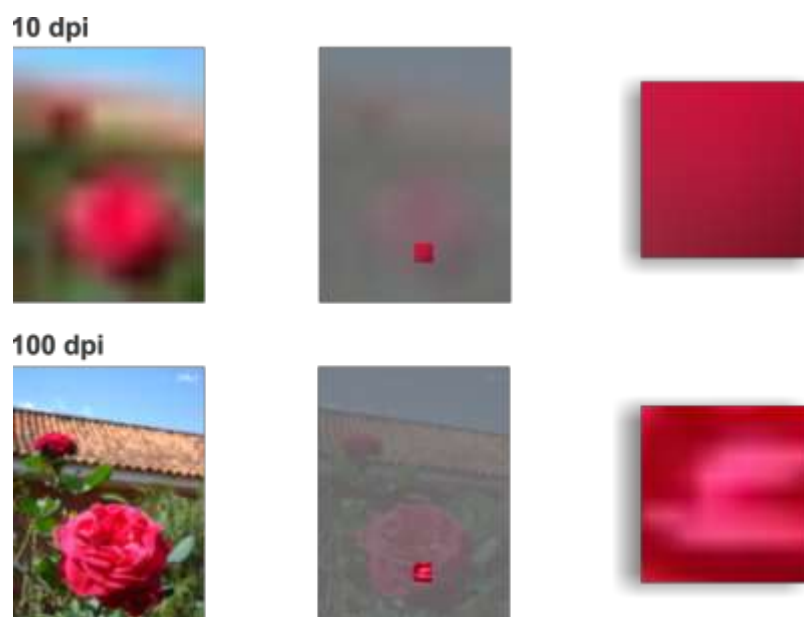


Figure 1.17. On the left, photographs of the same object reproduced at two different pixel densities 10 dpi (top) and 100 dpi (Bottom). On the right, expanded fragment (with the same area) of both photos illustrating the difference in density of information (in this case in the red chromaticity channel).

This is no different for electrochemical imaging, where the pixel size is limited by the probe size and the pixel information is an electrochemical quantity, such as current or potential. When working with large probes (*i.e.* large pixel sizes, lower densities) the pixel value is an average of the electrochemical quantities among that pixel area, hence variations of those quantities within that area are not recorded and are averaged out to the same value. This is a disadvantage in using lower density imaging techniques, as key information can be lost, much like when using bulk electrochemical methods.

Despite being the biggest limiting factor in SEPM spatial resolution, the probe size is not the only factor, as the resolution is also affected by the probe/substrate separation (working distance). The substrate effect over the recorded current is originated from mass transport perturbations and, ultimately, the SEPM tip is probing the substrate diffusion field hence, a large working distance will decrease the spatial

resolution by introducing blurriness in the image due to the small concentration gradient at the edges of the diffusion region. This effect is known as diffusion blur.⁶⁴ By reducing the working distance, i.e., effectively placing the probe further inside the substrate diffusion zone, the blur can be reduced due to the greater concentration gradient present inside the diffusion region, thus increasing the current contrast. An analogy that might be useful to understand this process is to imagine that the electrode is a flashlight and the spot of light it projects over the substrate is the image pixel size (Figure 1.18). When the flashlight is far from the substrate (large work distance) the light spot is large and dim, representing a large pixel size and a lower current contrast. When the flashlight is brought closer to the substrate (small working distance), the light spot is smaller and brighter, representing a smaller pixel size and higher current contrast. As the probe size also contributes to the minimal working distance (see Section 1.2, Figure 1.7), the diffusion blur can also be mitigated by the use of smaller probes.

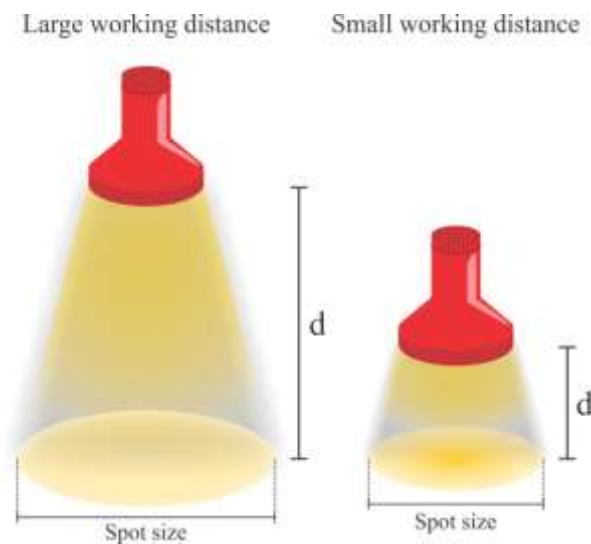


Figure 1.18. Light spot size and brightness dependence on the separation between the flashlight and a substrate (d), which is analogous to the spot size and current contrast dependence on the working distance in SEPM.

As spatial resolution limitations in most SEPM techniques are related (directly or not) to probe size, most efforts to increase spatial resolution have been employed on decreasing probe size. Although this may sound as a straightforward, simple and obvious strategy, a series of implications and complications arise when decreasing probe size to 10s of nanometers. The fabrication becomes more challenging and less reproducible, and traditional fabrication procedures are, mostly, not suitable. Hence, there is the need for developing new and innovative fabrication strategies and procedures, as well as optimize old methods. The proper characterization of probes of nanometer size is also challenging, requiring the use of techniques developed to other purposes, such as those used to characterize nanomaterials. Implementing those techniques for physically bulky samples, as micro and nanoelectrodes, requires the use of specially developed tools and procedures. All those limitations become even more critical when working with multifunctional nanometer sized electrochemical probes. Nevertheless, the benefits, in terms of spatial resolution and information density, of using nanometer sized SEPM probes far outweighs the disadvantages, justifying the never-ending pursuit for smaller probes.

Chapter 2. Characterization of multifunctional electrochemical probes with nanometer dimensions

Nanometer sized electrochemical probes, simple and multifunctional alike, can be tricky to characterize due to its small critical dimensions. Although most electrodes can be characterized by electrochemical methods through the acquisition of an electrochemical information that directly correlates to critical geometrical information of the electrode (electrode surface radius, surface area, among others), for electrodes in the nanometer size range, the geometry of the electrode area is not the only factor influencing the electrochemical response of a given electrode, with the geometry of the insulating or supporting material (RG) also greatly affecting the response. Hence, it is critical that the whole electrode geometry is elucidated by using imaging techniques such as SEM or TEM. The characterization of electrodes by those imaging techniques is usually challenging as most SEM and TEM equipments are not suited to hold large samples. The imaging of nanometer sized electrodes and electrochemical probes is even more challenging as their critical features and dimensions are in the nanometer range, which requires high magnification and usually low working distances, but they still present large macroscopic bodies. To satisfy those two conditions a custom made sample holder (for SEM and TEM) is required.

This chapter was published as an article in *PLOS ONE* and describes a cost effective alternative for fabricating custom sample holders using 3D printing techniques. This approach enables the quick and inexpensive fabrication of sample holders with specific features, allowing high resolution imaging and the characterization of nanometer sized electrodes for SEM and Transmission-SEM.

3D printing scanning electron microscopy sample holders: A quick and cost effective alternative for custom holder fabrication.

Gabriel N. Meloni and Mauro Bertotti*

*Corresponding author

2.1 Abstract

A simple and cost effective alternative for fabricating custom Scanning Electron Microscope (SEM) sample holders using 3D printers and conductive polylactic acid filament is presented. The flexibility of the 3D printing process allowed for the fabrication of sample holders with specific features that enable the high-resolution imaging of nanoelectrodes and nanopipettes. The precise value of the inner semi cone angle of the nanopipettes taper was extracted from the acquired images and used for calculating their radius using electrochemical methods. Because of the low electrical resistivity presented by the 3D printed holder, the imaging of non-conductive nanomaterials, such as alumina powder, was found to be possible. The fabrication time for each sample holder was under 30 minutes and the average cost was less than \$0.50 per piece. Despite being quick and economical to fabricate, the sample holders were found to be sufficiently resistant, allowing for multiple uses of the same holder.

2.2 Introduction.

Scanning Electron Microscopy (SEM) is a powerful analytical tool for studying chemical composition, material structure and morphology on the submicron level and thus has been widely used to characterize new materials with a broad applications spectrum.^{65,66} Although SEM is a well-established technique for characterizing nanomaterials, such as nanoparticles, it has been used lately to characterize samples that have macroscopic physical dimensions, such as electrode surfaces, ultramicroelectrodes

(UME), nanoelectrodes and nanopipettes. Although other techniques, such as Atomic Force Microscopy (AFM)⁶⁷, Transmission Electron Microscopy (TEM)²⁵ and Scanning Transmission Electron Microscopy (STEM)⁵⁷ can be used to characterize those samples, SEM is still the “first line of defense” as it is widely available, can give results fairly fast, and can still give important information such as the outer body dimensions of electrodes,^{46,68–70} imperative for a precise calculation of the radius of glass in UMEs.³⁷ Although some of those parameters can be estimated by electrochemical methods,^{23,24,38,71} without the knowledge of the precise geometry of the samples one can, misleadingly, interpret the electrochemical results wrongly and assume false characteristics for the electrode in hand.⁷²

The characterization of nanoelectrodes, UMEs and nanopipettes with SEM requires the use of especial custom-made sample holders that can accommodate the macroscopic body of the electrodes and still allow the nanometer features to be studied. Despite looking at first hand as a simple problem to solve, the manufacturing of specialized sample holders can be a time demanding and costly process, requiring the use of specialized tools and trained staff. In that sense, 3D printers can be powerful tools, speeding up the process and decreasing costs by closing the gap between the end user and manufacturing process. Although there are several 3D printing techniques available, Fused Deposition Modeling (FDM) 3D printers are finding more space on the 3D printing community, mainly due to the decrease in price of the printers, low cost and wide variety on the printing material (thermoplastic polymer filament) and increased resolution, now on the orders of tens of micrometers of layer height.⁷³ Not surprisingly, the use of 3D printers for fabrication of custom parts for research laboratories has been reported with increased frequency.^{74–80}

Herein an alternative approach for fabricating custom SEM holders using FDM 3D printers and free 3D Computer Aided Design (CAD) software is presented. The fabrication of custom sample holders with a cost and time effective technique, such as 3D printing, can benefit a broad range of research subjects being of especial interest for samples that cannot be accommodated on standard sample holders. Although the fabricated SEM holders herein presented are designed aiming at the characterization of ultramicroelectrodes and nanoelectrodes for electrochemical applications, the fabrication method developed (and the 3D printed holders) can be applied in a large variety of samples, including nanostructured materials, as demonstrated further. The proposed fabrication method and the application of low cost SEM sample holders is also an interesting alternative for research and teaching centers.

2.3 Materials and methods

All sample holders were designed according to the specific need using the free 3D CAD software 123D design (Autodesk, USA). Once finished, the design was imported to a Cliever CL1 Black (Cliever, Brazil) FDM 3D printer using its proprietary software. The printing speed was set to 150% of the maximum printer speed (value not specified by the manufacturer), bed temperature to 65° C and extruder temperature to 210° C for all prints. The printing infill percentage influence on the final printed pieces performance is explored further in the manuscript. All holders were printed from 1.75 mm diameter electrical conductive carbon impregnated polylactic acid (PLA) filament (Proto-pasta, USA). SEM images were acquired using a JSM-7401F FEG-SEM instrument (JEOL, JPN). The electrochemical measurements were performed using an Autolab PGSTAT 128N bipotentiostat (Metrohm Autolab, Utrecht, The Netherlands). All electrodes and nanopipettes were fabricated according to well-known methods described in the literature.^{25,44}

2.4 Results

2.4.1 Electric conductivity of 3D printed parts

Despite of the application, a common feature desired in all SEM holders is the ability to conduct, at some extent, electrical current (*i.e.* low electrical resistance). This is mainly to create an electrical connection between the sample holder and the SEM chassis which is held at ground potential. The connection avoids the build-up of charge in the sample and sample holder by draining it to ground through the sample holder. This increases the imaging resolution as charged surfaces will create distortions that could yield misinterpretation of the SEM image.⁸¹ To avoid such issues, a commercial carbon impregnated conductive PLA filament was used for printing the sample holders. Although the electrical resistivity (ρ) of the filament is specified by the manufacture, it regards to the resistivity of a cross section of a solid piece of PLA which is not true for most 3D printed parts by FDM. Most 3D printed parts are hollow or partially filled with a honeycomb-like structure (infill percentage of the 3d printed piece can be adjusted on most printers), as can be seen in Figure 2.1. This serves two purposes, one is saving printing time and the other is saving printing material. Hence, to proper measure the electrical resistivity, 1 cm² sided cubes were printed with different infill percentages (20, 40 and 100) and used as test pieces.

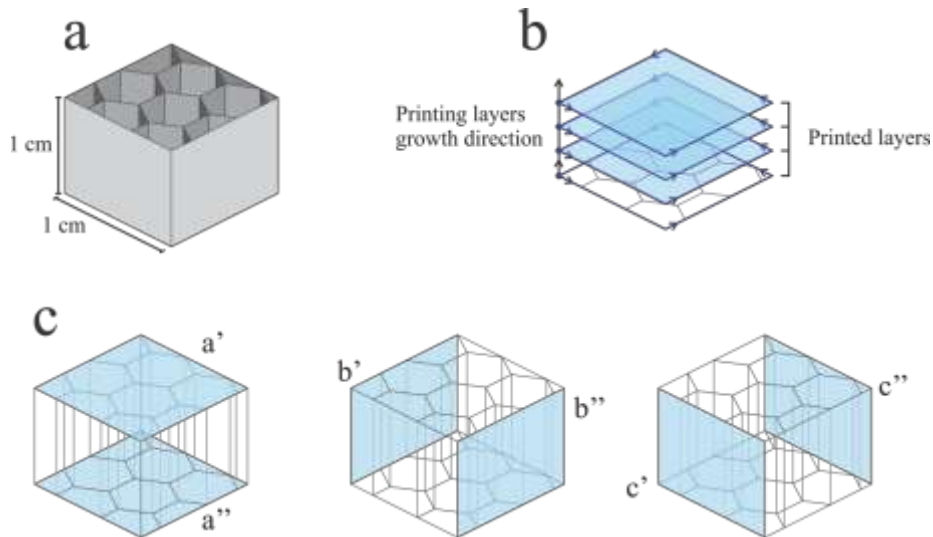


Figure 2.1. Schematic representation of the 3D printed 1 cm^3 test pieces. (a) Representation of a test piece with an open top showing the internal infill geometry. (b) Schematic representation of the printing path during the printing of the test pieces, highlighting the staggered layers. (c) Different pairs of opposite faces whose orientation regarding the internal infill geometry are shown in blue.

To measure the resistivity, two opposite faces of each of the test pieces were coated with a layer of silver conductive ink (Figure 2.2), reducing the contact resistance for the resistivity measurements. The opposite faces were connected to the leads of a potentiostat and the potential across both surfaces was scanned between 0.2 V and -0.2 V. The slope of the resulting Current vs. Potential curve is the inverse of the electrical resistance of the test piece (Ohm's law) and can be used to calculate its resistivity.

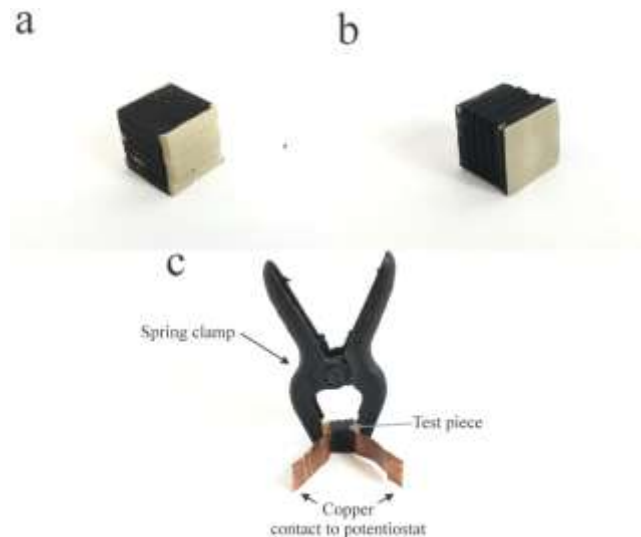


Figure 2.2. 3D printed test pieces with different infill percentages for electrical resistivity calculation showing faces painted with conductive silver ink to avoid contact resistance on (a) faces perpendicular to the printed layers and (b) face parallel to the printing layers. (c) setup for connecting the test pieces to a potentiostat to measure the electrical resistivity. Copper sheets act as a contact between the silver painted faces and the potentiostat. Spring clamp ensures constant pressure on the faces during all the measurements.

As can be seen by inspection of Table 2.1, the resistivity of a test piece with a common used infill percentage (20%) changes in a large extent depending on which of the 3 pairs of opposite faces are used in the measurement. The observed difference may rely on the non-uniformity of the 3D printed structure (Figure 2.1a). Although it is straightforward to see that an increase in infill percentage would result in a decrease in resistivity, as shown in Table 2.1 for a' and a'' face pairs, one can see that a 100% infill piece not only has a resistivity much higher (around $110 \Omega \text{ cm}$) than a solid piece of the conductive polymer ($15 \Omega \text{ cm}^{82}$), but also has a higher resistivity than the one measured between faces b' and b'' and faces c' and c'' of the 20% infill pieces. This is due to the additive fabrication method used, according to which the pieces were fabricated by adding a series of stacked layers as demonstrated in Figure 2.1b. This results in a material that despite being a solid piece of PLA is still anisotropic due to the poor

binding between each of the printed layers. This is less of an issue when the resistivity measurements are taken for faces that are perpendicular to the printed layers (b'/b'' and c'/c''), as those are printed as a continue string ensuring good electrical resistivity.

Table 2.1. Electrical resistivity measured in 3D printed 1 cm^3 test pieces with different infill percentages. Measurements were taken between different faces of the test cubes.

Infill (%)	Face pairs	Electrical resistivity ($\rho/\Omega\text{ cm}$)
20	a' and a''	129.46 ± 0.01
20	b' and b''	84.3 ± 0.1
20	c' and c''	61.07 ± 0.05
40	a' and a''	114.20 ± 0.07
100	a' and a''	109.98 ± 0.02

Double side conductive carbon tape, which are commonly used for fixing samples onto sample holders for SEM imaging, has a sheet resistivity, as stated by the manufacture, ranging from $100\text{ k}\Omega/\text{sq}$ to $250\text{ k}\Omega/\text{sq}$.⁸³ Assuming uniformity on the conductive carbon layer, the electrical resistivity (ρ) can be calculated from the sheet resistivity by multiplying the later by the thickness of the sheet. With a layer thickness of $125\text{ }\mu\text{m}$, the electrical resistivity calculated ranges from $1250\text{ }\Omega\cdot\text{cm}$ to $3125\text{ }\Omega\cdot\text{cm}$, one order of magnitude higher than the 3D printed parts.

2.4.2 3D printed SEM sample holders

Although the 100% infill test piece presented the lower resistivity for measurements taken across faces a' and a'' and a lower resistivity is always a desirable characteristic for SEM sample holders, the printing time and material consumption for printing 100% infill custom sample holders would make this unreasonable. Also, as the binding between layers is not perfect, pockets of air could be trapped between them, which could cause, in the worst case scenario, a violent decompression of the holder when placed in a vented SEM chamber. An easy way around those issues is to design a bottomless sample holder that exposes the infill geometry, thus allowing for the holder

to be safely vented inside an SEM chamber. The infill percentage value is a trade between electrical resistivity and printing time and material cost and should be chosen according to the printer used. Accordingly, an infill percentage of 50% was chosen in this work for the 3D printed SEM sample holders. A set of custom made 3D printed SEM sample holders for imaging UME, nanoelectrodes and nanopipettes can be seen in Figure 2.3.

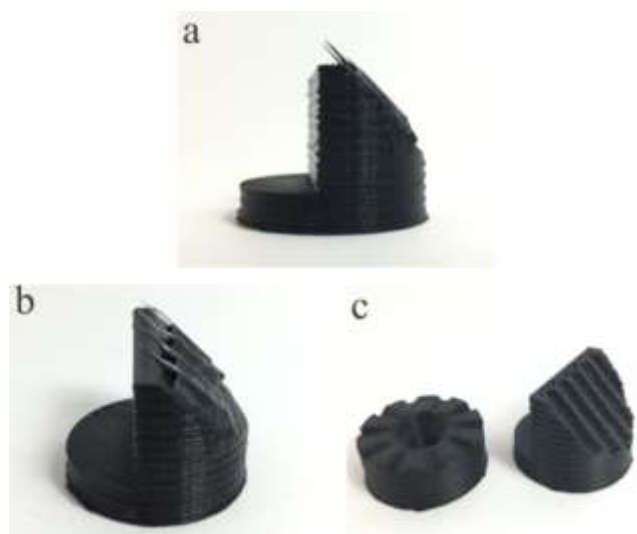


Figure 2.3. (a) and (b) custom designed 3D printed conductive 45° SEM sample holder for UME and nanopipettes. Nanopipettes attached using conductive carbon tape. (c) Couple of custom designed and 3D printed SEM sample holders showing specific features for holding UMEs and nanopipettes.

The 3D printed holders shown in Figure 2.3 were designed to have specific features that allow for a better positioning and imaging of the electrodes, such as the grooves that allow for precisely positioning each individual electrode. Although a metal sample holder can be made and machined to have the same features, its fabrication can hardly be achieved in a research laboratory as it demands the use of a machine shop and results in time consuming and expensive processes. The total printing time for each of the holders shown in Figure 2.3 was less than 30 minutes, which is a short period of time to fabricate a finished and functional product.

The fabricated sample holders were used to image double barrel (teta) nanopipettes intended to be used as multifunctional probes for electrochemical imaging experiments. This multifunctional nanoprobes can be applied on single crystal analysis,⁶⁸ single cell^{17,21,51,84} and single nanoparticle imaging,^{9,53,85} among others. The knowledge of the critical dimensions of those nanopipettes is crucial for precise characterization,^{25,86} being SEM one of the few alternatives for acquiring such information. The nanopipettes were imaged using the 45 degrees 3D printed sample holder (Figure 2.3) and the obtained images can be seen in Figure 2.4.

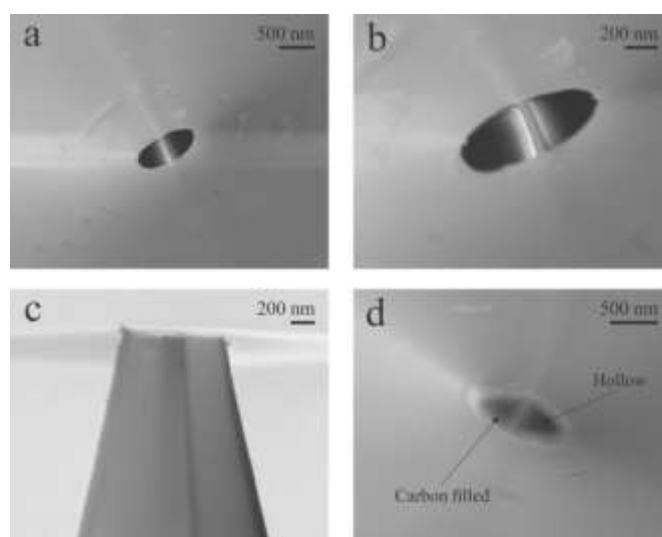


Figure 2.4. SEM images of nanopipettes and nanoelectrodes. (a) and (b) top view of a double barrel pipette showing both openings unblocked. (c) Side view of a double barrel pipette. (d) Top view of a dual-function pipette based electrode showing selective carbon deposition in only one barrel. Accelerating voltage = 5 kV.

Even though the samples are not conductive (Figure 2.4a, 2.4b and 2.4c) and were not coated with a conductive layer, clear images of the electrodes with resolution in the nanometer range were obtained using the 3D printed sample holders with minimal charging effects. The pipette opening dimensions and the overall tip geometry can be easily measured from the acquired images, allowing for a precise electrochemical calculation of the pipette opening radius as described further. The selective deposition

of pyrolytic carbon in only one of the barrels of a double barrel pipette, during the fabrication of a dual function nanoelectrode,¹⁶ can also be clearly seen in Figure 2.4d. The low resistivity of the printed holders allows not only for electrodes to be imaged but also nanostructured materials. Despite not being the focus of this manuscript, as it normally does not require customized sample holders, the characterization of nanomaterials can also be performed using the 3D printed sample holders, even in non-conductive samples, such as alumina powder, as shown in Figure 2.5. Despite the presence of some charging effect (more significant in the highest alumina density sites, as seen in Figure 2.5b), which is expected when imaging non-conductive and uncoated substrates, they still present a reasonable resolution and the size and shape of the alumina particles can be easily extracted from them.

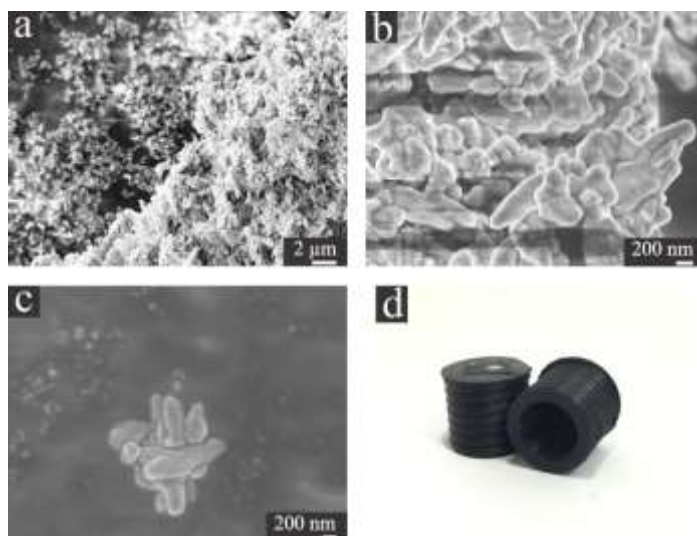


Figure 2.5. (a) and (b) SEM images of a 300 nm alumina powder used for polishing electrodes at different magnification. (c) Close-up of a single particle cluster showing the details of the particle surface. (d) 3D printed SEM stub sample holders used for acquiring the alumina powder images. Accelerating voltage = 3kV.

2.4.3 Nanopipette radius calculation

It is largely accepted that the radius of nanopipettes can be electrochemically calculated from the resistance to the ionic flow across the pipette opening when a bias potential is applied between two reference electrodes submerged in an electrolyte solution, one placed inside the pipette barrel and the other in the bulk solution. Although this is true, the resistance to ionic flow is not only a function of the pipette radius, it is also a function of the conductivity of the electrolyte solution and the pipette inner semi cone angle (Figure 2.6a). Equation 2.1 describes the relationship between those parameters and the pipette radius²⁵.

$$R_p = \frac{1}{K \pi r_i \tan \beta} + \frac{1}{4 K r_i} \quad (\text{Equation 2.1})$$

Where R_p is the resistance to ionic flow across the pipette opening, K is the electrolyte solution conductivity, r_i is the pipette opening radius and β is the inner semi cone angle.

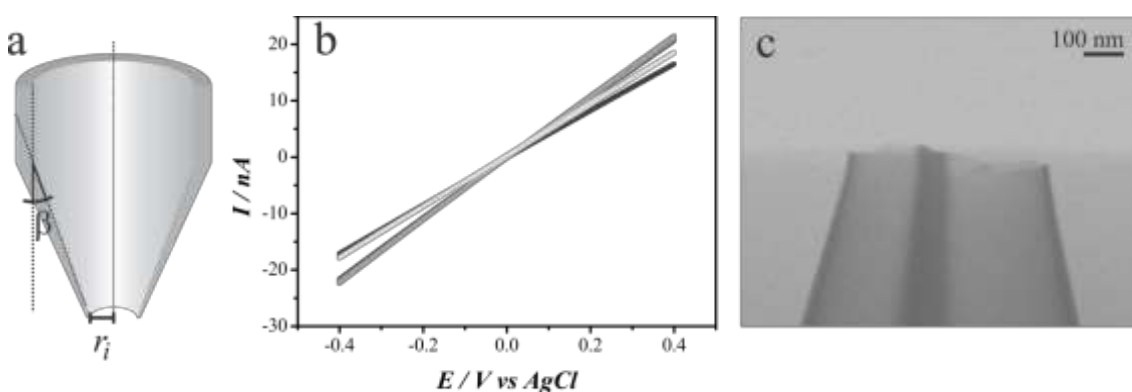


Figure 2.6. (a) Representation of a cross section of a nanopipette showing the opening radius and the inner semi cone angle, β . (b) Polarization curves recorded with 5 different nanopipettes in a $0.1 \text{ mol L}^{-1} \text{ KCl}$ solution using a pair of AgCl coated silver wires as Quasi-reference counter electrodes (QRCE). Scan rate = 0.1 V s^{-1} . (c) Transmission-SEM image of a nanopipette. Accelerating voltage = 15 kV.

The resistance across the pipette opening is easily calculated by recording a polarization curve. For such, the pipette was filled with 0.1 mol L⁻¹ KCl solution and a AgCl coated silver wire was inserted inside the barrel to act as a quasi-reference counter electrode (QRCE). Another AgCl coated silver QRCE was placed in the bulk of the solution. Using a potentiostat, the potential across those two QRCE was scanned between -400 mV and 400 mV at 100 mV s⁻¹. The resulting polarization curves for 5 different nanopipettes can be seen in Figure 2.6b. The slope of the linear fit of the data points is the inverse of the resistance across the pipette opening (R_p) (Ohm's law) and can be used to calculate the nanopipette radius using equation 2.1. The inner semi cone angle value cannot be calculated by electrochemical methods, hence the need for using imaging techniques, such as SEM, for proper characterizing nanopipettes. Although an estimative of the inner semi cone angle can be made from the outer semi cone angle using SEM images of the side of nanopipettes (Figure 2.4c), this would not be very precise as the inner and outer pipette wall do not taper parallel to each other, hence a technique capable of imaging the inner wall of the nanopipette, such as electron transmission technique, is better suited for acquiring this information.²⁵

Despite TEM is the most appropriate technique for imaging the inner features of a nanopipette, the macroscopic nature of the nanopipettes body poses as an obstacle as imaging such sample would require custom made holders or time demanding sample preparation procedures such as Focused Ion beam (FIB) milling. As TEM and FIB are not as commonly available as SEM, one alternative electron transmission technique for acquiring images of the inner portion of a nanopipette is Transmission-SEM (T-SEM) which, usually, requires the use of an especial sample holder to acquire transmission images from a SEM equipment.⁸⁷ Due to the electron transparency nature of the nanopipette walls (only a couple nanometers thick), T-SEM images with an adequate

resolution were obtained by simply laying the nanopipettes over a regular, “stub” (Figure 2.5d), sample holder. Figure 2.6c shows a T-SEM image acquired using a 3D printed SEM holder where the internal features of the nanopipette (such as the wall thickness and the inner semi cone angle) can be easily seen and measured. Using the values obtained from Figure 2.6 b and c ($\beta = 8.5^\circ$), the nanopipette barrel radius can be calculated as ranging between 108 nm and 126 nm, averaging at 117 nm. The values obtained are expected according to the fabrication procedure and are in accordance with SEM and T-SEM images. The difference among the obtained values is not unusual for such fabrication procedure, hence the need for proper characterization of the pipettes.⁸⁶

2.4.4 3D printed sample holders durability

Despite being 3D printed out from a thermoplastic polymer, the 3D printed sample holders were found to be extremely durable and able to be reused several times and for different samples. The irregular surface of the printed sample holders (due to the presence of build lines, typical of FDM 3D printing) limits the adhesion of carbon and copper conductive tapes, which are commonly used to fix samples to holders, making it easy to remove them completely from the holders without leaving much residue. Although soluble in acetone⁸⁸, the PLA holders were able to endure an overnight acetone bath without presenting much damage other than partial delamination of the first printing layers (data not shown), demonstrating that they can be cleaned with acetone prior to reuse. No apparent damage was observed by interaction with the electron beam during or after the imaging experiments, even when using higher accelerating voltages (15 kV) necessary for the T-SEM experiments. Granting their durability, the 3D printed holders are much softer than any other metal fabricated sample holder and care against mechanical damage should be taken.

2.4.5 3D printed sample holders price

The 3D printed sample holders used in the SEM imaging and shown on Fig. 3 had a diameter of 25 mm and an infill of 50%. Although they differ in height and geometry, their mass averaged at 4.1 g. With the retail price (march 2017) of \$49.99 USD for a 500 g spool of conductive PLA, each holder would have an average material cost of \$0.41 USD.

2.5. Conclusion

Using commercial 3D printers, commercial carbon impregnated PLA filament and free 3D cad software, we were able to fabricate custom designed fully functional SEM sample holders for high resolution imaging of nanopipettes and nanoelectrodes. Several different sample holders were constructed by using such fast and simple process, each with a specific use and design feature. The conductive nature of the printing material and the chosen printing parameters allowed the use of 3D printed sample holders for imaging nanostructured materials with satisfactory resolution. Although the initial cost of acquiring a 3D printer can be high, the low price of the printing material result on sample holders that cost (on average) less than \$0.50 in material, making this an attractive alternative. Despite been made out of PLA, the printed holders were found to be surprisingly durable and able to be re-used several times even after cleaning with diluted acetone solution.

2.6. Acknowledgements

The research upon which this article was based was supported by Conselho Nacional de Desenvolvimento Científico e Tecnológico (CNPq: grant number 48383/2012-2 for GNM) and FAPESP (Fundação de Amparo à Pesquisa do Estado de

São Paulo, grant number 2015/20776-9), to which the authors are very grateful for the financial support.

Chapter 3. Ring-disc microelectrode towards glutathione electrochemical detection

Ring-disc microelectrodes are simple multifunctional probes, presenting a straightforward and simple fabrication procedure. Nevertheless, despite the simplicity, they can be extremely powerful towards the elucidation of complex systems and the acquisition of topography-free electrochemical information. The presence of two distinct electrodic surfaces (ring and disc) opens the possibility to simultaneously monitor two distinct electroactive species granting a higher information density to experiments using such probes. The presence of two distinct electrodic surfaces also enables such multifunctional probe to be used as a generation/collection system, allowing the investigation of non-electroactive species by monitoring the collection efficiency of the system. Non-electroactive species that can react with the electrochemically generated species at the disc, during its diffusion towards the ring, will affect the system collection efficiency. As the collection efficiency is also affected by the separation between the electrochemical probe and the substrate being investigated (in a SECM experiment), topography-free information can be acquired.

This chapter was published as an article in *Electroanalysis* and describes the use of ring-disc microelectrodes to electrochemically detect and visualize the transport of glutathione, an important endogenous antioxidant, across an impermeable membrane. Glutathione electrochemical detection is challenging as it is not electroactive at bare electrodic surfaces over reasonable over-potentials. By using a redox probe (acetaminophen) and relying on the glutathione interference on the system collection efficiency, it was not only possible to electrochemically monitor the antioxidant, but also image (without topography influence) its transport across a membrane.

Ring-disc microelectrodes towards glutathione electrochemical detection

*Gabriel N. Meloni and Mauro Bertotti**

Instituto de Química - USP, São Paulo, SP, Brazil

*Corresponding Author

3.1 Abstract

An alternative approach for space-resolved glutathione (GSH) detection using a ring-disc microelectrode and an appropriate electroactive probe (acetaminophen) is reported. Acetaminophen is electrochemically oxidized at one of the electrodes and a fraction of the reaction product (N-acetyl-p-quinoneimine) diffuses to the other, where it is detected. The collection efficiency value is dependent on the concentration of glutathione in solution, which consumes N-acetyl-p-quinoneimine during its transit between the disc and the ring. Collection efficiency values close to 100% were obtained by confining the electroactive species in a gap ($< 2 \mu\text{m}$) that resembles a thin layer cell in a SECM configuration. The proposed indirect method was used to image the transport of GSH across an impermeable membrane in a SECM experiment. The method proved to be useful as a proof of concept for space-resolved GSH electrochemical detection and a topography independent electrochemical image was acquired.

3.2 Introduction

Glutathione (GSH) is one of the most important endogenous anti-oxidants found in cells⁸⁹. It is responsible for maintaining the redox state of both prokaryotic and eukaryotic cells, preventing cellular damage by oxidative species such as free radicals and reactive oxygen species (ROS). GSH is a tri-peptide in the form *Glu-Cys-Gli* that

takes part in several cellular processes such as metabolism, differentiation, detoxification and apoptosis. Glutathione can be converted to glutathione disulfide (GSSG) through a chemical reaction with reactive oxidative species in the cellular medium, forming an important defense mechanism against oxidative agents⁸⁹⁻⁹¹. Studies show that a change in the homeostatic concentration of GSH at the cellular level is a factor that can lead to the development of diseases such as cardiovascular diseases, Alzheimer's disease, diabetes and cancer^{89,92,93}.

Glutathione detection has been performed, mostly, by high performance liquid chromatography (HPLC) due to its high sensitivity and selectivity⁹⁴⁻⁹⁶. Despite its satisfactory performance, HPLC detection presents some drawbacks such as the need of sample preparation, high cost and long analysis time. An alternative that could potentially overcome some of those drawbacks is the use of electrochemical techniques. As glutathione does not present electrochemical response over bare electrode surfaces, all electrochemical methods for its detection rely on modified electrode surfaces⁹⁷⁻¹¹⁰ or the use of mediators^{111,112}. Lowinsohn *et al* reported the use of acetaminophen, a readily available and well-studied pharmaceutical compound, as a mediator for the electrochemical detection of glutathione in solutions with physiological pH¹¹³.

The use of electrochemical techniques for glutathione detection eliminates the need for sample preparation, allowing for "*in vivo*" detection of this tri-peptide. In that sense, microelectrodes are a powerful tool because they can be fabricated with physically small dimensions and a time and space resolved electrochemical response is generated, allowing the application of this kind of sensor in single cell analysis^{7,114-117}. For instance, the advantageous features of microelectrodes have been explored in studies involving the excretion of thiodione, an electroactive conjugate between

menadione and glutathione, at the single cell level by means of Scanning Electrochemical Microscopy (SECM) ^{30,118}.

In the present paper we investigate the application of a ring-disc microelectrode for indirect electrochemical sensing of glutathione using acetaminophen as an electroactive probe. The proposed approach is a proof of concept for space-resolved glutathione detection that could be potentially useful for Scanning Electrochemical Microscopy application in single cell analysis.

3.3 Materials and Methods

3.3.1 Chemicals

All the solid reagents were of analytical grade and were used without further purification. Phosphate buffer saline (PBS) pellets, acetaminophen, glutathione, potassium ferricyanide and potassium chloride were obtained from Sigma-Aldrich (St. Louis, MO, USA). All solutions were prepared using deionized water (Millipore, Billerica, MA, USA). The PBS solution was prepared by dissolving an entire PBS pellet in an appropriate amount of deionized water.

3.3.2 Instrumentation

All the electrochemical measurements were performed using an Autolab PGSTAT 128N bipotentiostat (Metrohm Autolab, Utrecht, The Netherlands) and a 4 electrode system consisting of 2 working electrodes (ring and disc), a platinum auxiliary electrode and a Ag/AgCl (saturated KCl) reference electrode. For the electrochemical images, the above mentioned potentiostat was coupled to a Sensolytics (Sensolytics, Bochum, Germany) SECM working station with high-resolution option.

3.3.3 Ring disc microelectrode fabrication

Different approaches have been used to fabricate ring-disc microelectrodes, which are essentially based on lithography, chemical vapor deposition, physical vapor deposition and a few other novel procedures^{56,119–122}. In this work, ring-disc microelectrodes were fabricated from platinum disc-shaped microelectrodes with 25 μm diameter and a RG value of 10 (RG being the ratio between the radius of the overall tip, including the glass, and the radius of the active microdisc) that were made using a P-2000 Flaming/Brown Micropipette Puller (Sutter Instrument Company, USA) according to a protocol reported in the literature^{22–24}. The ring part of the electrode was fabricated by coating a 400 nanometer gold layer onto the glass body of the microelectrode using a HHV Auto306 sputtering equipment (HHV Ltd., Crawley, UK). The electrical contact of the outer gold layer was performed by attaching a copper wire using silver epoxy glue (Epoxy Technology, USA). The outer layer was then isolated using a colorless nail varnish. The fabricated electrode was polished using fine grit sand paper to expose a cross section with the disc shape platinum electrode and the ring shaped gold electrode. A schematic drawing of the fabrication process and images of the constructed device are shown in Figure 3.1.

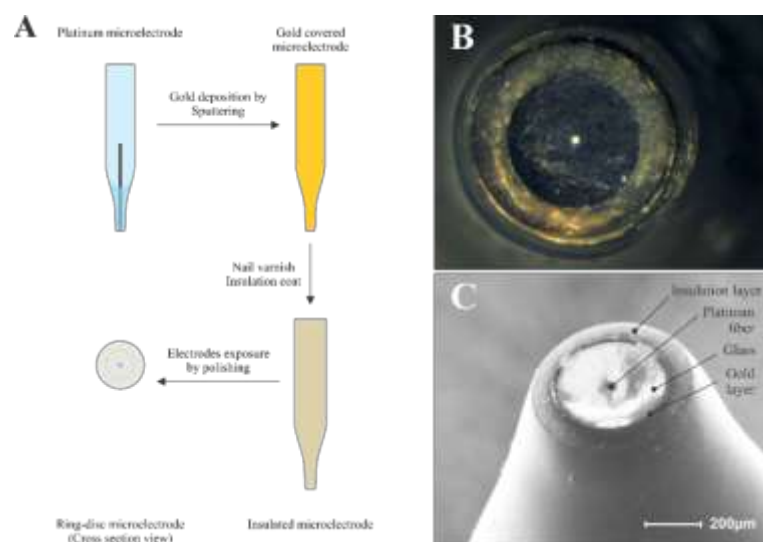


Figure 3.1. Ring-disc microelectrode fabrication process (A). Optical microscopy image (B) and SEM image (C) of the ring-disc microelectrode fabricated by the proposed method.

All ring-disc microelectrodes were tested regarding the electrochemical behavior by performing a series of cyclic voltammetry experiments in a 15 mmol L⁻¹ potassium ferricyanide solution (data not shown). The electrodes were repeatedly polished until the expected electrochemical behavior was noticed (sigmoidal curve with low hysteresis).

3.4 Results

3.4.1 Ring-disc microelectrodes

Figure 3.2a shows results on the use of the proposed ring-disc microelectrode as a generation/collection system using ferricyanide as a probe and a low collection efficiency (at around 15%) was obtained. Although not unusual for ring-disc microelectrodes¹²², this low value can be attributable to the fact that the system does not rely on any hydrodynamic force to transport mass from one electrode to the other, radial diffusion from the disc to the ring being the only mechanism of transport. Besides, as it can be seen in Figure 1, the disc/ring inter-distance is significantly large, approximately 125 µm (the radius of the glass), hence a considerable amount of

material is lost to the bulk solution instead of being primarily collected at the ring. This low collection efficiency value is in agreement with theoretical predictions, according to which such value decreases as the inner and outer ring radii are both increased ¹²³.

Although the collection efficiency could be increased by decreasing the disc/ring inter-distance during the fabrication processes (for instance, by reducing the radius of the glass body of the platinum microelectrode prior to gold deposition), an alternative is to decrease the amount of material lost to bulk solution, hence promoting the arrival of more material to the collector electrode. This can be performed by confining the material close to the electrode by approaching it to an inert surface forming, as a consequence, a small thin layer cell in a similar way as the hindered diffusion phenomena in SECM ¹²⁴. Although the influence of the tip-substrate separation has been already investigated for SECM Substrate Generation/Tip Collection (SG/TC) experiments ¹²⁵, the same study for a ring-disc microelectrode is more complex as it depends on a handful of parameters such as the ring/disc inter-distance, ring thickness and disc radius and as such it is unique for different electrode geometries. A quick comparison between the currents recorded in bulk solution (Figure 3.2a) and at a distance typically used for SECM imaging, i.e. 5 μm from the substrate (Figure 3.2b), shows that the collection efficiency, calculated as the ratio of the steady state currents, changes dramatically from approx. 15% to almost 100% when the electrode is brought closer to the substrate.

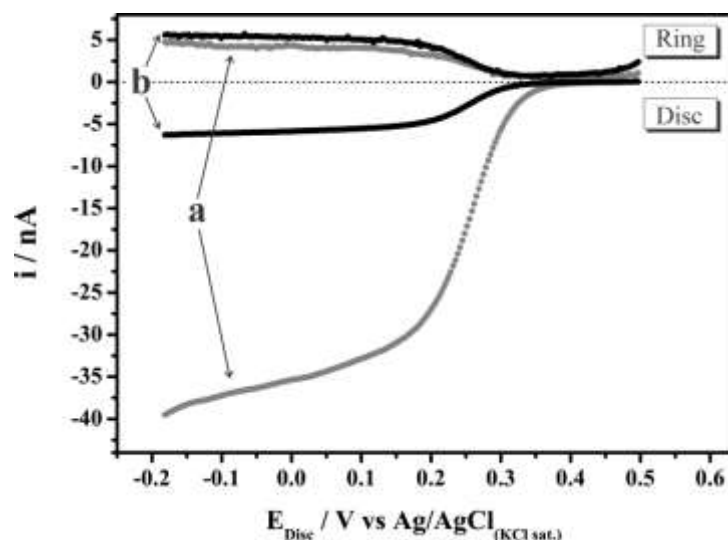


Figure 3.2. Generation/Collection experiment recorded with a ring-disc microelectrode in a 15 mmol L^{-1} potassium ferricyanide + 0.1 mol L^{-1} KCl solution with the microelectrode positioned at (a) the bulk solution and (b) at $5 \mu\text{m}$ from an inert substrate. Potential scanned at the disc in the range 0.5 to -0.2 V. Ring polarized at 0.5 V. Scan rate: 5 mV s^{-1} .

In order to investigate with more details the influence of the tip-substrate separation on the fabricated electrode, a SECM Disc Generation/Ring Collection (DG/RC) experiment was performed in a 15 mmol L^{-1} potassium ferricyanide + 0.1 mol L^{-1} potassium chloride solution. For such experiment, an electroactive species is electrochemically produced at the disc electrode (generator) and a portion of it is transported by diffusion to the ring electrode (collector), where it can be electrochemically detected. The electrode was approached towards an insulating substrate (silicon wafer) and the generation and collection currents were recorded for different tip-substrate separations. Collection efficiency values were calculated for different tip-substrate separations, as can be seen in Figure 3.3. The results are similar to those previously reported¹²¹, although the absolute values at each distance differ due to differences between the systems geometry. The SECM DG/RC results shown in Figure

3.3 demonstrate that the collection efficiency can be easily controlled by adjusting the tip-substrate separation and the importance of this feature will be discussed further.

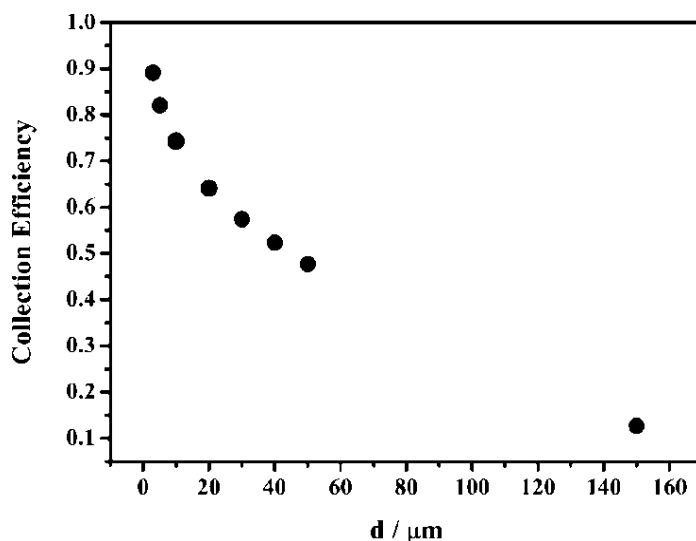


Figure 3.3. SECM DG/RC collection efficiency values at different tip-substrate separations. Experiments were carried out in 15 mmol L^{-1} potassium ferricyanide + 0.1 mol L^{-1} KCl solution. $E_{disc} = -0.1 \text{ V}$, $E_{ring} = 0.5 \text{ V}$.

3.4.2 Glutathione detection

As glutathione is not electroactive at bare electrode surfaces at relatively moderate potentials, alternative methods have been reported using modified electrodes or redox mediators in order to allow for glutathione detection. In a recent approach, acetaminophen was used as a redox mediator after its immobilization onto electrodic surfaces¹¹³. Acetaminophen (APAP), also known as Paracetamol, is a well-studied compound that can undergo oxidation over bare electrode surfaces. The oxidation product of acetaminophen, N-acetyl-p-quinoneimine (NAPQI), can react with glutathione in a redox reaction leaving glutathione disulfide and acetaminophen as products. As the extent of the acetaminophen regeneration is a function of the glutathione concentration, both signals, the acetaminophen oxidation and the N-acetyl-

p-quinoneimine reduction, can be indirectly used as indication of the glutathione concentration as can be seen by inspection of Figure 3.4.

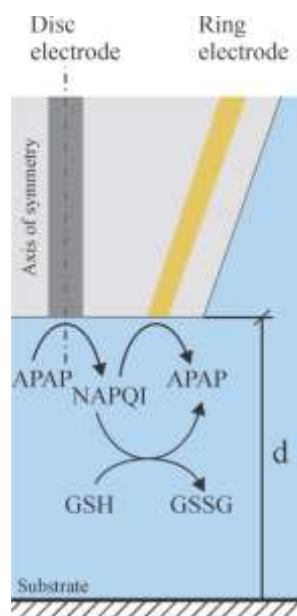


Figure 3.4. Schematic representation of the indirect detection of GSH at a ring-disc microelectrode positioned over an inert substrate. Tip-substrate separation denoted as “d” on the representation.

To apply this method for electrochemical detection of glutathione using microelectrodes, certain issues must be taken into account. Owing to the high mass-transport rate at microelectrodes, electrocatalytic cycles are poorly developed, hence the current enhancement corresponding to the APAP oxidation caused by the presence of glutathione would be negligible. On the other hand, the signal decrease associated with the NAPQI consumption by glutathione can still be used in a typical diffusion layer titration configuration^{126,127}.

To demonstrate the applicability of the fabricated ring-disc microelectrode towards the electrochemical detection of glutathione, the sensor was positioned over an insulating substrate (25x25 mm silicon wafer) and experiments were performed in an

electrochemical cell containing 1 mmol L⁻¹ APAP in 10 mmol L⁻¹ PBS solution (pH 7.4). The disc was biased at 0.9 V, a potential value where APAP is oxidized at diffusion-limited conditions with the electrogeneration of NAPQI, and the ring was held at -0.2 V in order to monitor the reduction of NAPQI back to APAP. Successive additions of glutathione were made to the electrochemical cell, resulting in solutions with GSH concentrations of 30, 60, 90, 120, 150, 180 and 210 μmol L⁻¹, which lie in a typical GSH concentration range found in cellular environments¹¹¹. The solution was stirred after every addition of GSH solution to promote homogenization. This was accomplished by withdrawing the microelectrode from the substrate towards the bulk solution before every addition of GSH, hence the solution could be properly stirred without any risk of damaging the microelectrode. The electrode was then brought to the adequate tip-substrate separation from the substrate prior to every measurement.

The addition of GSH to the working solution results in a decrease of the collection efficiency of the ring-disc microelectrode because of the decrease of the recorded reduction current at the ring, as shown in Figure 3.5A. This is in agreement with the fact that glutathione can chemically react with NAPQI during its transport from the generator electrode to the collector (Figure 3.4). As a consequence, the amount of NAPQI reaching the collector is lower and dependent on the concentration of GSH in solution.

As the quantification of GSH is a function of the collection efficiency, which depends on the tip-substrate separation (see Figure 3.3), it is straightforward to examine the influence of the distance between the tip and the substrate on the analytical parameters involving the GSH determination. Figure 3.5A shows the plot of the ring current as a function of GSH concentration for two tip-substrate separations: 30 (curve i) and 5 μm (curve ii). Two main findings can be noticed: firstly, in the absence of GSH

the collection current is higher when the ring-disc microelectrode is closer to the substrate, because less NAPQI is lost to the bulk solution. Secondly, the influence of the GSH concentration on the current at the ring (sensitivity) is more pronounced at a lower tip-substrate distance (curve ii), as the generated product at the disc (NAPQI) is not allowed to diffuse away to the bulk solution, hence the reaction zone is closer to the ring electrode.

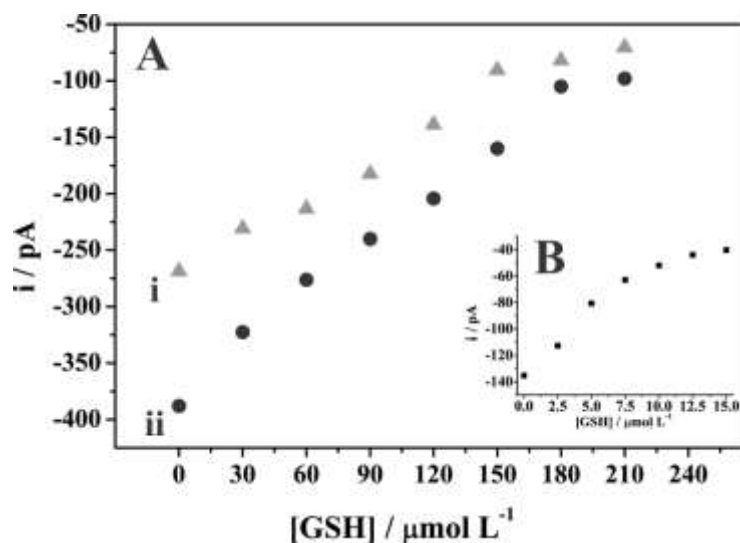


Figure 3.5. (A) Collection current recorded at the ring as a function of GSH concentration for two different tip-substrate separation values: (i) 30 and (ii) 5 μm . $E_{disc} = 0.9$ V, $E_{ring} = -0.2$ V. (B) Collection current recorded at the disc vs. GSH concentration in experiments performed with the tip far from the substrate. $E_{disc} = -0.2$ V, $E_{ring} = 0.9$ V. Experiments performed in a 1 mmol L⁻¹ APAP + 10 mmol L⁻¹ PBS solution (pH 7.4).

The ability to change the collection efficiency by changing the tip-substrate separation makes the system flexible regarding its sensitivity towards GSH detection and allows for such parameter to be chosen according to the experimental condition. Although a higher sensitivity is always desired, the positioning of the tip too close to the substrate could represent a higher risk of crashing the tip in a SECM DG/RC experiments, thus a larger tip-substrate separation could be beneficial. Another effect of

changing the collection efficiency is changing the detection range of the system. By inspection of Figure 3.5A, one can see that the collection current for curve i (tip-substrate separation = 30 μm) reaches a constant value at a GSH concentration around 150 $\mu\text{mol L}^{-1}$, no significant current changes being noticed after successive GSH additions. In contrast, when the tip-substrate separation is reduced to 5 μm (Figure 3.5A, curve ii) the same effect can only be seen at a concentration of 180 $\mu\text{mol L}^{-1}$. At those concentrations, the collection efficiency for each of the configurations (30 and 5 μm) becomes so low that only a small fraction of the electrogenerated NAPQI reaches the ring. At such small NAPQI levels, the faradaic current is not significantly distinguishable from the background current and cannot be accurately resolved.

Although the ability to change the collection efficiency, as well as the sensitivity of the method, might be desirable for some experimental setups, one should keep in mind the trade between sensitivity and the linear concentration range. In extreme situations, with low collection efficiency, the linear concentration range greatly decreases. In order to simulate such adverse scenario, the generator and collector electrodes were inverted (ring = generator, disc = collector) and, consequently, much lower collection efficiency values are achieved (Figure 3.5B). The low collection efficiency of this setup resulted in a linear concentration range one order of magnitude smaller when compared to the conventional setup (DG/RC). It should be pointed out that similar results could be obtained with the conventional configuration (DG/RC) but working with acetaminophen in much lower concentrations.

3.4.3 Space resolved detection

Space resolved information can be obtained through the use of a SECM setup which is especially interesting when working with biological systems where local changes in composition are of high interest. This is even more important when working with single entities, such as single cells ¹². SECM experiments generally require a redox mediator present in solution in order to determine the tip-substrate separation. This is typically done by recording an approach curve, where current at the tip is measured as a function of its separation from the substrate. As the solution already contains APAP, which can be easily oxidized at diffusion-limiting conditions at the disc, this substance was used as a redox mediator. Even though NAPQI reacts with GSH to generate APAP in an electrocatalytic cycle, the high mass transport rate at microelectrodes limits this effect on the disc current and allows for the electrode to be approached even in the presence of GSH, with no change in the disc current/separation dependence, as can be seen in Figure 3.6. Furthermore, as the disc current is independent of GSH concentration, in opposition to what was noticed for the collection current at the ring (Figure 3.5), the system produces an electrochemical response (normalized collection efficiency) that is independent of the topography, as will be explored further in the manuscript. This feature could allow for a constant distance SECM experiment to be performed, similar to previously reported in the literature ²², although a more specific instrumentation is needed. In this work a simpler alternative was used that, despite not being a constant distance scan, still give information independent of the topography.

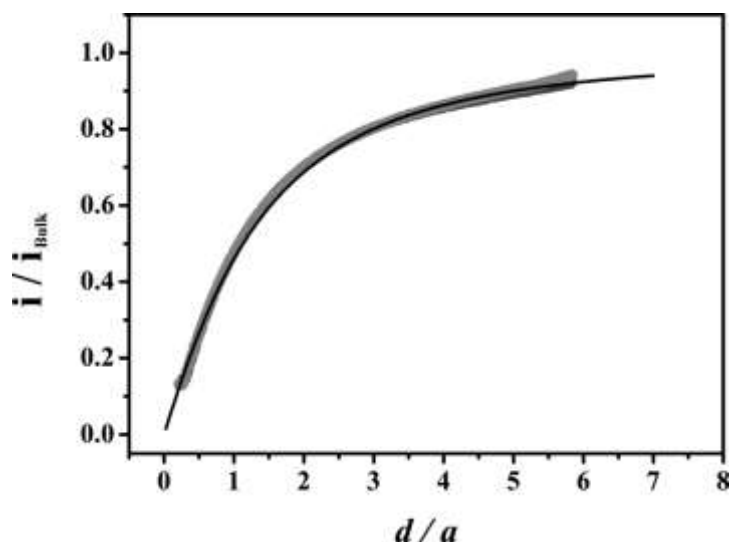


Figure 3.6. Normalized approach curve recorded in 1 mmol L^{-1} APAP + 10 mmol L^{-1} PBS solution. Dots: In presence of GSH 50 mmol L^{-1} and absence of GSH. Both data are superimposed. Black line: Theoretical curve. $E_{disc} = 0.9 \text{ V}$. Radius of the microelectrode, $a = 12.5 \mu\text{m}$.

Aiming to demonstrate the applicability of the proposed method for space-resolved GSH detection, a SECM DG/RC experiment was performed in a “mock up” system as a proof of concept. A special electrochemical cell containing two stacked compartments (one above the other) and separated by an impermeable membrane in such a way that they can be filled with distinct solutions was used. A schematic drawing of the cell can be found in Figure 3.7A. The bottom compartment is connected to a secondary reservoir that is open to atmospheric pressure in order to maintain hydrostatic condition with the top compartment. The top compartment was filled with 1 mmol L^{-1} APAP in 10 mmol L^{-1} PBS solution (pH 7.4), while the bottom one received the same solution, but also containing $100 \mu\text{mol L}^{-1}$ GSH. The separating membrane was punctured using a sharp object in order to produce a small opening from where GSH can diffuse to the top compartment, simulating a localized GSH transport/release system.

With the disc polarized at 0.9 V, where APAP is oxidized at diffusion-limited conditions, and the ring polarized at -0.2 V in order to collect the electrogenerated NAPQI, the electrode was approached to the membrane and kept at a constant height of 5 μm . A small opening close to the center of the membrane was made using a quartz micropipette and the electrode was scanned along the xy plan (parallel to the membrane) in a SECM DG/RC experiment. Figure 3.7B shows the obtained electrochemical image regarding the GSH diffusion across the punctured membrane and the current decrease noticed when the electrode was scanned across the orifice indicates the permeation of GSH and consequent consumption of NAPQI generated at the disc, hence less material reached the ring.

Although the feature of the image can be correlated to the transport of GSH across the puncture, one can argue that the current response might have a topographical contribution as it can be difficult to separate the electrochemical response from the topographical one in a constant height SECM experiment. As the sensing of GSH relies on changes of the collection efficiency and such parameter is affected not only by the GSH concentration, but also by the tip-substrate separation (topography), a procedure was used to compensate possible topography influence of the membrane. Accordingly, the collection efficiency was normalized by using current measurements obtained in an experiment prior to puncturing the membrane (no GSH transport). The normalization, as seen on Figure 3.7C, shows an area with decreased collection efficiency, characteristic of an active site on G/C SECM experiments⁴⁴. The decrease is expected as GSH will react with the electrogenerated NAPQI throughout its transport to the ring electrode. The reduced collection efficiency area correlates with the reduction on the collection current seen on Figure 3.7B, hence the distinct feature on both images can be regarded as due to the GSH transport and not to a topographical artefact.

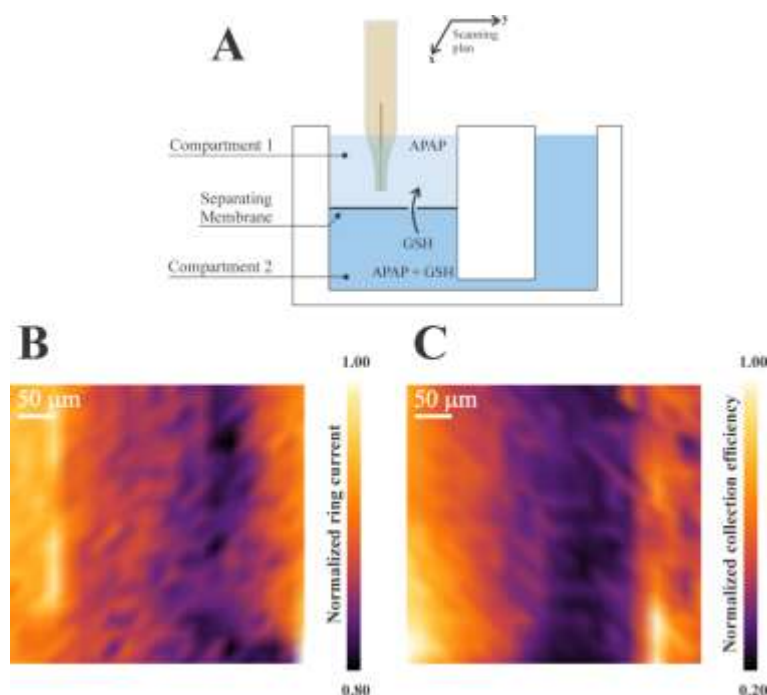


Figure 3.7: (A) Schematic drawing of the electrochemical cell used during the electrochemical imaging experiments showing the separated compartments and the separating membrane. Electrochemical image of GSH transport across an orifice in the separating membrane showing normalized ring current (B) and normalized collection efficiency (C); $E_{disc} = 0.9\text{ V}$, $E_{ring} = -0.2\text{ V}$.

The information provided by Figure 7C, despite being free from topography influences, does not give any quantitative value for GSH concentration, at least not directly, for such a constant distance SECM mode such as a Shear Force-SECM⁵⁹ or Scanning Ion Conductance Microscopy/SECM¹⁶ would be more suitable. Even if such information cannot be obtained directly, as both images present a high degree of correlation one can assume that the features presented in Figure 7B are mostly independent of any topographic features on the substrate allowing for a comparison between the decrease in current on the image with the one obtained in Figure 3.5A, curve ii. The 20% decrease in ring current, as seen in Figure 3.7B, is expected as the concentration of GSH in compartment 1 (Figure 3.7A) is $100\ \mu\text{mol L}^{-1}$. The quartz micropipette used to puncture the membrane had to be approached in angle in order to

clear the electrode and electrode holding system of the SECM equipment, thus resulting in a puncture that resembles more a cross cut than a hole, hence the oddly elongated feature seen in Figure 3.7.

3.5 Conclusions

In this paper we were able to demonstrate, as a proof of concept, the possibility of using ring-disc microelectrodes to monitor the concentration of glutathione by an indirect method using acetaminophen as an electroactive probe. The fabrication of the ring-disc microelectrode was found to be straightforward, allowing batch processing. Changes in the tip-substrate separation allowed the linear concentration range and sensitivity of the method to be modulated, enabling to resolve glutathione concentration in buffer solution at $\mu\text{mol L}^{-1}$ levels. The possibility of acquiring space-resolved information was investigated and the system was found to be able to electrochemically image GSH diffusion across an orifice in an impermeable membrane in a SECM DG/RC experiment. Although further investigation is needed, we envisage that the method could be used in more complex systems both for electrochemical detection and imaging.

3.6 Acknowledgements

The research upon which this article was based was supported by Conselho Nacional de Desenvolvimento Científico e Tecnológico (CNPq: grant number 48383/2012-2) and FAPESP (Fundação de Amparo à Pesquisa do Estado de São Paulo), to which the authors are very grateful for the financial support.

Chapter 4. Controlled Fabrication and Characterization of Multifunctional SEMC-SICM Carbon Nanoprobes for Electrochemical Microscopy

Pipette based carbon electrodes are an attractive alternative for fabricating electrochemical probes for SEPM. Such probes rely on the use of nanopipettes that can be easily pulled to sharp tapers resulting in pipette openings of a few 10s of nanometers at which the deposition of conductive carbon (usually by pyrolysis) can be performed to form a nanometer sized electrodic surface. Although carbon (especially pyrolytic) does not present pristine electrochemical properties, the easy and speed of the fabrication procedure (pulling pipette and carbon pyrolysis) yields quick and small electrodic surfaces that would be otherwise complicated to achieve using classic fabrication methods relying on metal fibers. Despite simple and promising, the fabrication procedure employed hereinto results in low reproducibility of the carbon electrodic surface, which usually turned quite ways recessed on the pipette body. This recessed electrodic surface is (usually) non-ideal for SEPM experiments and can greatly compromise the interpretation of results.

This chapter will be submitted as a technical note to *Analytical Chemistry* and describes the development of a new fabrication procedure, based on the use of a well-controlled gas flow (for the carbon source) and heating procedure (for pyrolysis), which is capable of producing non-recessed electrodic surfaces. The new fabrication method retains the simplicity and speed of the previous method employed, but greatly increases the reproducibility and the yield of electrodes with ideal geometry. The method was used for fabricating multifunctional electrochemical probes (SECM-SICM) with

nanometer dimensions which were used for imaging a microelectrode surface (2 μm radius) with nanometer resolution.

Controlled Fabrication and Characterization of Carbon Nanoprobes for Electrochemical Microscopy

*Gabriel N. Meloni[†], Minkyung Kang[†], Robert A Lazenby[†], Emma Ravenhill and Patrick R. Unwin**

Department of Chemistry, University of Warwick, Coventry, U.K., CV4 7AL.

[†] These authors have contributed equally to this work

*Corresponding Author

4.1 Abstract

A combined scanning electrochemical microscopy/scanning ion conductance microscopy (SECM-SICM) probe fabrication method, using a dual barrel capillary, based on butane pyrolysis, is described. Such probes are becoming widely used for electrochemical microscopy applications, and are frequently made using a flame blow torch method that does not offer adequate control of the carbon deposition process. Here, we have modified an electric coil capillary puller to gain significantly greater control over the carbon deposition (pyrolysis) process, allowing the tuning of parameters (deposition time, coil position, and coil temperature), in order to produce non-recessed (as well as recessed, if required) carbon probes. Probes were characterized after different conditions for the pyrolysis process, using various techniques such as transmission electron microscopy (TEM), Raman spectroscopy, and cyclic voltammetry (CV). We demonstrate the effect of the parameters associated with the pyrolysis process, hence the need for the greater control that the heated coil puller method provides, over the flame blow torch method.

4.2 Introduction

Scanning electrochemical microscopy (SECM)^{7,8} has been used extensively to explore electrochemical activity and probe kinetics at surfaces. The combination of

SECM with techniques for distance feedback, such as atomic force microscopy (AFM)^{61,128} or scanning ion conductance microscopy (SICM),^{16,21} allows for improved image resolution and simultaneous topographic mapping.^{14,129} In recent studies, SECM-SICM has proven powerful for high resolution topographical and electrochemical mapping of biological cells and nanomaterials,^{7,8,85} and local ion flux measurements.^{9,16–18} Nanoscale dual-function probes for this technique can be fabricated from a single barrel glass pipet, coated with thin metal layer deposit and further insulated, to form a ring electrode surrounding the pipet opening.^{18,20,21} A more popular method is to use a double barrel quartz pipet, with one barrel filled with a carbon deposit, produced by the pyrolysis of a carbon-containing gas such, as butane.¹⁶ The open channel, in either of these fabrication methods, is filled with electrolyte and a Counter reference electrode to function as the SICM probe, and the metal or carbon deposited electrode is used for SECM.

Dual barrel SECM-SICM probes with pyrolyzed carbon have been widely adopted in recent studies, because they can be fabricated relatively quickly and easily. The carbon probe can be decorated with other materials,^{44,130,131} and applied to electrochemical sensing and imaging in biological environments,^{16,17} pH measurements,⁶⁸ and hydrogen peroxide detection,⁸⁵ amongst others.¹³² The fabrication method introduced by Takahashi *et al.*¹⁶ stands out due to its simplicity and the possibility of the fast production of probes. Here, a constant butane gas flow passes through one barrel of the dual barrel quartz capillary and carbon is pyrolytically deposited under an argon atmosphere by heating the capillary with the flame of a blow torch. This method can yield nanometer-sized probes, which can be easily functionalized to produce a solid metal nanoelectrode without the time-consuming procedures reported previously.^{24,133} To gain further control of the pyrolysis process, an

electric coil capillary puller¹³⁴ and chemical vapor deposition (CVD) methods¹³⁵ have been used for carbon deposition in quartz pipets, although the latter appears more complicated and time-consuming compared with the flame method. It should also be mentioned that focused ion beam-scanning electron microscopy (FIB-SEM) has also been used to mill the ends of nanoelectrodes after the carbon deposition to shape probes and eliminate electrode recession.⁵⁷

The dimensions of SECM-SICM probes are generally characterized by scanning electron microscopy (SEM),^{8,17,51} however the resolution of SEM and charging effects on the nonconductive part of the pipet limits the accuracy for probe characterization. Moreover, the precise geometry, including the recession depth of the carbon plug and even the quality of fill of the carbon within the pipet, are not easily obtained. Higher resolution images of pipet probes, can be obtained by the use of transmission electron microscopy (TEM),¹³⁵⁻¹³⁷ as originally proposed by Baker's group. The thin glass wall around the end of the pipet (less than tens of nanometers thick) allows TEM techniques to not only image the outer contour of the nanopipet but also observe through the pipet wall. Scanning (S)TEM is also applicable to image the side-view of nanopipets¹³⁶ and characterize the opening size, but can result in tip degradation due to the highly focused electron beam required.¹³⁵ Furthermore, Raman spectroscopy^{7,57} provides a measure of the quality of pyrolyzed carbon by comparing the intensity ratio of the known D and G peaks¹³⁸ and AFM⁶⁷ can be used to show the roughness of the carbon surface in the pipet from the top.

Herein, we present an improved carbon SECM-SICM probe fabrication method retaining the simplicity of the butane pyrolysis approach, but offering improved control over the carbon filled barrel. The SICM-SECM probes were assessed by TEM, voltammetry and high-resolution electrochemical imaging.

4.3 Materials and methods

4.3.1 Chemicals

All the solid reagents were of analytical grade and were used without further purification. Ruthenium hexamine chloride and potassium chloride (“ACS reagent” grade) were obtained from Sigma-Aldrich (St. Louis, MO, USA). All solutions were prepared with ultra-pure water (“Select HP”, Purite, >18 M Ω cm at 25 °C).

4.3.2 Fabrication of SECM-SICM probes

SECM-SICM tips were fabricated in a two-step process. First, a quartz theta pipet (o.d. 1.2 mm, i.d. 0.9 mm) was pulled using a laser puller (P-2000, Sutter Instruments) to a sharp point with an approximate diameter that ranged from 250 to 400 nm. Note that although smaller (or larger) tip sizes could be pulled and filled with carbon, we focused on this size range as typically for combined SECM-SICM, in order to fully investigate the carbon pyrolysis parameters. Changing the size of the pipet tip would require readjustment of those parameters, but the procedures herein provide a basis for this if required. One of the pipet barrels was blocked with ‘Blu-Tack’ (Bostik) and a constant butane flow, between 0.6 – 0.8 bar of pressure, was passed through the other barrel. A modified electric coil capillary puller (PB-7, Narishige) was used as the heat source for the butane pyrolysis. With the tip under an argon flow (0.1 L min⁻¹) and the heating coil set to a desired temperature, a servomotor was used to move the coil through the length of the tip to pyrolytically deposit carbon from the butane, as illustrated in Figure 4.1. The pyrolysis temperature (T_p), was monitored by a microcontroller board (Arduino Uno, Arduino) that recorded the temperature of the coil using a type-K thermocouple, and the pyrolysis time (t_p) was controlled by the translation speed of the servomotor.

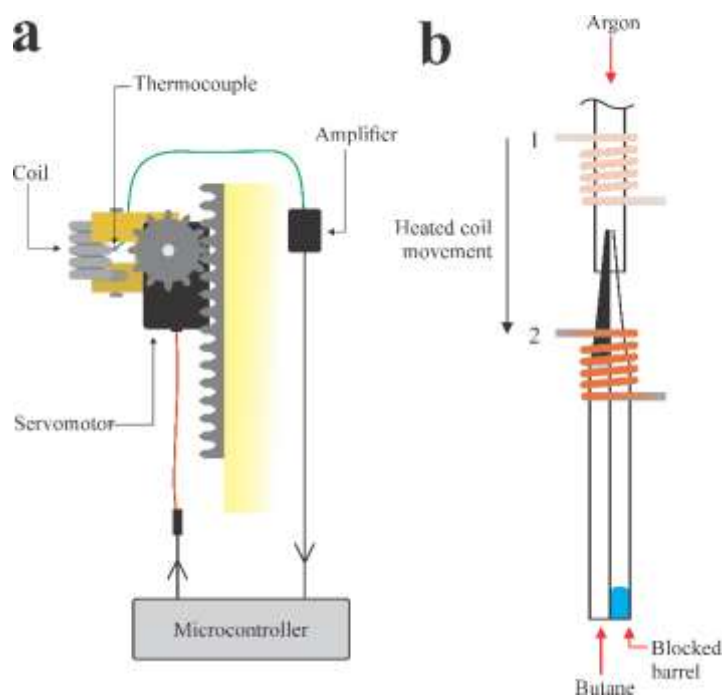


Figure 4.1. Schematic of the setup used to fabricate pyrolytically deposited carbon electrodes showing: (a) side view representation of the coil carriage assembly (heating coil, servomotor and thermocouple sensor) and (b) coil movement through the pipet (from position 1 to 2), showing argon and butane gas inlets and a carbon plug deposited in one barrel only.

4.3.3 Characterization of the SECM-SICM probes

The fabricated tips were characterized using electrochemical techniques, TEM and micro-Raman spectroscopy. Electrochemically, the probes were characterized by recording cyclic voltammograms (CVs) in an aqueous solution of 2 mM ruthenium hexamine chloride, with 0.1 M KCl, this solution was also used for imaging. The potential of the carbon electrode was scanned between 0.1 and -0.5 V at 100 mV s^{-1} , in a 2-electrode arrangement using an AgCl-coated Ag wire quasi-reference counter electrode (QRCE), and the resulting voltammogram was used to estimate the tip radius and the standard rate constant for electron transfer. TEM images were used to assess the geometry, carbon layer recession and SICM barrel contamination, and were performed on a microscope (JEM-2000FX, JEOL), operating at 200 kV accelerating voltage and

equipped with a GATAN ORIUS 11 megapixel digital camera. Micro-Raman spectroscopy (Argon 633 nm laser, 50× lens, NA 0.85, inVia Raman Microscope, Renishaw) was used to assess the quality of the deposit carbon.

4.3.4 SECM-SICM instrumentation and imaging technique

For all electrochemical measurements, including electrochemical imaging, a home-built bipotentiostat was used. For imaging, SECM-SICM probes were mounted to a single axis (z) piezoelectric positioner (P-753-3CD, Physik Instrumente). The piezo/probe assembly was attached to a 3 axis micrometer stage (461-XYZ-M, Newport), allowing for coarse positioning of the tip. A lock-in amplifier (SR830, Stanford Research Systems) was used to induce a controlled sinusoidal oscillation on the tip. The substrate, a 2 μm diameter Pt ultramicroelectrode (UME), was held in a custom-made sample holder that was mounted on an x - y piezoelectric positioner (P-733.2DD High-Dynamics, Physik Instrumente), allowing for lateral movement (imaging).

The fabricated probes were used to electrochemically image the activity and topography of a Pt UME in a substrate generation/tip collection (SG/TC) mode, using a hopping scan protocol that has been described elsewhere.²¹ Briefly, the response of a QRCE placed inside the SICM barrel, filled with electrolyte solution, was used as a probe for distance modulation. A bias potential applied between the QRCE inside the tip and one in the bulk of the solution generated a direct ionic current (DC), and an associated alternating current (AC) due to probe oscillation. The sensitivity of the AC magnitude to the probe to substrate distance was used as a feedback signal for distance control, as in conventional distance-modulation SICM.⁸⁶ In hopping mode, a series of approach curves, at every x - y position in the image plane, were made, with the closest distance based on the AC set point (estimated to be 200 nm). The data collected

produced both an electrochemical and a topographical image. With the substrate UME potential set to reduce $\text{Ru}(\text{NH}_3)_6^{3+}$ to $\text{Ru}(\text{NH}_3)_6^{2+}$ (-0.3 V) and the SECM carbon barrel potential set to oxidize $\text{Ru}(\text{NH}_3)_6^{2+}$ to $\text{Ru}(\text{NH}_3)_6^{3+}$ (0.3 V), the tip was successively approached to the substrate x - y position and the resulting SECM current and tip displacement along the z -axis were used to form the electrochemical and topographical image pixel by pixel.

4.4 Results and Discussion

4.4.1 SECM-SICM probe fabrication

We first considered the SECM-SICM probe fabrication method of Takahashi *et al.*,¹⁶ as this method has been widely adopted in this field.^{7,8,44,53,68,131} Although a very popular method, our investigation suggests that control of the amount of recession of the carbon layer is extremely challenging. In addition, it is difficult to control the pyrolysis temperature, which can lead to melting and softening of the quartz glass, resulting in misshapen tips, reduced in tip diameter (Figure 4.2a), or in extreme cases closed entirely (Figure 4.2b). Recession of the carbon layer is a further problem, high temperatures can lead to carbon oxidation, even with the butane pyrolysis occurring under an argon atmosphere. This increases the amount of carbon layer recession that can range from half a micron to several microns into the barrel (Figure 4.2c).

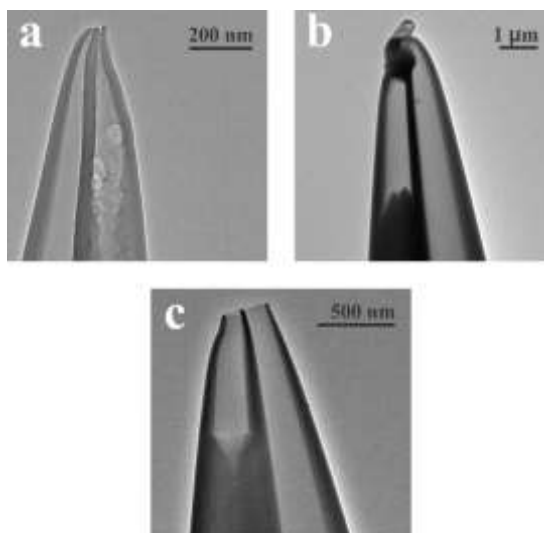


Figure 4.2. TEM images to show common problems faced when using poor control of the heat source. (a) Misshapen tip geometry and reduced tip diameter as a consequence of partial melting of the pipet quartz body. (b) Blocked tip due to complete melting of the pipet quartz body. (c) Carbon layer recession in the order of micrometers.

As we show herein, the heated coil method offers enhanced control that is required to produce probes reproducibly, although the variables first require optimization depending on the dimensions of the probe used. For this study, we chose to focus on probes of 250 to 400 nm in diameter, which are a useful size for SECM-SICM, in order to fully optimize the parameters used in the heated coil method, these were the carbon deposition time, temperature, coil position and gas pressure.

Figure 4.3 shows TEM images of SECM-SICM probes made using the heated coil method, to demonstrate the effect of deposition time and temperature. It can be seen in Figure 4.3a, that a short deposition time (250 s) and/or lower deposition temperature (750 °C) generates a tip with carbon deposition on the inside walls, but a hollow core. By increasing one or both of those parameters, a perfect flush and filled tip that keeps the original pipet geometry is obtained, as shown in Figure 4.4b (for $T_p = 800$ °C and $t_p = 200$ s). If the parameters, T_p and t_p , are further increased, the carbon layer starts to recess inside the fabricated tips, as was the case for the tip in Figure 4.3c ($T_p = 800$ °C,

$t_p = 300$ s). This is most likely due to carbon oxidation at the pipet barrel, as was pointed out for the tip produced by the blow torch flame method in Figure 4.2c.

As discussed, there is a fine balance between temperature and time in order to fabricate fully filled carbon tips, which is extremely hard to achieve by the flame deposition method,¹⁶ which lacks precise control of these parameters. As Figure 4.3 shows, a difference of 50 °C in the coil temperature is enough to produce a hollow tip rather than a fully filled one, whilst a difference of 100 s in deposition time separates a fully filled tip from a recessed one.

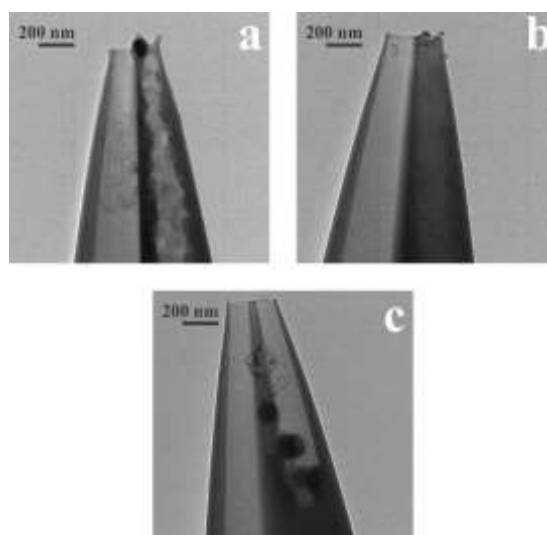


Figure 4.3. TEM images to effect of temperature and deposition time on carbon pyrolysis. (a) Hollow profile ($T_p = 750$ °C, $t_p = 250$ s). (b) Completely filled carbon barrel and an unblocked SICM barrel ($T_p = 800$ °C, $t_p = 200$ s). (c) Recession cavity caused by carbon oxidation due to high pyrolysis temperature and time ($T_p = 800$ °C, $t_p = 300$ s).

The quality of the pyrolytically deposited carbon at different T_p was assessed by Raman spectroscopy, with an excitation wavelength of 633 nm. Analysis was accomplished by monitoring the characteristic D and G peaks (1340 and 1595 cm^{-1} , respectively) of graphitic material using the intensity ratio ($R = I_D/I_G$) of two peaks,

which represents the disorder or structure defects in carbon materials.¹³⁸ R values (from Figure 4.4b and d) for the lower T_p and the higher T_p were 1.1 and 0.9, respectively. This implies the T_p has only a marginal effect on the quality (in terms of disorder and defects) of the carbon deposit. More importantly, the TEM images show that T_p has a significant effect on the growth of the carbon in the tip, with a higher T_p resulting in a much greater recession of the carbon deposit.^{139,140}

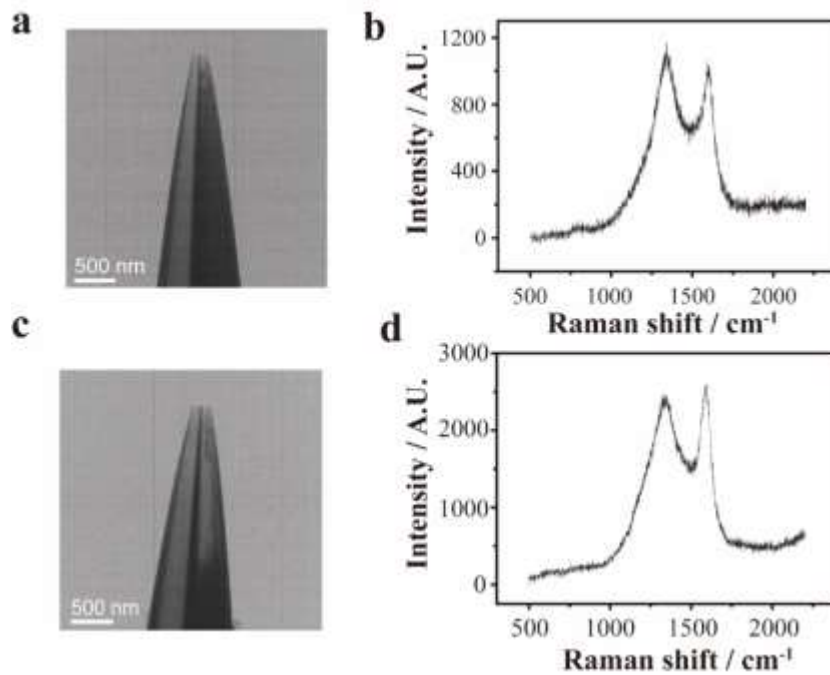


Figure 4.4. TEM image (a) and Raman spectrum (b) of the SECM-SICM probe made using a lower T_p . TEM image (c) and Raman spectrum (d) of the SECM-SICM probe made using a higher T_p .

The use of an electronic controller based on a microcontroller and an electric heating coil made it possible to tune those parameters in such a way that 80% ($n = 23$) of the fabricated tips presented no obvious recession and 100% presented less than 500 nm of carbon layer recession as shown in the histogram in Figure 4.5. This method therefore eliminates the need for using FIB milling to cut the tips flush.^{57,72} FIB milling is not only a time-consuming and not widely available technique, but also can induce

structural damage on carbon material as demonstrated by Baker *et al.*⁵⁷ Even under minimal exposure to the ion beam, FIB can introduce contamination to the electrode material by Gallium ions impregnation jeopardizing the electron transfer kinetics.¹⁴¹ The electronic controller, whereas, makes it possible to set different deposition times and temperatures for carbon deposition at the tip ends and the control the recession of the SECM tip. The change of R value at different T_p in Raman spectra, is insignificant, implying marginal damage of carbon for electrochemical activity¹⁴⁰ and lead us to further application of recessed tip modified with nanoparticles using electrochemical deposition for wider application of the SICM-SECM tip.

Moreover, recessed tips can still show good electrochemical behavior in cyclic voltammetry (sigmoidal shape with no hysteresis)^{135,142} that could appear as a result of completely filled tips. This naive assumption makes it challenging to accurately use those tips for quantitative measurements when the precise geometry and size of the tip must be known, a particular problem when fitting theoretical and experimental data.

It is important to note that we have found no evidence of tip damage that could be caused by electrostatic discharge (ESD), in either the high-resolution TEM images or in the electrochemical measurements for any of the tips herein. Nanometre-size metal electrodes are known for being susceptible to ESD damage,¹⁴³ and lately ESD damage on carbon nanoelectrodes has been reported.¹⁴¹ As ESD can be reduced (if not avoided) by a high humidity environment,¹⁴³ we can speculate that the lack of ESD damage is justified by high local humidity in the UK (typically 76%-89%) .

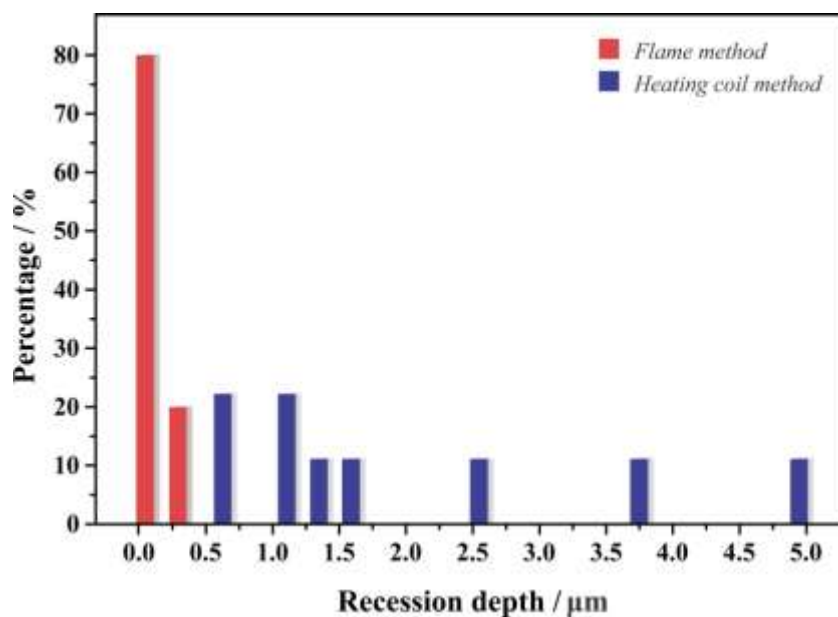


Figure 4.5. Histogram showing the distribution of carbon layer recession of carbon nanoprobes fabricated by two methods: the manual blow torch method (■), as described by Takahashi et al., and the “heating coil method” (■) as described in this manuscript.

4.4.2 Electrochemical characterization and imaging

Although the dimensions of the carbon surface can be reasonably characterized by measurements using SEM and TEM images, more commonly the steady-state limiting current is used for this purpose. Assuming a planar disk geometry for a non-recessed electrode, and using the steady-state limiting current equation corrected for electrodes with small insulating walls,³⁶ the electrode radius calculated from the reduction current of 2 mM ruthenium hexamine chloride (0.1 M KCl) (Figure 4.6b) was 83 nm. Note that the ratio of the radius of the insulating glass sheath to radius of the active carbon electrode, known as the RG value, used was 1.1. Using the simple analysis of steady-state voltammograms presented by Bard and Mirkin,⁷¹ the standard rate constant (k^0) calculated was 1.69 cm s^{-1} , a great improvement on the values previously reported for electrodes fabricated by the blow torch method.¹⁶ This value was further confirmed by fitting the experimental data to theoretical models using the

DigiElch software (Gamry, USA). The resulting fitting can be seen in figure 4.7. The SICM voltammogram (Figure 4.6a) shows that carbon was selectively deposited in just one of the theta pipet barrels, leaving an unblocked barrel that could be used as a SICM electrode.

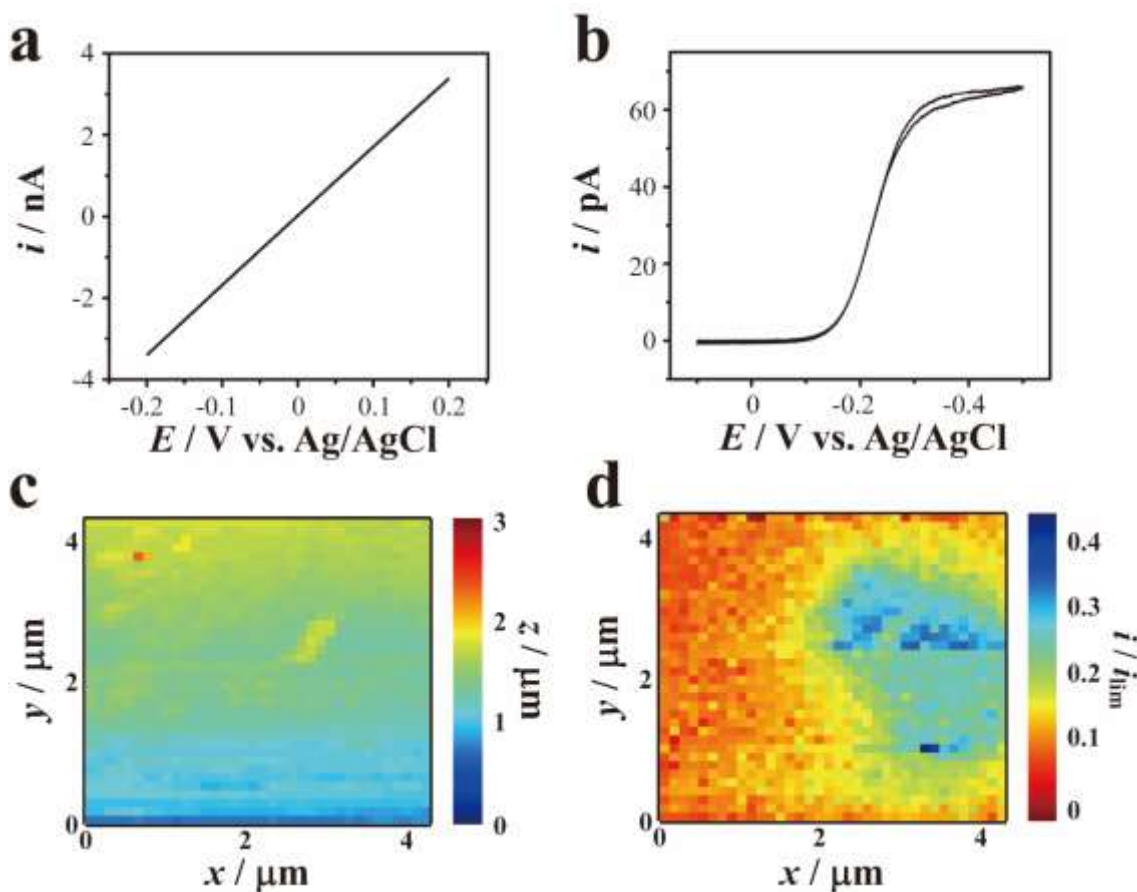


Figure 4.6. Electrochemical characterization of the fabricated probes in 2 mM ruthenium hexamine chloride, 0.1 M KCl solution. (a) Cyclic voltammogram performed on the SICM barrel, at 100 mV s^{-1} scan rate. (b) Cyclic voltammogram performed on the carbon filed barrel, at 100 mV s^{-1} scan rate. (c) Topographic image (SICM) and (d) electrochemical (SECM) image of Pt UME ($d = \sim 2 \mu\text{m}$). Pixel size = $100 \times 100 \text{ nm}$.

As a proof of concept of the high-resolution capabilities of those tips, a platinum UME ($\sim 2 \mu\text{m}$ radius, Figure 4.8) was used as a substrate in a SG/TC setup. The tip was approached to the UME using the AC component of the ionic current as a distance feedback signal. The electrochemical image was performed in hopping mode, as

explained previously. The resulting topography profile of the UME and electrochemical current (SECM barrel) can be seen in Figure 4.6c and 4.6e, respectively. The tip was able to track the UME topography without crashing into the surface, whilst recording the electrochemical response. The small dimensions of the fabricated tip allowed a high-resolution image of the UME to be obtained, which had a slightly elliptical shape that matched observations by optical microscopy.

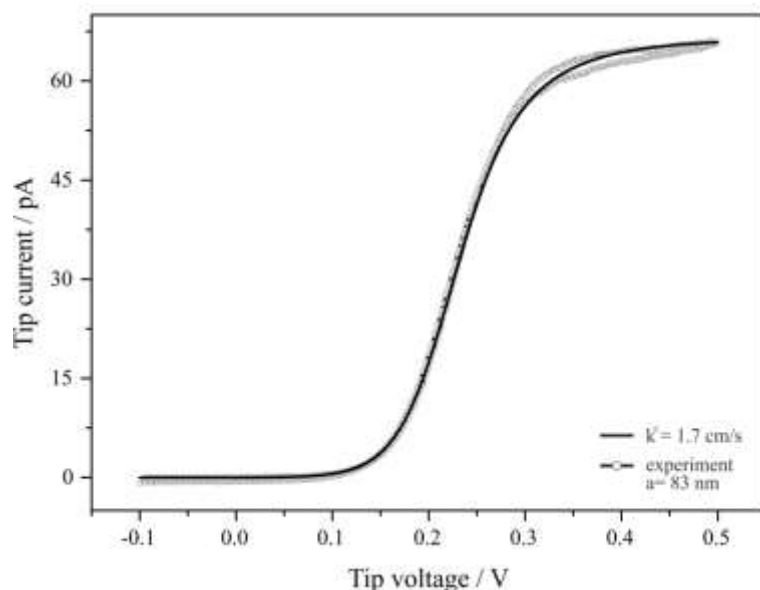


Figure 4.7. (Dots) Voltammogram performed on the Carbon filled barrel, at 100 mV s^{-1} scan rate. (Solid line) Simulation using the DigiElch software for an 83 nm radius electrode and a standard rate constant (k^0) of 1.7 cm s^{-1} . 2 mM ruthenium hexamine chloride, 0.1 M KCl solution

One can clearly see a good fit between the experimental data and the theoretical simulation (for the SECM voltammograms) in Figure 4.7 for a standard rate constant (k^0) of 1.7 cm s^{-1} , which is in good agreement with the number calculated previously by numerical methods.

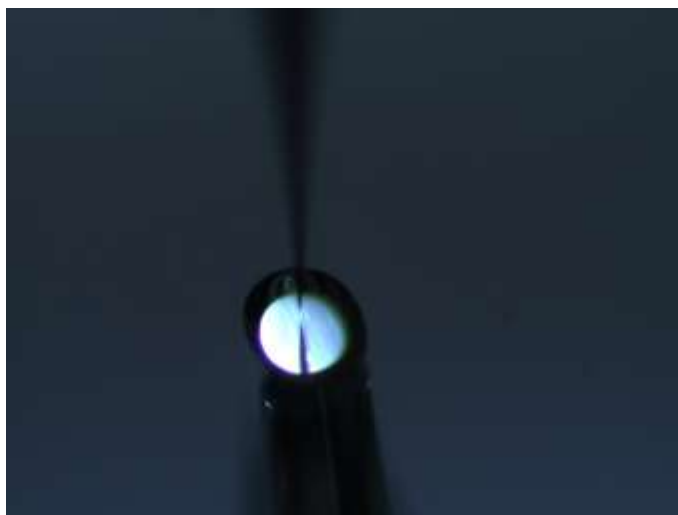


Figure 4.8. Optical image of a Multifunctional SECM-SICM electrochemical probe approaching a 2 μm radius platinum microelectrode substrate for the experiments portrayed in Figure 4.6.

4.5 Conclusions

We have presented a modified method for the fabrication of carbon nanoelectrodes, based on an established method of pyrolysis of butane in quartz pipets. The key advantage of the method is the much improved control of the fabrication parameters, by using a coil wire adjustable heat source and microcontroller. This meant the fabrication of non-recessed carbon tips was possible, with a high reproducibility rate. We demonstrated some of the common problems encountered when using the more established methods, such as tip melting and carbon oxidation, that have been overcome by the new approach. The fabricated tips can be readily used without the need of subsequent methods to improve tip quality, such as FIB milling, providing a much quicker and cheaper alternative for fabricating high-quality carbon electrodes.

The fabricated SECM-SICM probes were used to obtain a high-resolution electrochemical image of a 2 μm radius platinum UME, proving their capabilities for resolving, with high spatial resolution, small features. The probes were well

characterized, in particular by using TEM imaging to examine the pyrolyzed carbon deposit and glass geometry. This proved useful to illustrate the potential problems that could occur with the established flame torch method, as well as to assist in fine-tuning the parameters in our modified set up. We plan to publish further work on the characterization of nanopipettes used in SECM and SICM experiments in due course, as an understanding of the probe geometry and composition is crucial in gaining a full understanding of a system of interest, especially at the nanoscale.

4.6 Acknowledgements

This work was supported by Conselho Nacional de Desenvolvimento Científico e Tecnológico (CNPq: grant number 203506/2014-6) providing a studentship for G.N.M. and a University of Warwick Chancellor's International Scholarship to M.K. We thank Dr. Alexander W. Colburn and Mr. Rod Wesson for designing and building electronic instrumentation used in this work. The authors would also like to thank Binoy P. Nadappuram for initial work on this system.

Chapter 5. Multifunctional electrochemical probe at a single barrel nanopipette

As mentioned on Chapter 1, Section 1.3.3, multifunctional electrochemical probes can assume a variety of shapes and designs and not always present more than one electrodic surface for acquiring multiple electrochemical information. In Chapter 3 and 4 we explored the fabrication and application of multifunctional probes that have a somehow more obvious design and shape, presenting more than one electrodic surface. Although some applications do require more than one electrodic surface, as for most hybrid techniques, this is not true for others and a multifunctional probe can have only one electrodic surface. In this Chapter, the application of a single barrel nanopipette as a multifunctional electrochemical probe for SICM experiments will be explored.

Although SICM is a (mostly) unselective technique and largely employed for topographical mapping (Section 1.3.2), it can be used to “track” chemical reactions and active sites (were the reaction is happening) by mapping spatial distribution of ionic flow (local conductance). This is possible as for any reaction taking place at an interface, charge neutrality is conserved despite the consumption or formation of charged species during the reaction. This charge neutrality is achieved by contra balancing the charged species consumed or produced with other charged species in solution, usually from the supporting electrolyte. Although the charge is balanced, the different species will have different mobilities and hence, will affect the local conductivity. By exploring this phenomenon, it was possible to monitor topography and chemical reactions employing a single barrel pipette as a SICM probe.

This chapter was published in *Analytical Chemistry* and resulted from the one year spent as a visiting student at the Warwick Interfaces and Electrochemictry Group

(WEIG) at the University of Warwick, under the supervision of Prof. Patrick R. Unwin. This chapter was elaborated in collaboration with Dmitry Momotenko, Kim McKelvey, Minkyung Kang and Patrick Unwin, which are in accordance with the use of the paper as a chapter. The research, which was idealized by Dr. Momotenko, was only possible due to this collaboration and much of the results herein presented were not obtained, analyzed and published solely by myself, and I cannot, and will not, take credit for the entire paper. Credit should be given to all the authors, especially to Dr. Momotenko for idealizing the project and for performing all the mathematical modeling.

Simultaneous Interfacial Reactivity and Topography Mapping with Scanning Ion Conductance Microscopy

*Dmitry Momotenko**, *Kim McKelvey*, *Minkyung Kang*, *Gabriel N. Meloni* and *Patrick R. Unwin**.

Department of Chemistry, University of Warwick, Coventry, CV4 7AL, United Kingdom

*Corresponding author

5.1 Abstract

Scanning ion conductance microscopy (SICM) is a powerful technique for imaging the topography of a wide range of materials and interfaces. In this report, we develop the use and scope of SICM, showing how it can be used for mapping spatial distributions of ionic fluxes due to (electro)chemical reactions occurring at interfaces. The basic idea is that there is a change of ion conductance inside a nanopipette probe when it approaches an active site, where the ionic composition is different to that in bulk solution, and this can be sensed via the current flow in the nanopipette with an applied bias. Careful tuning of the tip potential allows the current response to be sensitive to either topography or activity, if desired. Furthermore, the use of a distance modulation SICM scheme allows reasonably faithful probe positioning using the resulting AC response, irrespective of whether there is a reaction at the interface that changes the local ionic composition. Both strategies (distance modulation or tuned bias) open up the prospect of simultaneous topography-activity mapping with a single channel probe. The application of SICM reaction imaging is demonstrated on several examples, including voltammetric mapping of electrocatalytic reactions on electrodes and high-speed electrochemical imaging at rates approaching 4 s per image frame. These two distinct approaches provide movies of electrochemical current as a function of potential with hundreds of frames (images) of surface reactivity, to reveal a wealth of spatially-

resolved information on potential (and time) – dependent electrochemical phenomena. The experimental studies are supported by detailed finite element method modeling that places the technique on a quantitative footing.

5.2 Introduction

Since its invention by Hansma et al.,⁵ scanning ion conductance microscopy (SICM), has developed into a powerful scanning electrochemical probe microscopy (SEPM) for non-contact nanoscale visualization of surface topography, finding application in imaging living cells^{144–148} and cell membranes (down to the single protein level),⁴⁶ and as a complementary technique for accurate probe-to-substrate distance control, when combined with other scanning probe routines.^{16,21,85,149–151} In essence, the operation of SICM is based on the detection of changes of the conductance current, flowing between two quasi-reference counter electrodes (QRCEs), one in a nanopipette filled with electrolyte and one in the bulk solution. The current magnitude is a measure of resistance of the pipette probe and the tip-to-substrate gap. This two-electrode cell arrangement is typically built on relatively straightforward and inexpensive instrumentation. Similar to other electrochemical nanopipette techniques,^{53,152–155} simple probe design, along with high reproducibility and low cost of tip fabrication (nanopipettes are produced by pulling glass or quartz capillaries to a sharp point with a laser puller) and easily tunable probe size (from a few microns in diameter down to a level of a few nanometers). That provides SICM with high resolving power and considerable flexibility of applications.

Although SICM has mainly been concerned with topographical imaging, it is increasingly recognized that the technique has wider scope and applications.^{156–158} SICM is a sensitive tool for the detection of local ion fluxes,⁵¹ but unlike some other

electrochemical methods, does not require the analyte species to be electroactive, since the probe monitors conductivity changes in the confined region between the sample and the pipette opening. Thus, SICM has been used to study individual pores and ion channels in artificial and living cell membranes.^{18,159–162} Measurements of ion flux through the pipette orifice can be also used to explore ion current rectification phenomena^{163,164} at interfaces^{49,165} opening up exciting opportunities to map spatial distributions of surface charge and to probe heterogeneous acid-base equilibria.^{157,158}

In this work, we introduce new functional capabilities of ion conductance microscopy demonstrating its potential for imaging spatially distributed (electro)chemical reactions through the detection of ionic fluxes near active sites. We provide proof-of-concept applications of this technique for dynamic imaging of electrochemical reactions at electrodes, first by recording the ion conductance response to a series of voltammetric sweeps, over wide potential range, with the pipette at a set of coordinates (image pixels) to map out oxidation and reduction reactions occurring at the electrode. Second, we highlight the potential of SICM for high-speed visualization of electroactivity at rates approaching 4 s per image frame.

A strength of the technique described is that it is quantitative, and we provide theoretical support for the experimental observations by comparison of experimental data with finite element modeling. Since all electrochemical reactions are accompanied by changes in local ionic composition (speciation), a fact that is also true for many other interfacial chemical reactions, the studies herein provide a foundation for SICM to become a powerful general probe of local interfacial reactivity.

5.3 Material and methods

5.3.1 Chemicals

Ferrocene methanol (FcCH_2OH , $\geq 97\%$, Sigma-Aldrich), hydrazine sulfate ($\geq 99.0\%$, Sigma-Aldrich) and KNO_3 ($\geq 99.0\%$, Sigma-Aldrich) were used as received. Deionized (DI) water produced by Purite Select HP with resistivity 18.2 M cm ($25\text{ }^\circ\text{C}$) was used to prepare aqueous solutions. Ferrocenylmethyl trimethylammonium hexafluorophosphate (FcTMA^+) was synthesized in house as described elsewhere.¹⁶⁶

5.3.2 Nanopipette probes

Nanopipettes with tip radii of approximately 95 nm and 200 nm were pulled from single-barrel borosilicate glass capillaries containing a filament (GC120F-10, Harvard Apparatus) using a laser pipette puller (P-2000, Sutter Instruments). For geometric characterization, nanopipettes were gold-coated and visualized using a field-emission scanning electron microscope (FE-SEM, Zeiss SUPRA 55 VP). Nanoscale characterization of the geometry of uncoated nanopipette tips was carried out using a transmission electron microscope (TEM) JEOL 2000FX at 200 kV accelerating voltage.

5.3.3 Scanning ion conductance microscopy (SICM) setup

Pipette probes were mounted on a custom made probe holder and coarsely positioned over a sample with a mechanical micropositioner (Newport, M-461-XYZ-M) and the aid of a 3MP digital camera (PixeLink PL-B776U) with 4X magnification lens. The electrolyte solution in the nanopipette probes contained no redox species, while the bulk solution was composed of both supporting electrolyte salt and redox mediator. Precise control and translation of the probe in the vertical direction (normal to the electrode surface of interest) was achieved with a single axis nanopositioner (Physik Instrumente, P-753.3CD). A small vertical oscillation of the probe (40 nm peak-to-

peak) at typical frequencies of 270 – 370 Hz was applied using a lock-in amplifier (Stanford Research Systems, SR830) to induce an alternating current (AC), the magnitude of which served as a positional feedback (distance-modulated SICM).^{167,168} Scanning was accomplished with a high-precision XY nanopositioning piezoelectric stage (MadCityLabs, Nano-Bio300) or high-dynamics nanopositioner (Physik Instrumente, model P-733.2DD) for high-speed imaging. The piezoelectric positioners were mounted inside a faraday cage, built on an optical table (Newport, RS 2000) to avoid mechanical vibrations, which incorporated acoustic insulation, vacuum insulating panels (Kevothermal) and aluminium heat sinks (aimed at reducing thermal fluctuations and drift of the piezoelectric positioners¹⁶⁹). Electrochemical measurements were performed with a custom-built bipotentiostat equipped with a high sensitivity current follower to measure nanopipette probe currents with a bandwidth of 10 kHz for the current range measured herein. The SICM setup was controlled through a FPGA card (PCIe-7852R, National Instruments) using a home-written program in a LabView interface.

5.3.4 Numerical simulations

The simulation model was built in the Comsol Multiphysics (version 4.4) software package using geometrical parameters of the pipette probes available from TEM data. Numerical resolution of the system of governing differential equations was achieved in a two-dimensional axisymmetric formulation for computational efficiency. The mesh size was refined down to 4 nm resulting in about 140000 triangular mesh elements. For more details of the numerical modeling see Supporting Information SI-1.

5.4 Results

5.4.1 Operational principles

Electrochemical and chemical processes in electrolyte solutions involve a change of the charge state of species near the electrode/electrolyte interface. The change of the charge number and concentration of the different ions results in a corresponding change of electrophoretic mobility, which can be considerable for cases where there is a conversion of neutral molecules into a set of ionic species (e.g. hydrazine oxidation, $\text{N}_2\text{H}_4 - 4\text{e}^- \rightarrow \text{N}_2 + 4\text{H}^+$) or transformation of ions into uncharged undissociated compounds takes place (for instance, the hydrogen evolution reaction, $2\text{H}^+ + 2\text{e}^- \rightarrow \text{H}_2$). Since the conductivity of an electrolyte is determined by the overall concentration and mobility of the charge carriers present in the medium, a local heterogeneous reaction of this type will produce a spatial redistribution of ions near the reactive site, resulting in a variation of conductance within the diffusion layer (concentration-boundary layer near the electrode). The chemical transformation therefore leads to an increase or decrease of electrolyte conductivity and this effect can become detectable with a reasonable amount of redox molecules (with respect to electrolyte concentration). As we demonstrate below, these variations of local ionic conductance within a concentration-boundary layer near electrodes can be successfully accessed with a scanning nanopipette in the SICM configuration and, hence, this opens up the possibility to employ ion conductance probes for imaging electrode (interfacial) reactivity.

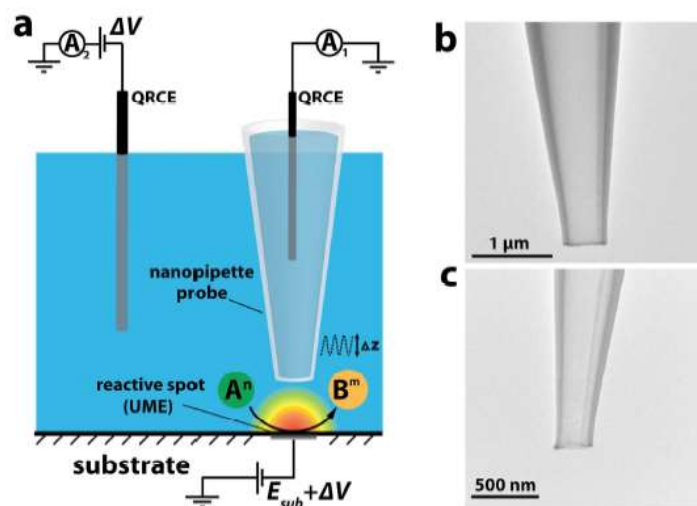


Figure 5.1. a) Schematic representation of the experimental setup for reaction mapping with SICM. b), c) TEM images of nanopipette probes of ~ 200 nm and ~ 100 nm opening radius, respectively.

Figure 5.1a schematically illustrates the working principle of SICM for these functional measurements. Similar to a classical SICM setup, ion current is driven through the pipette tip by the bias, ΔV , applied between the QRCE in the pipette (which is at ground) and that in the solution bulk. This allows accurate vertical tip positioning by using the AC feedback induced by tip oscillation^{167,168} (amplitude, z , as illustrated on Figure 5.1) or bias modulation and the detection of local changes in ionic conductance through the direct current (DC), measured at the current follower A_1 . The rate of the electrochemical reaction at the substrate electrode is controlled by the potential value, $E_{\text{sub}} + V$, with respect to ground, or E_{sub} vs QRCE in the solution bulk. In this case, the current flowing through the current follower A_2 is the sum of the conductance current at A_1 and the faradaic current due to electrochemical oxidation/reduction at the working (substrate) electrode. This electrical configuration requires that the active area of the substrate electrode is small in comparison with the QRCEs in order to keep the conductance current induced by the potential difference between the substrate and the tip at a minimum (see section 5.4.2). If this condition is satisfied, then the nanopipette

can be used to probe dynamic processes at electrodes, as exemplified herein during voltammetric measurements, where the substrate potential is scanned over a wide range and the corresponding conductance current is measured simultaneously at every image pixel. This configuration is particularly advantageous for imaging, as it does not overcomplicate the experimental setup and it brings more versatility compared to other modifications of SICM instrumentation for ion flux imaging.¹⁷⁰

Another important aspect for accurate measurements with SICM is the performance characteristics of the pipette probe, determined by its geometrical parameters. Both the lateral resolution and current sensitivity depend on the mass transport of ions through the nanopipette, which requires precise characterization of the probe (opening size, inner/outer cone angle and glass wall thickness) for quantitative measurements.^{136,171} Figures 5.1b and c show electron micrographs of typical nanopipette probes. As can be seen, pipettes can be reasonably well approximated with a truncated cone shape with opening radii of ~ 100 and ~ 200 nm, and almost constant semi-angle ($3.5^\circ/5.5^\circ$ and $4.2^\circ/6.7^\circ$, inner/outer wall, respectively). This level of detail is important for quantitative data analysis, which can be achieved using simulation tools to treat mass transport and ion conductivity (*vide infra*).

5.4.2 Electrical setup configuration and influence of substrate size

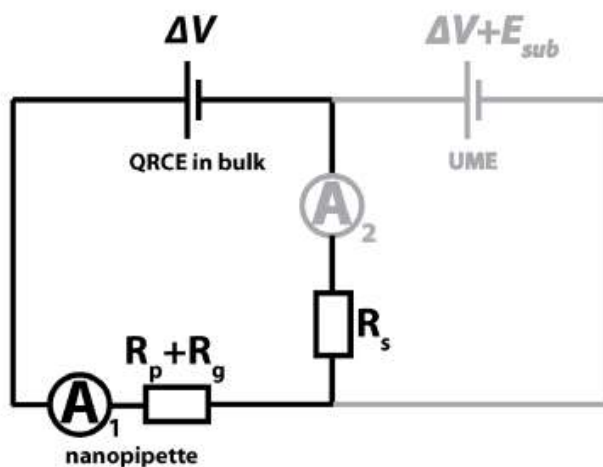


Figure 5.2. Electrical circuit representation of the SICM setup used for mapping reactions. Gray line indicates additional parts of the circuit (compared to classical SICM) for the control of substrate potential.

Figure 5.2 shows the electrical circuit of the SICM setup employed for mapping reactions. In some respects, the configuration is similar to classical SICM setup (black lines), with an additional circuit part for controlling the potential at the substrate electrode (gray lines). The resistances R_p , R_g and R_s denote the resistance of the nanopipette probe, the resistance of tip-to-substrate gap, the resistance of the electrolyte solution (between UME/nanopipette and QRCE in the bulk), respectively. As follows from the simple electrical circuit (assuming no charge transfer resistance at the UME, *i.e.* the worst-case scenario), the current I_{pipette} , flowing through the nanopipette is controlled by the local ion conductance and is given by:

$$I_{\text{pipette}} = \frac{(\Delta V + E_{\text{sub}}) + \Delta V}{R_g + R_p} \quad (\text{Equation 5.1})$$

Therefore, it appears that the potential at the substrate ($\Delta V + E_{\text{sub}}$) can drive ionic current through the pipette. For the studies herein this would be an undesired scenario,

since it implies that sweeping the potential at the substrate will lead to significant ion flow through the nanopipette probe, whereas we seek the nanopipette to be a faithful ion-sensor of the local interfacial environment.

However, the actual electromotive force (emf) of the substrate is not necessarily equivalent to $(\Delta V + E_{\text{sub}})$ and will be largely dependent on the capability of the substrate to pass large enough current. Naturally, the smaller the substrate area A_{sub} with respect to the area of QRCE in the nanopipette A_{QRCE} , the less influence the substrate will have on the nanopipette current. In the first approximation, one can assume the condition

$$A_{\text{sub}} \ll A_{\text{QRCE}}$$

to be valid if

$$1000A_{\text{sub}} = A_{\text{QRCE}}$$

Typical geometric surface area of an Ag/AgCl QRCE (approximated as 250 μm radius cylinder of 5 cm height) is about 0.787 cm^2 , which is equivalent to a disk electrode of 5 mm radius. Taking into account condition eq.5.1, one can conclude that independence of the SICM measurement from the substrate bias will be achieved at electrodes typically not larger than 320 μm in diameter. At the same time, the use of Ag/AgCl QRCEs can bring an advantage of having much larger surface area thanks to a highly porous nature of deposited AgCl layer and a fast electrode reaction, characterized by high current density. On the safe side, measurements are probably limited by $\sim 500 \mu\text{m}$ radius (equivalent area) substrates, but the area could be larger in some circumstances.

5.4.3 Measurements near active reaction sites

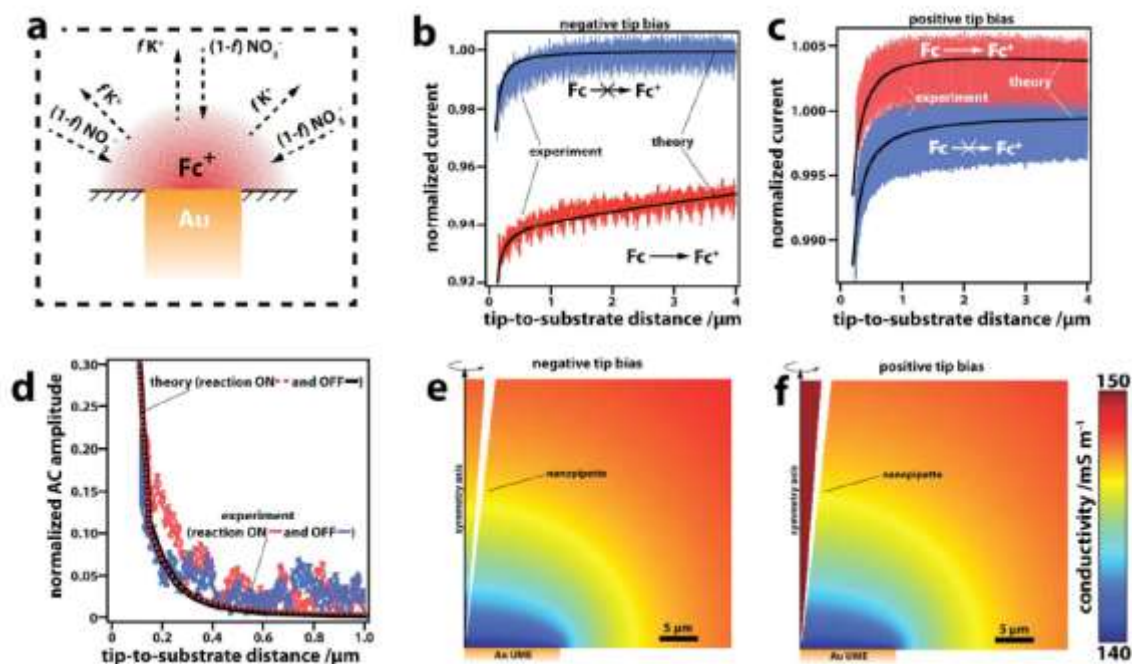


Figure 5.3. Probing the diffusion (concentration-boundary) layer with a nanopipette. a) Schematic representation of the ion redistribution at the diffusion layer of generated Fc^+ adjacent to an Au UME. b), c) Experimental (red and blue traces) and simulated (solid black lines) SICM current-distance curves acquired with a nanopipette (biased at -0.1 and $+0.1$ V, respectively) positioned over an inert (blue) and Fc^+ generating (diffusion-controlled rate) $12.5 \mu m$ radius Au UME (red). Experimental conditions (1.95 mM and 1.45 mM Fc for (b) and (c), with 10 mM KNO_3 in bulk solution, and nanopipettes of 175 nm opening radii as determined by TEM) were mimicked in the simulation with the best fit with an f parameter of 0.925 . d) Experimental (red, reaction on, and blue, reaction off) and theoretical (black and red dashed lines) AC amplitude – distance relationships for a nanopipette positioned over an inert and Fc^+ generating UME. Note that the theoretical curves with the electrode on and off essentially coincide. e), f) Simulated conductivity distributions (magnified view) with a nanopipette (biased at ± 0.1 V) positioned at $1 \mu m$ distance from an Fc^+ generating substrate electrode (Au UME).

The magnitude of ionic fluxes near reactive sites at interfaces (within the concentration-boundary layer) depends on the type of species involved, reaction

stoichiometry and the rate. To exemplify this concept, it is convenient to consider the one-electron transfer that results in the transformation of a neutral redox molecule into an ionic compound, such as ferrocene methanol (Fc) oxidation ($\text{Fc} - e^- \rightarrow \text{Fc}^+$), taking place at a mass transport-limited rate at 25 μm disk Au UME. Electroneutrality requires supporting electrolyte ions to counterbalance the charge of Fc^+ in the diffusion layer by repulsion of f moles of cations and attraction of $(1-f)$ moles of anions for each generated mole of ferrocenium methanol, as illustrated in Figure 6.3a. The conductivity at every location of the solution is therefore the sum of charge carrier concentrations, c_i , multiplied by their respective mobilities u_i and charge numbers z_i . Taking into account the electroneutrality condition as discussed above, the conductivity σ can be expressed using the local concentration of generated Fc^+ :

$$\begin{aligned}\sigma &= F \sum_i |z_i| c_i u_i = F (c_{\text{Fc}^+} u_{\text{Fc}^+} + c_{\text{K}^+} u_{\text{K}^+} + c_{\text{NO}_3^-} u_{\text{NO}_3^-}) \\ &= F [c_{\text{Fc}^+} u_{\text{Fc}^+} + (c_{\text{salt}}^0 - f c_{\text{Fc}^+}) u_{\text{Fc}^+} + (c_{\text{salt}}^0 + (1-f) c_{\text{Fc}^+}) u_{\text{NO}_3^-}]\end{aligned}$$

Herein, f is a factor that determines the local ionic composition within the diffusion layer: for $f = 0.5$ the supporting electrolyte salt (present in solution bulk and in the nanopipette at a concentration c_{salt}^0) balances the generated charge with equivalent cation and anion contributions, while $f = 1$ denotes substitution of electrolyte cations by Fc^+ . The resulting change in local conductivity is thus dependent on the relative amount of species with different electrophoretic mobility (e.g, Fc^+) with respect to the local concentrations of supporting electrolyte ions (K^+ and NO_3^-).

To probe the resulting conductive properties of the concentration-boundary layer, a series of approaches (over an Au UME held at -0.2 V vs bulk QRCE, no Fc oxidation) and retracts (for which the substrate potential was switched to 0.2 V to drive

the diffusion-limited oxidation of Fc into Fc⁺) was performed using ~175 nm radius nanopipette tip. A relatively large nanopipette probe was chosen to avoid any possible additional complications from ion current rectification phenomena¹⁶⁴ to the mass transport through the nanopipette, which can affect both steady-state¹⁶³ and transient^{50,172} measurements, although such effects could be accounted for in the future. As seen from Figures 5.3b and c, an electrochemical reaction at the substrate UME evidently changes the SICM approach curve. Moreover, the contrast between an active and inert substrate is dependent on the polarity of the SICM tip: at negative SICM tip bias there is a noticeable change in conductance across the diffusion layer adjacent to the active electrode (smaller conductance current), while at the opposite (positive) polarity any difference between the inert and active substrate is hardly distinguishable, *i.e.* the measured current-distance approach curves over active and inert electrode are closely similar. Note the difference in the normalized current scale on the plots in Figures 5.3b and c.

To account for this result, a finite element method model was built, taking into consideration the geometrical characteristics of the tip, the substrate, their relative positions, electrolyte properties, and ionic composition of the concentration-boundary layer (see Supporting Information SI-1 for more details). Fitting of the experimental data with the simulation has f as the only adjustable parameter. The best fit was achieved with essentially equivalent substitution of supporting electrolyte cations by the generated Fc⁺ ($f = 0.925$). This value of f provided good agreement with data at both tip polarities as evident from Figures 5.3b and c. The value of f close to 1 indicates a fundamental condition for electrolytes, highlighting that apart from electroneutrality, the ionic strength is also maintained across the medium. Ferrocenium ions, which replace almost equivalent amounts of K⁺ from the electrolyte, have *ca.* 65% smaller ionic

mobility, resulting in noticeable change in the conductive properties of the diffusion layer at the UME, and, more importantly, inside the negatively biased nanopipette tip. Because the nanopipette resistance is the key factor that dominates the ion current at a broad range of probe-to-substrate distances, even a relatively small variation of conductivity within the probe (especially at the tip) leads to a significant change of the overall measured ionic conductance.

Importantly, the strategy adopted, in which the AC component due to tip oscillation was used for positioning, is further advantageous for avoiding the convolution of topographical information with the measurement of local reactivity. The magnitude of the AC current is simply the gradient of the DC current-distance relationship at a particular distance. Figure 5.3d compares experimental and simulated AC ion current amplitude values as a function of tip-substrate separation. The AC components of the nanopipette ion current are most sensitive to the probe proximity to the substrate, where steep changes of tip-to-substrate gap resistance occur, rather than changes of local conductivity, and can therefore be used for reliable probe positioning. As shown on Figure 5.3d, this is well evidenced by the theoretical results and experimental observations, which are all in close agreement, regardless of the substrate activity.

Computed conductivity maps (Figure 5.3e and f) evidence the importance of the probe polarity, which determines the sensitivity of the nanopipette towards the ion flux of generated Fc^+ . At negative tip bias, electrogenerated Fc^+ travels into the nanopipette and accumulates at the tip, leading to the substitution of the more mobile charge carriers, K^+ , by “slow” Fc^+ , and a subsequent increase of the overall resistance. In contrast, at positive tip bias, the imposed electric field at the tip leads to the rejection of Fc^+ cations from entering the probe, and the ionic composition (and conductivity) of the

nanopipette remains almost unaffected (as illustrated on Figure 5.3f), resulting in a very small change of the mass flux through the nanopipette due to the generation of charged species at the UME. This result highlights a further possible means of separating topography and interfacial reactivity in SICM, simply by switching the tip polarity.

5.4.4 Dynamic Voltammetric Imaging

Figure 5.4a demonstrates the application of SICM for dynamic visualization of interfacial reactivity, *i.e.* with a pipette probe (held at constant bias) sensing conductance variations during voltammetric measurement at the substrate. In this example, a ~ 200 nm radius pipette probe biased at -0.25 V was scanned over a ca. 1.2 μm diameter Pt UME, where the electrochemical reduction of protons and oxidation of hydrazine could take place (depending on the applied potential). At every scan pixel, the probe approached the substrate held at -0.2 V with respect to QRCE in bulk solution (to ensure that no significant reactions took place) and as the positionable feedback set point was triggered (AC amplitude threshold), a voltammogram (between potential limits of -1.2 V and 0.75 V) was recorded at the substrate. The resulting data (45 by 45 probe locations, resolved with a 125 nm pitch) comprised a set of lateral and vertical tip positions (sample topography) along with a sequence of 380 substrate and tip current values measured during voltammetric sweep at each probe position (at 2025 locations).

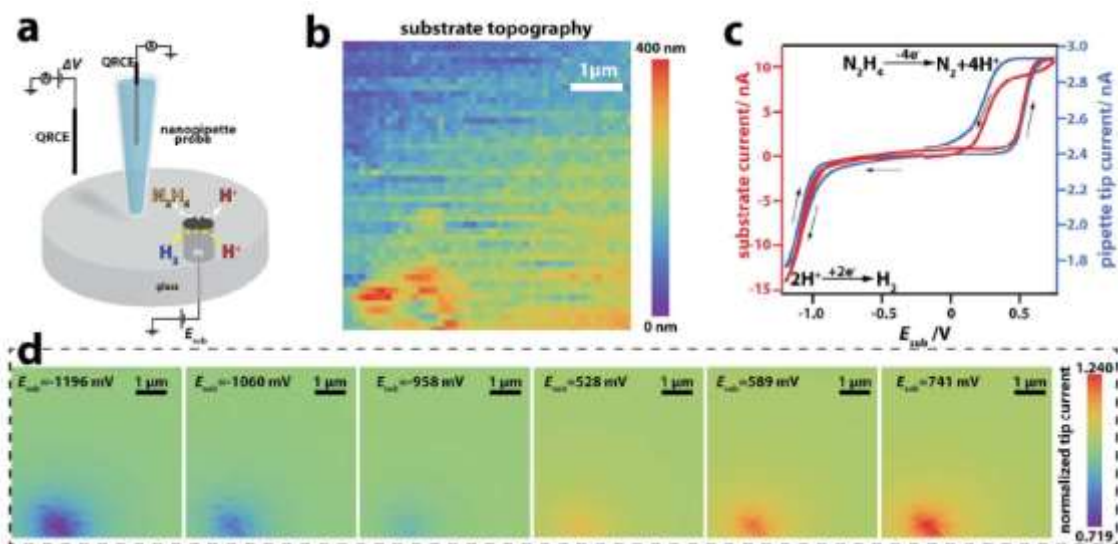


Figure 5.4. Dynamic reaction imaging with SICM. a) Schematic representation of the experimental setup employed for mapping hydrazine oxidation and proton reduction at ~ 600 nm radius Pt UME. b) Topography map (45 by 45 pixels, 125 nm step size) during a hopping scan. The nanopipette, biased at -0.25 V, was approached to the substrate (held at -0.2 V vs Ag/AgCl QRCE in bulk) at every pixel at a speed of 250 nm s^{-1} and then retracted by 1 μ m before being repositioned above the next location. c) Substrate (red) and nanopipette probe (blue) voltammograms acquired with the nanopipette at the central part of the substrate electrode during the potential sweep at the Pt UME (-1.2 V to 0.75 V) at a scan rate 0.5 V s^{-1} . The electrolyte solution contained hydrazine sulfate $N_2H_4 \cdot H_2SO_4$ and KNO_3 at 20.5 mM and 10 mM, respectively. The arrows on the graph indicate the direction of the potential sweep. d) Electrochemical images (6 frames) from a 380-snapshot image sequence, constructed from a voltammetric data resolved at each image pixel. The nanopipette current has been normalized by the value at the point of the closest approach (at each individual pixel) with the substrate potential held at -0.2 V.

The recorded topographical image (Figure 5.4b) evidences some substrate tilt, although thermal drift may also contribute to the image.¹⁶⁹ The important point is that the tip can successfully locate the near interface at a large array of positions. Figure 5.4c exemplifies one of the voltammetric responses (from both the electrode and the pipette tip recorded simultaneously), acquired over the central part of the Pt UME during

imaging. As shown, the nanopipette probe successfully detects changes of ion conductance, caused by consumption of aqueous protons (conductivity decrease) due to electroreduction of hydronium ions in the potential range -0.95 V to -1.2 V, and the release of four H^+ per single hydrazine molecule due to its oxidation at more positive potentials (0.1 V – 0.75 V), which causes an increase of conductivity and tip current. The probe and substrate currents are well-correlated in the reduction part of I-V curve, where the hydrogen evolution reaction occurs. Hydrazine electrooxidation on Pt electrodes (and especially in the presence of H_2SO_4) is a more complex process¹⁷³ in which potential-dependent oxide formation occurs on the electrode surface, leading to a large hysteresis between the forward and reverse voltammetric scans and a rather unusual shape,¹⁷⁴ including a loop (crossing point) on the cathodic and anodic going scans. The corresponding conductance measurements in the diffusion layer demonstrate a typical mass transport-limited plateau. While broadly tracing the voltammetric wave, there is some hysteresis between the substrate voltammogram and tip response on the reverse voltammetric scan that suggests this type of measurement could be mechanistically revealing.

Voltammograms recorded at scan pixels can be conveniently represented as a sequence of images, resolved at a set of discrete substrate potentials. Figure 5.4d shows a few frames, illustrating spatially resolved maps of electrochemical activity. The images demonstrate clear contrast between active (Pt surface) and inert (glass) regions, with the diffuse nature of the active region due to the diffusion of reagents and products. Importantly, because of the procedure adopted, there is no influence from topographical effects, with the image purely representing a reaction-diffusion map. Note that the data shown are neither interpolated nor filtered.

It is further important to note that the recorded images do not evidence noticeable influence from the scanning probe on mass transport at the substrate, which can be an issue for many scanning probe techniques, even with relatively small probes. The geometrical arrangement of SECM (micro or nanoelectrodes with a large glass sheath) or even conical AFM tips often leads to a partial blockage of the diffusion layer at the substrate and therefore results in some perturbation of the measurement.^{175,176} This is not much of an issue for SICM (highly slender probes) as even the presence of a relatively large (~200 nm radius) nanopipette above ~600 nm radius active electrode area has minor influence on the overall substrate electrode current. This is evident from Figures 5.5a and b, which compare maps of the tip and UME currents, respectively, as a function of tip position extracted from the image sequence, at a substrate potential of 0.75 V (mass transport-limited hydrazine oxidation). As can be seen, the substrate current as a function of tip position is relatively uniform, with just a slightly smaller current, seen when the nanopipette probe is above the active area of the Pt disk. The current profiles shown on Figure 5.5c, extracted from potential-dependent substrate current images (as a function of tip position), indicate that the current drop at the substrate is (at most) about 500 pA, which corresponds to only about ~ 5% of redox mediator flux at the microelectrode, in good agreement with numerical simulations (see Section 5.4.5 below). This is a relatively small perturbation, comparable to the blocking effect of optimal AFM tips.¹⁷⁶

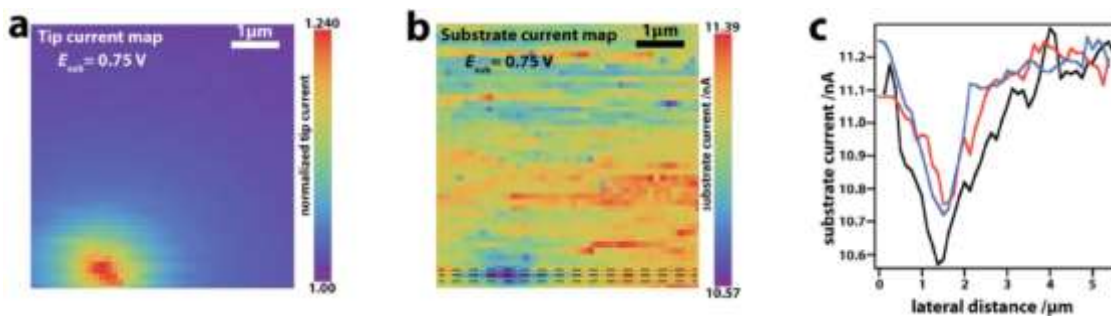


Figure 5.5. The effect of a nanopipette tip on the mass-transport at the substrate. Maps of a) normalized tip current and b) corresponding map of substrate current as a function of nanopipette position at 0.75 V (mass transport-limited hydrazine oxidation. c) Substrate current profiles extracted from substrate current map at positions indicated by dashed lines in b).

5.4.5 Effects of nanopipette tip on measured substrate current

The scanning probe operating above the substrate inevitably causes some perturbation of the mass flux on the sample. In the case of SICM, this perturbation is relatively small and as exemplified in the manuscript does not exceed ca. 5% of the current drop when a $\sim 200\text{ nm}$ radius nanopipette is positioned above $\sim 600\text{ nm}$ radius active electrode area. To support this result, a numerical simulation of the pipette approaching the substrate (for both of the geometrical dimensions were as given above) was carried out. Figure 5.6 demonstrates the substrate current change with the pipette positioned at different tip-to-substrate distances above the electrode. As can be seen, the current reaches about a 5-6% change as the probe approaches working distances about 100–200 nm, in a good agreement with experimental data

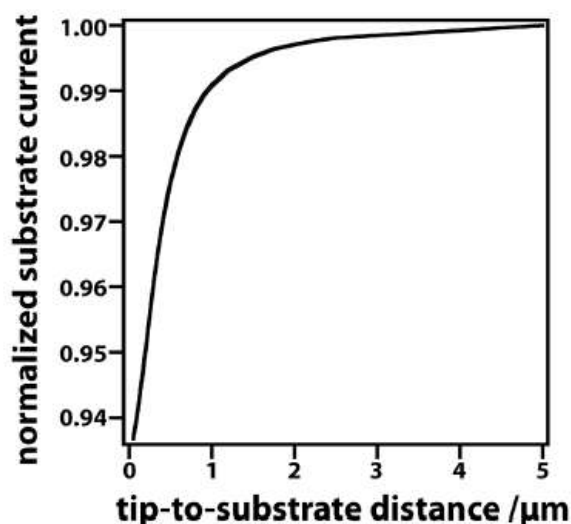


Figure 5.6. The relationship between the normalized current at 600 nm radius disk UME and the tip/substrate distance (nanopipette radius 200 nm).

5.4.6 High-Speed Imaging

While the dynamic imaging described is a very robust approach for studying various electrochemical systems, imaging at high tip scanning rates can offer numerous advantages, from the capability of acquiring a large amount of information (of extended sample areas) to the avoidance of limitations from long imaging times, such as chemical and physical changes to the substrate during the scanning, sample ageing, probe fouling, solvent evaporation, and the instability of electrolyte solutions. As we showed recently,¹⁷⁷ high-speed imaging for SEPMs requires a set of factors to be carefully considered for successful application with a particular technique, including the constraints of the piezoelectric positioners for probe translation, the rate of positional feedback, the characteristic probe response time and the bandwidth of current amplifiers. Most of the imaging limitations can be overcome using a harmonic scan pattern (such as an Archimedes spiral as exemplified herein) for smooth probe translation and a trace/retrace protocol, where a probe is scanned close to the substrate to acquire its topography at a relatively slow scan rate followed by a series of quick

retraces over the set of acquired topographical coordinates (x, y and z). As we show herein, this strategy can be applied to the SICM technique for high-speed imaging of electrochemical activity at interfaces.

Figure 5.7a demonstrates a pre-scan image (acquisition time 390 s) for the electrochemical oxidation of FcTMA⁺ at a Pt electrode (~430 nm radius disk) at 0.4 V recorded at 5.2 $\mu\text{m s}^{-1}$ translation rate with a 95 nm radius nanopipette probe (biased at -0.25 V). The original image contained about 1.52×10^6 pixels, which were smoothed by averaging down to 38091 data points on the presented image, resulting in a pixel density of 162 pixels μm^{-2} . As can be seen, the reaction zone at the UME is clearly resolved, with the lowest probe currents observed above the active region (Pt surface). Similarly to ferrocene methanol oxidation, the generation of FcTMA²⁺ results in a decrease of ionic conductance at the nanopipette tip due to repulsion of the supporting electrolyte cations (K⁺, which has 30% higher ionic mobility than FcTMA²⁺) from the diffusion field.

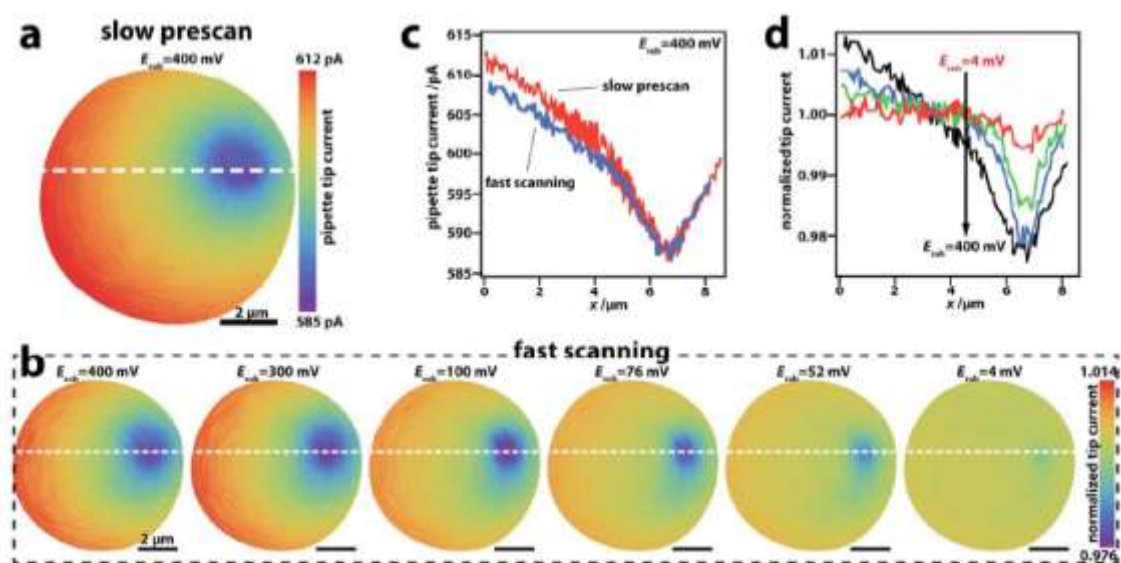


Figure 5.7. a) High-speed electrochemical imaging of reactions with SICM. a) Electrochemical image of ~ 430 nm radius Pt UME (held at 0.4 V) recorded with a ~ 95 nm radius nanopipette biased at -0.25 V vs QRCE in bulk solution during a topographical prescan at $5.2 \mu\text{m s}^{-1}$ in electrolyte solution containing 2 mM FcTMA^+ (diffusion-limited oxidation) and 10 mM KNO_3 . b) A set of high speed images constructed from both forward and reverse scans (for improved image quality) recorded at $180 \mu\text{m s}^{-1}$ probe translational speed at different substrate potentials. The probe currents are normalized with respect to the average ion current for every snapshot. c) Nanopipette current profiles (along the dashed white line on the images) depicting the comparison between high-speed (red) and slow prescan (blue) imaging of diffusion-controlled FcTMA^+ oxidation (substrate held at 0.4 V). d) Normalized tip current profiles, demonstrating the effect of the substrate potential on the normalized tip current. Red, green, blue and black lines correspond to substrate electrode potentials of 4, 52, 76 and 400 mV vs QRCE in solution bulk, respectively. White dashed line on a) and b) denotes the position of the current profiles shown on c) and d). Scale bar $2 \mu\text{m}$. Note, the current data was smoothed using Gaussian filter.

Following acquisition of the substrate topography, a series of 202 high-speed frames (101 forward and reverse) was collected with a probe operating at a speed $180 \mu\text{m s}^{-1}$. Each image frame has been resolved at a constant substrate potential, which ranged from 0.4 V (mass transport-limited oxidation of FcTMA^+) to 0 V (no FcTMA^{2+}

generation) with a step of 4 mV between images. Figure 5.7b depicts six of the acquired images, constructed from both forward and reverse scans recorded at a rate of ca. 4.16 seconds per frame with ca. 16250 pixels per image. As illustrated by the image sequence, the nanopipette tip current contrast vanishes gradually with a decrease of electrode activity: as the FcTMA^+ oxidation process is switched off at the substrate UME, the less is the change of ionic composition near the active electrode area (compared to bulk).

Interestingly, convection does not seem to play a major role for imaging at such a high frame rate. As can be seen, for example by comparing the slow and fast images in Figures 5.7a and b at 0.4 V, scanning at elevated rates does not significantly compromise image quality. Figure 5.7c depicts the tip current profiles across the central part of the UME in cases of slow (preliminary scan) and high-speed imaging and confirms a minor influence of probe translation on the measured ionic fluxes. As can be seen, there is little difference between the probe current profiles even for a 35-fold increase (from 5.2 to $180 \mu\text{m s}^{-1}$) of the probe scanning rate.

Figure 5.7d demonstrates the current profiles across the image frames recorded at different substrate potentials. The magnitude of the current change between the active electrode and surrounding glass diminishes with a decrease of the reaction driving force (overpotential) and this is well evidenced from the current profiles and the resolved images. As can be seen, the sensitivity of the technique is high enough to detect variations of the local conductivity even at a very low overpotential (with the substrate biased at 4 mV vs QRCE in the bulk). The presented current profiles also suggest that the diameter of the active area of the substrate UME is around $0.7 - 0.8 \mu\text{m}$, very close to the Pt disk size of $\sim 860 \text{ nm}$ (estimated from voltammetry), providing a good estimate of active region size even at a very large translation rate and regardless of the magnitude

of the change in ionic compositions near the active site, as determined by the reaction rate at the electrode.

5.5 Conclusions

Scanning ion conductance microscopy has been shown to be a powerful technique for imaging electrochemical reactivity at interfaces. The magnitude of the ionic current flowing through the nanopipette probe is very sensitive to the local conductivity changes that occur near active sites and can be used for probing the spatial distribution of ion fluxes, arising due to (electro)chemical transformations. Along with the high resolving power intrinsic to SICM, the technique brings several important advantages over other electrochemical imaging methods, thanks to the simple protocols for probe fabrication, the possibility of simultaneous tracking of topography and reactivity, easily tunable probe size and a small extent of perturbation exerted on the mass fluxes at the substrate. Moreover, ion current measurements can be made with a high degree of accuracy. This makes SICM reactive imaging a very attractive alternative for the characterization of (electro)catalytic materials. At the same time, the possibility to translate the probe at very high scan rates (up to 1000 probe diameters per second) offers exciting opportunities for high-speed imaging with the frame rate approaching 4 s per snapshot with high pixel resolution.

A considerable issue in SEPM is the separation of topography and activity effects, and in this paper we have identified two simple approaches to resolve this problem. First, by using a distance-modulation SICM approach, we have shown that the resulting AC SICM current at the modulation frequency is relatively insensitive to reactivity of the surface, so that a combination of simultaneous AC and DC SICM measurements reveals both the substrate topography and the activity. Second, the potential applied to the SICM probe can be selected so that the DC probe response is

sensitive to either the topography or activity. These deductions were aided by detailed finite element method modeling that allowed a thorough assessment and analysis of ion fluxes with the SICM reactive imaging technique.

5.6 Acknowledgment

This work was supported by the European Research Council through Project ERC-2009 AdG 247143-QUANTIF and a Marie Curie IntraEuropean Fellowship 626158 FUNICIS (D.M.). The authors also acknowledge Ms. Sophie L. Kinnear for her kind help with software development, Dr. Robert A. Lazenby for fruitful discussions about experimental setup and Dr. Alex Colburn for high-speed current amplifiers.

Appendix

Electrochemistry is a highly instrumental subject and most (if not all) measurements are performed through an instrument. Electrodes, disregarding their nature, effectively bridge (electro)chemical reactions with the measurement instrument and allow us to probe those reactions by monitoring interfacial reaction occurring at the electrode/electrolyte interface. Not surprisingly, most of the experiments and results presented so far were obtained through high-end highly sophisticated electrochemical instruments, mostly potentiostats. Although desirable, sophisticated (and thus powerful) equipments are not necessary for teaching and for (some) research applications. In most applications, a simple potentiostat would suffice and the use of high-end equipment not only add an unnecessary cost to the limited research budget, but also pushes the user (student/researcher) away from the principles of operation of the equipment due to sophisticated machinery (difficult to understand) and/or to a “black-box” type of construction. This can lead to a limited adoption of electrochemical techniques due to the high cost involved and to a total disregard of the instrumentation impact on the experimental outcome by the user due to the complicated instrumental design.

The costs involved are specially concerning when we look at developing countries, which have very limited budget for R&D and hence cannot justify the cost of high-end equipments. This is even more troublesome due to the large applicability of electrochemical techniques in the basic and life sciences. The disregard to the instrument impact on the experimental outcome is deeply concerning specially for “cutting edge” research application where non-trivial, non-well behaved, chemical systems are usually studied. The naïve assumption that the equipment has no limitations can lead, and will lead, to a false interpretation of the experimental results.

The arguments presented so far showcase the need for an accessible electrochemical instrumentation that is both low-cost and simple in design. Such platform will be of great value for teaching applications, where the principles of operation of the equipment can be explored, and for research application for places with a budgetary restriction, as it would function as an R&D platform where people can build upon it and design an equipment tailored to their own needs. Appendices 1 and 2 explore the pursuit for such instrumentation platform, with Appendix 1 exploring the design and operation of a simple, yet capable, potentiostat based on a microcontroller that can perform basic electrochemical measurements on well behaved systems. The electronic design and instrumental limitations of the proposed equipment are thoroughly explored and explained allowing the full understanding of the operation and a possible replication of the proposed equipment. Appendix 2 pushes further the instrumental design proposed in Appendix 1 and, by employing “off-the-shelf” electronic components and custom design 3D printed parts, presents the design fabrication and application of a fully functional Scanning Electrochemical Microscope (SECM) capable of performing space resolved electrochemical measurements using a microelectrode as a scanning tip. Both the proposed designs are fully functional, simple to understand and fabricate and “low-cost”.

A1. Building a Microcontroller based potentiostat: An Inexpensive and versatile platform for teaching electrochemistry and instrumentation.

*Gabriel N Meloni**

Instituto de Química, Universidade de São Paulo. São Paulo, SP, Brazil

*e-mail: Gabriel.meloni@usp.br

*To whom correspondence should be addressed

A1.1 Abstract

A versatile potentiostat based on inexpensive and “off the shelf” components is reported. The platform was shown to be capable of performing simple electrochemistry experiments, suitable for undergraduate level teaching. The simple design and construction enable easy customization to accommodate a broad array of experimental designs. The equipment was used to calculate the diffusion coefficient of potassium ferricyanide in an aqueous solution, and the obtained result was in good agreement with the literature. Although simple in design, the low cost and good performance of the device make it a competitive alternative for teaching laboratories in the fields of both electronics and electrochemistry, and for developing teaching centers that cannot afford a commercial device.

A1.2 Introduction

Modern equipment construction and design often rely on a “black box” construction philosophy, pushing the user away from the principles of operation of the machine and transforming itself into a “data spitting” equipment.¹⁷⁸ Most of these design decisions are under the pretext of making the operation easy by means of a maintenance free and user-friendly equipment, but in fact, they end up preventing the full usage of the equipment capabilities and true understanding of the collected data.

With the rise of the do-it-yourself (DIY) culture and the constant growth of DIY enthusiasts, powerful prototyping platforms have become affordable and accessible for everyone. In this scope, Arduino microcontroller boards based on the ATMeaga microcontroller family stand out because of their outstanding capabilities, affordable price, and support community. Owing to these characteristics, Arduino based measuring equipment and sensors such as thermometers, pH-meters,¹⁷⁹ photometers,¹⁸⁰ and PCR thermal cyclers,¹⁸¹ are making their way into teaching laboratories as powerful teaching tools.^{181,182} Although a few potentiostats have been reported elsewhere,^{183,184} they usually rely on expensive electronic hardware and custom software in order to achieve high precision levels. On this note, we present the design and fabrication of a simple, cheap, and customizable Arduino based potentiostat that relies only on open software programs and a handful of “off the shelf” electronic components capable of performing basic electrochemical measurements in teaching laboratories. The proposed platform can be used as a multidisciplinary experiment for exploring both the electrochemistry and electronic aspects.

A1.3 Materials and methods

A1.3.1 Potentiostat fabrication

Potentiostats are simple devices that rely on operational amplifiers to keep a desired potential difference between two electrodes (working and reference electrodes) immersed in a solution while recording the electrical current that flows between them. Normally a third electrode (counter electrode) is added to the system in order to isolate the electrode used as a potential reference (reference electrode) from the charge transfer reaction.¹⁸⁵ A basic potentiostat can be assembled using a handful of simple electronic components consisting of some resistors, capacitors, and operational amplifiers. A circuit diagram of the electronic components used in the fabrication of the proposed

potentiostat and a device fabricated using a custom etched printed circuit board can be seen in Figure A1.1 and A1.2. This diagram represents the potential controlling and current measurement parts of the equipment, where all the analog electronics are. A photo of the actual device used on the measurements herein presented, fabricated using a breadboard type construction, can be seen in Figure A.1.2.

The proposed device uses an Arduino microcontroller board (Arduino Uno, Arduino) for parameter control and data acquisition. The Uno board runs a basic sketch (see supporting information) that enables the user to perform simple cyclic voltammetry (CV) experiments by choosing the start potential, vertex potential (inflexion on the E vs. t curve), and scan rate. The script can be easily understood and changed to perform different experiments (such as chronoamperometry), making the platform extremely versatile. The device potential window and current limits are defined by the summing amplifier (Figure A1.1ii(A)) and the transimpedance amplifier (Figure A1.1ii(C)), respectively. These are further explained in the manuscript.

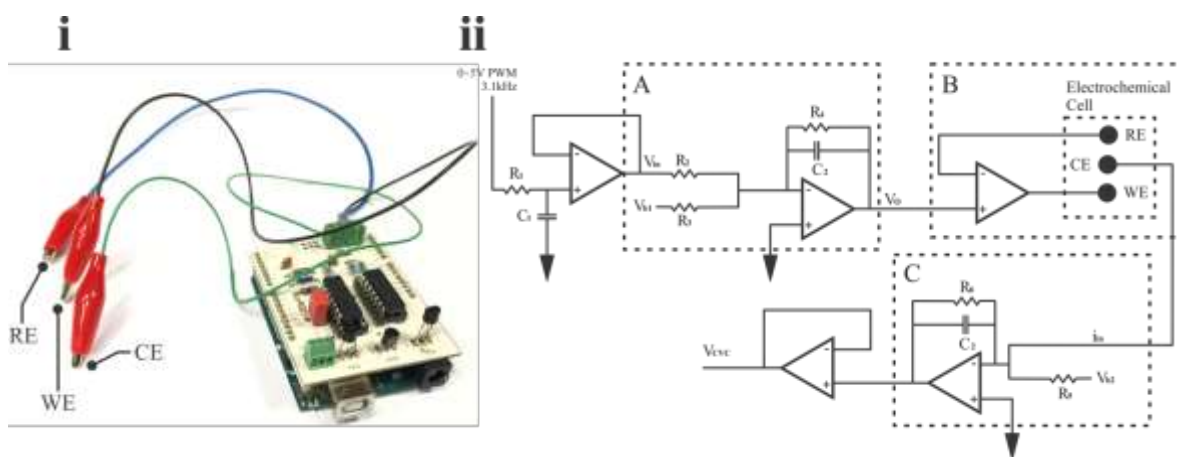


Figure A1.1. i) Possible construction of the device using a custom etched printed circuit board ii) Analog circuit of the potentiostat with highlighted A: summing amplifier; B: electrochemical cell and electrochemical cell potential controlling amplifier; and C: transimpedance amplifier (current to voltage converter).

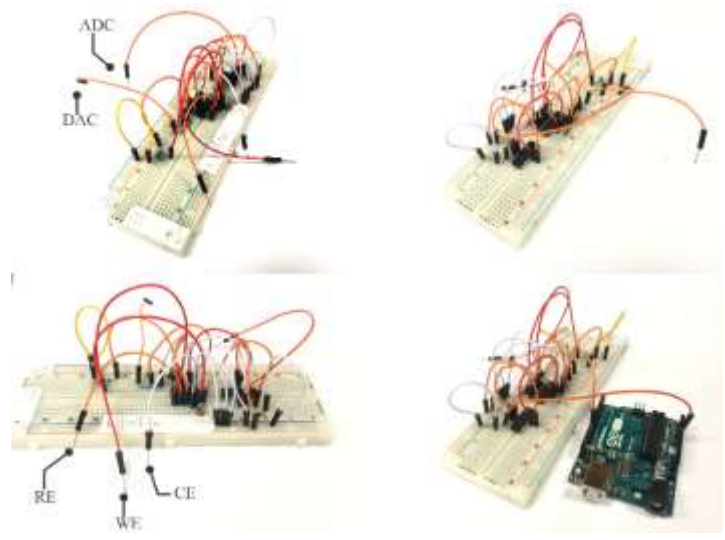


Figure A1.2. Pictures of the device used on the experiments showing its breadboard construction. Highlighted are the jumper wire connections to the ADC and DAC (top left image) and to the reference, counter and working electrodes (bottom left picture).

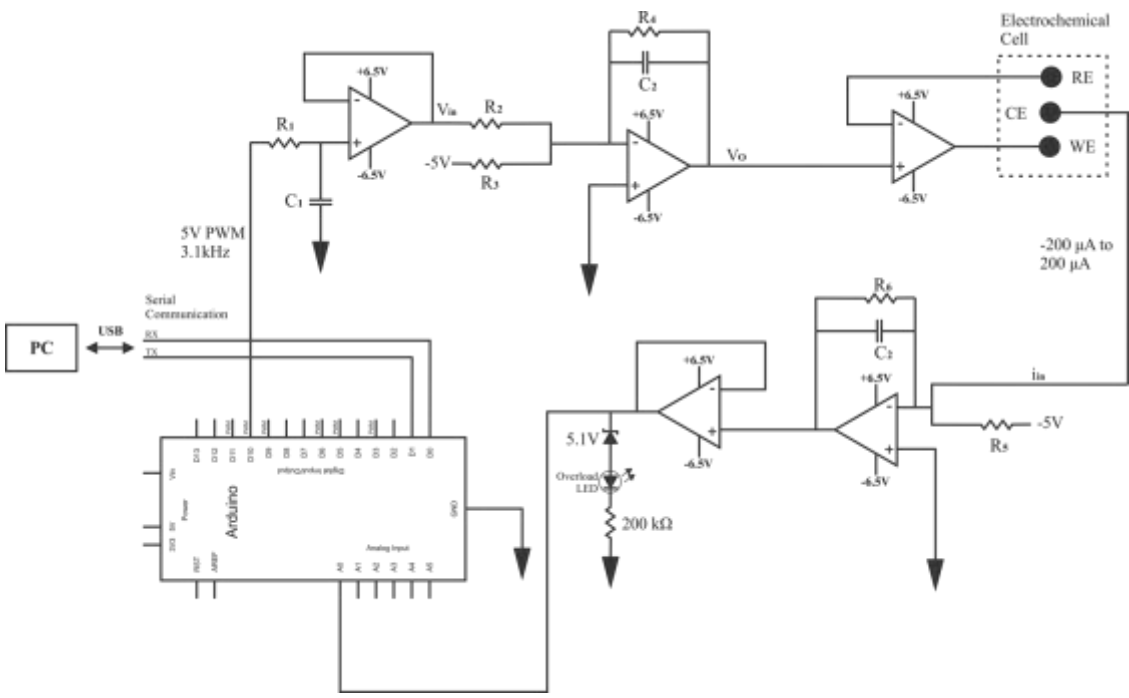


Figure A1.3. Full schematic design of the potentiostat including the Arduino board pin connections.

A1.3.2 Power supply

Most operational amplifiers (Op-Amp) such as the LM324 (Texas Instrument) used on this report are usually powered by symmetrical power supplies *i.e.* they need to be powered with both a positive and negative voltage (symmetrically) with respect to ground. Although this is not true for all Op-Amp applications, it is true for the proposed circuit. The +/- 6.5V supply shown on figure S1 are designed to allow for a +/- 5V output on the Op-Amp (after the internal voltage drop, commonly 1.5V) which is within the microcontroller capabilities as described further. This is not necessary and is intended to be a failsafe to avoid damage to the microcontroller, as it is the 5.1V Zener diode connected between the output of the ADC (Figure A1.1ii (C)) and ground. The LM324 quad Op-Amp can be powered with a dual power supply up to +/- 16V with respect to common ground¹⁸⁶ and thus can be powered by a PC ATX power supply +12V and -12V rails. ATX power supplies are readily available and can be often salvage from old PC without adding any cost to the project.

The -5V supplied to the summing amplifier and ADC (Figure A1.1ii (A) and A1.1ii (C)) should be stable and precise, as any fluctuation on this voltage will cause an offset on both the applied potential to the electrochemical cell and the current read from it. A voltage regulator such as the LM79L05 can be used to provide a stable -5V from the -12V rail of the ATX power supply.

A1.3.3 Digital to analog converter (DAC)

As the Arduino Uno boards do not have a true digital to analog converter (DAC) but only pulse-width modulation (PWM) and for a cyclic voltammetry experiment, a potential ramp should be applied on the potential controller (Figure A1.1ii (B)), the square wave generated by the PWM must be converted into a potential ramp. One

alternative is to use an RC filter to convert PWM values into true analog values. The drawback of using this approach is that for an Uno board the PWM has an 8-bit resolution, generating only 256 discrete potential values. This might result in poorly defined voltammograms, especially if performing experiments with less than the maximum and minimum potential limit of the equipment. The summing amplifier as seen in Figure A1.1ii (A) gives those limits. Besides the resolution problem, most Arduino boards have low frequency PWM signal, ranging from 400 Hz to 960 Hz¹⁸⁷, resulting in a high time constant for the RC filter. These frequencies are determined by an integer divider on the internal clock of the board, meaning that the frequency can be changed by changing the divider value, resulting in frequencies up to 31 kHz, much more suitable for the intended application. Table A1.1 lists the truth table for the PWM based DAC.

Table A1.1. Truth table for the summing amplifier, showing its voltage output as a function of the DAC voltage/PWM level.

Input (V/PWM level)	Output (V)
0/0	1
2.5/127	0
5/255	-1

The PWM voltage of the Uno board is 5 V and the DAC can only provide voltages from 0 to 5 V. Thus, a summing Op-Amp is needed for cyclic voltammetry experiments as we are interested to vary the potential between negative and positive values. As most of the teaching experiments in electrochemistry are performed in water and the electrochemical window for water is not greater than 1.5 V for most working electrode (WE) materials, there is no point in sweeping the potential up to 5 V. Thus, the summing amplifier can be designed to output voltages in a more usable range. As the 8-bit resolution will be used in the whole span of the potential window, the design of

the summing amplifier is a compromise between the potential resolution and potential window width. The width of the window can be adjusted by changing the values of V_{b1} , R_2 , R_3 , and R_4 (Figure A1.3). Applying Kirchhoff's law and Ohm's law on the inverting input of the summing amplifier, it can be easily seen that the relation between V_O , V_{in} , V_{b1} , R_2 , R_3 , and R_4 is given by

$$V_O = -R_4 \left(\frac{V_{in}}{R_3} + \frac{V_{b1}}{R_2} \right). \quad (\text{Equation A1.1})$$

Figure A1.4 shows a plot of the output of the DAC and summing amplifier for the setup described in Figure A1.3.

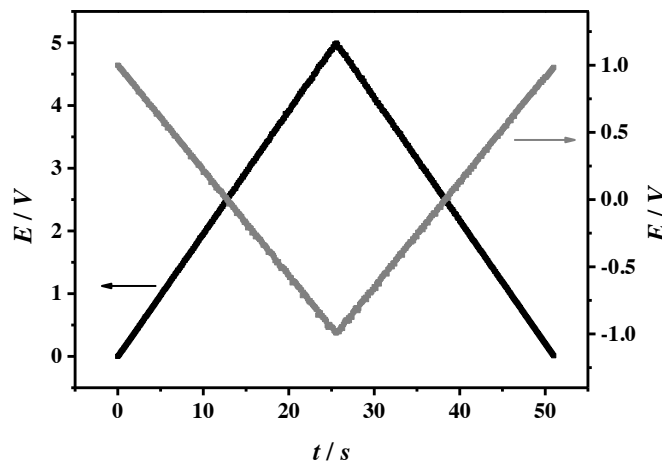


Figure A1.4. E vs. t plot of the DAC output (black line) and summing amplifier output (grey line).

A1.3.4 Scan rate

The maximum scan rate for the designed device is dependent on the rise time of the RC filter used on the ADC. In addition, the potential window and resolution will affect the maximum scan rate. All those parameters can be changed allowing for some experimental setup flexibility. As the DAC bit resolution is fixed (8-bit) the DAC can generate 256 different levels. With a potential window of 2V (from -1V to 1V) as used

for the electrochemical experiments, the DAC resolution is 0.0078V. With a DAC RC filter rise time of 0.01s (10kΩ resistor and 470nF capacitor and 31kHz PWM) the maximum scan rate on the setup used for the electrochemical experiments would be 0.780mVs⁻¹. The maximum scan rate of the device is defined by:

$$v_{max} = \left(\frac{E_w}{2^{256} / RC_t} \right) \quad (\text{Equation A1.2})$$

Where:

v_{max}	Maximum scan rate value (Vs ⁻¹)
E_w	DAC potential window width (V)
RC_t	DAC RC filter rise time (s)

A1.3.5 Analog to digital converter (ADC)

The current reading part of the equipment is highlighted in Figure A1.1(B) and it consists of an Op-Amp in a current to voltage converter setup (transimpedance amplifier) connected to the counter electrode (CE). The current to voltage converter (CVC), as its name suggests, converts the current that flows through the electrochemical cell into a potential that the microcontroller can read. To avoid any damage to the microcontroller the Op-Amps are supplied with +6.5 V, which is within the microcontroller limits. This means that an overload in the current reading will only result in a saturated amplifier and not cause damage to the equipment. The current limit is given by the resistor R_6 (Figure A1.3) connected to the transimpedance amplifier feedback loop. Using the property of Op-Amps^{185,188} and Ohm's law, one can easily see that the current limit is given by

$$V_{CVC} = i_{in} \times R_6 \quad (\text{Equation A1.3})$$

where V_{CVC} is the output voltage of the converter. The potentiostat was designed to use the maximum dynamic range of potential reading from the microcontroller (0-5 V) and engineered taking into account that the Arduino Uno board does not read negative potentials, meaning that a value of 0 A on the current to voltage converter should result in 2.5 V (Table A1.2). This was achieved by the addition of a bias potential on the inverting input of the amplifier.

Table A1.2. Truth table of the current to voltage converter, showing its voltage output and ADC level as a function of the current flowing through the counter electrode.

Input (μA)	Output (V)	ADC level
-200	0	0
0	2.5	511
200	5	1023

Table A1.3. Component values used during the electrochemical experiments on the main manuscript. Components are labeled as on Figure A1.3.

Component label on Figure S1	Component Value
R1	10k Ω
R2	510 Ω
R3	1k Ω
R4	200 Ω
R5	24k Ω
R6	12k Ω
C1	470nF
C2	100nF

Table A1.4. Current and voltage limits for the potentiostat used during the experiments performed in the main manuscript.

	Min.	Max.
Potential (V)	-1	1
Current (μA)	-200	200
Voltage compliance (V)	-5	5
Scan rate (Vs^{-1})		0.780

A1.4 Results

A1.4.1 Resistors polarization curve

To assess the capabilities of the fabricated equipment and to verify if it was working as expected, a 1 k Ω and 10 k Ω resistor were used. These resistors were connected between the working electrode and the counter and reference electrode (which were short circuited together). The well-behaved and well-known response of these electronic compounds when submitted to a potential ramp make it easy to evaluate the performance of the equipment. When a potential is swapped between the leads of a resistor, the measured current is expected to show a linear response with a slope that corresponds to the inverse of the resistance value of the resistor (I/R). As seen in Figure A1.5, the expected behavior is observed and the resistances can be calculated as being $1044.9 \pm 0.4 \Omega$, $10584.5 \pm 19.0 \Omega$, $5273.7 \pm 4.5 \Omega$ for the 1 k Ω , 10 k Ω , and 5 k Ω parallel resistor association, respectively. These values are in good agreement with the 10% tolerance resistor used.

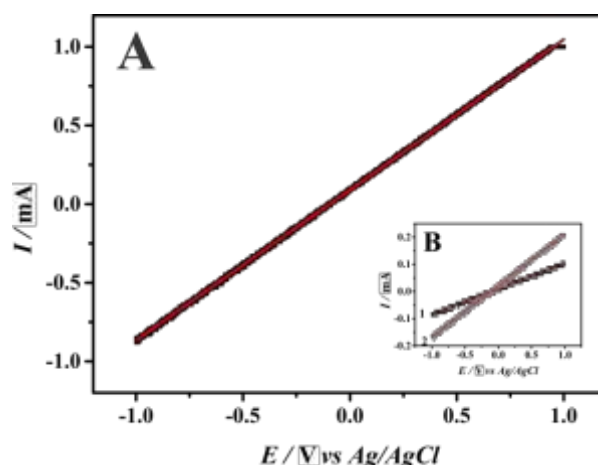


Figure A1.5. Dots: Polarization curves for A: 1 k Ω resistor, B1: 10 k Ω resistor, and B2: 5 k Ω parallel resistor association. Line: Linear fit for the obtained curves with $R^2 = 0.9996$, 0.9984 , and 0.9933 for 1 k Ω , 5 k Ω , and 10 k Ω , respectively.

A1.4.2 Diffusion coefficient determination

In order to prove the capabilities of the potentiostat, a basic electrochemical experiment based on the redox reaction of potassium ferricyanide salt in water was performed. The diffusion coefficient of potassium ferricyanide was calculated by recording CV experiments in a solution containing a known concentration of the salt for different scan rates and using the Randles-Sevcik equation (See below).

$$i_p = 268,600n^{\frac{3}{2}}AD^{\frac{1}{2}}Cv^{\frac{1}{2}} \quad (\text{Equation A1.4})$$

Randles–Sevcik equation at 25°C¹⁸⁹ where:

<i>i_p</i>	Peak current	Ampere
<i>n</i>	Number of electrons involved on the reaction	
<i>A</i>	Area of the electrode	cm²
<i>C</i>	Concentration of the electroactive species	mol/cm³
<i>v</i>	Scan rate	V/s
<i>D</i>	Diffusion coefficient	cm²/s

Although simple, this experiment is widely used as it illustrates the important electrochemical aspects and parameters¹⁸⁹ to students dealing with electrochemistry or CV for the first time. The values of all the components used for the setup during the electrochemical experiments are given in detail in Table A1.3. A platinum working electrode with a diameter of 1.6 mm was used in a conventional three-electrode electrochemical cell. An Ag/AgCl wire was used as a quasi-reference electrode and a platinum wire as a counter electrode. The electrochemical cell was filled with 19.35 mM potassium ferricyanide in 0.1 M KCl solution. The potential was swapped between 1 V and -1 V with scan rates of 0.01 Vs⁻¹, 0.02 Vs⁻¹, 0.05 Vs⁻¹, 0.10 Vs⁻¹, 0.20 Vs⁻¹, 0.25 Vs⁻¹, and 0.3 Vs⁻¹. The recorded data can be seen in Figure A1.6.

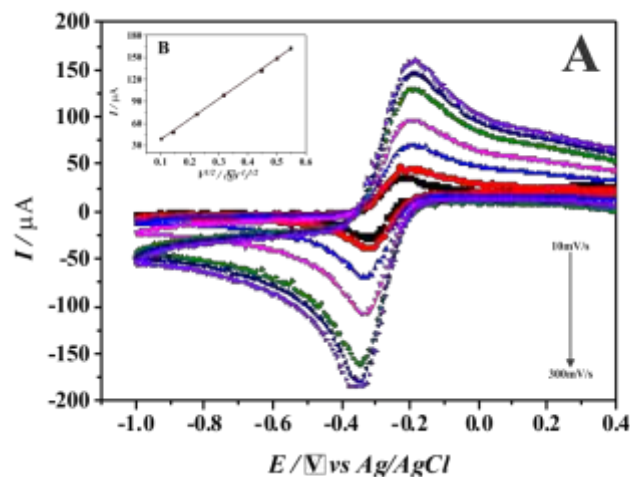


Figure A1.6. Cyclic voltammogram recorded on a platinum working electrode in 19.35 mM potassium ferricyanide in 0.1 M potassium chloride solution with scan rates of 0.01 Vs^{-1} , 0.02 Vs^{-1} , 0.05 Vs^{-1} , 0.10 Vs^{-1} , 0.20 Vs^{-1} , 0.25 Vs^{-1} , and 0.30 Vs^{-1} . Inset B: Linear fit of the anodic peak currents against the square root of the scan rate.

As expected, Figure A1.6 shows an increase in the recorded electrochemical current with an increase in the scan rate. Figure A1.6(B) shows the plot of the anodic peak current vs. the square root of the scan rate. As expected, the plot is a line and a linear fit with an R^2 of 0.9993 is obtained. From the slope of the linear fit and Randles-Sevcik equation, the diffusion coefficient of potassium ferricyanide is calculated to be $6.93 \times 10^{-6} \pm 0.07 \times 10^{-6} \text{ cm}^2\text{s}^{-1}$, which is in good agreement with the value in the literature.¹⁹⁰

A1.5 Conclusion

It is demonstrated that the fabrication and design of a simple potentiostat that is capable of resolving a current of the order of a few μA is possible using no more than a handful of simple and readily available electronic components. The simple design makes it possible for students with a basic electronics background to understand how a potentiostat operates and to recognize the equipment limitations and sources of error.

The proposed device can be applied in joint teaching experiments encompassing electrochemistry, electronics, and programming. Although somehow limited, especially when compared with commercial equipment, the fact that the proposed device costs less than \$30.00 in materials (including the Arduino Uno board) makes it a competitive alternative for places where electrochemistry experiments take place on computer software or web based simulators.

A1.6 Acknowledgements

The author would like to thank Mr. Rod Wesson (University of Warwick, senior electronic technician) for the helpful discussions.

A2. 3D printed and Microcontrolled: The one hundred dollars Scanning Electrochemical Microscope.

*Gabriel N Meloni**

Instituto de Química , Universidade de São Paulo. São Paulo, SP, Brazil

*e-mail: Gabriel.meloni@usp.br

*To whom correspondence should be addressed

A2.1 Abstract

The design and fabrication of a versatile and low-cost Electrochemical Scanning Probe Microscope (EC-SPM) is presented. The proposed equipment relies on the use of modern prototyping tools such as 3D printers and microcontroller boards and only a few “off-the-shelf” parts to deliver a simple yet powerful EC-SPM equipment capable of performing simple space resolved electrochemical measurements. The equipment was able to perform space resolved electrochemical measurements using a Platinum ultramicroelectrode (UME) as the working electrode on a Scanning Electrochemical Microscopy (SECM) configuration and was used to record approach curves, line scans and array scans over an insulating substrate. The performance of the proposed equipment was found to be adequate for simple SECM measurements under hindered diffusion conditions. Due to its flexible design (software and hardware), more complex array scan patterns, only found on high-end EC-SPM setups such as hopping mode scan, were easily implemented on the built equipment. Despite its simplicity, the versatility and low cost of the proposed design make it an attractive alternative as a teaching platform as well as a platform for developing more elaborate EC-SPM setups.

A2.2 Introduction

Electrochemical Scanning Probe Microscopy (EC-SPM) techniques such as Scanning Electrochemical Microscopy (SECM) are powerful tools for investigating surfaces and interfaces, exploring electrochemical activity and probing kinetics at the sub-micron level.¹⁻³ Recent advances dramatically improved EC-SPM spatial resolution to the order of a few nanometers,^{25,84,141,142} opening the possibility of applying such techniques to single entities analysis, like single cells and single nanoparticles,⁷⁻¹¹ high-resolution topographic mapping,^{14,15} local ion flux, and local conductivity measurement, among others.^{9,16-19} The use of multifunctional probes, coupling more than one EC-SPM technique on a single probe, also extended further the experimental capabilities of those techniques making them attractive for a broad range of research subjects.^{16,19,21,45} However, SECM and EC-SPM in general, have not been widely adopted as other electrochemical techniques, being restricted to a small community despite having been described in the literature for almost 30 years.⁴ The complex instrumentation, demanding specially trained users, and the high costs involved favor the gradual adoption of EC-SPM by the scientific community which could be promoted by the development of easy to use and accessible instrumentation.^{191,192}

Although EC-SPM needs a specific instrumentation to couple the translation of the electrochemical probe over a substrate with different electrochemical techniques, modern fabrication and prototyping tools, that are now available to final consumers, can achieve the level of precision necessary for producing such specific parts and could be used to manufacture fully functional equipment. In this sense, 3D printers and microcontrollers stand out as flexible and cost efficient fabrication and prototyping alternatives for custom built laboratory equipment. Even though they require the use of specific programs to operate, online support and teaching material can be easily found

enabling the most inexperienced user to operate those tools efficiently in little time. Not surprisingly, 3D printers and microcontrollers are finding more space in research laboratories and teaching facilities.^{76,80,179,180,182,193,194}

Herein the design, fabrication, and operation of a custom EC-SPM equipment capable of performing basic space-resolved electrochemical experiments that cover the basic principles behind the use of a SECM, are presented. These principles are not only interesting for teaching SECM but also can be utilized, in a much broader sense, to approach basic electrochemistry principles such as mass transport phenomena and electron transfer kinetics, when teaching general electrochemistry.^{40,71,124,195} The proposed design makes use of 3D printing, microcontrollers and only a few “off-the-shelf” electronic and mechanical components resulting in an easy to build and operate, accessible and low-cost SECM equipment that can be used not only as a teaching tool but also as a developing platform for building a EC-SPM rig.

A2.3 Materials and methods

A2.3.1 Chemicals

All solid reagents were of analytical grade and were used as received. Methyl viologen, potassium ferricyanide, and potassium chloride were obtained from Sigma-Aldrich (St. Louis, MO, USA). All solutions were prepared using deionized water (Millipore, Billerica, MA, USA). The supporting electrolyte concentration was kept the same (500 mmol.L⁻¹ of potassium chloride) for all solution.

A2.3.2 3D printed parts.

All 3D printed parts were fabricated using the fused deposition method (FDM) on a commercial 3D printer (CL1 Black, Clever, Brazil) using 1.75 mm polylactic acid (PLA) filament of different colors. Before printing, the parts were designed using a computer aided design (CAD) software (Autodesk Fusion 360) and exported to the printer's proprietary slicer software where the printing parameters could be set. For all the 3D printed parts the printer parameters were kept the same, 50% infill and 135% of the maximum printer speed (value not specified by the manufacturer). Extruder and printing bed temperature were set for each of the filaments used according to printing performance on a test piece. Due to a careful CAD design, no rafts or supports were needed for any of the printed parts allowing them to be used out of the printer without further finishing process. The 3D models are available in Section SI-1 of the supporting information.

A2.3.3 Electrochemical measurements

All experiments were performed in a two-electrode configuration consisting of a 15 μm diameter Platinum microelectrode as a working electrode, and a AgCl coated silver wire as a Quasi-Reference Counter Electrode (QRCE). During the space resolved electrochemical experiments, the Platinum microelectrode was used as a SECM tip and a highly polished silicon wafer surface, partially covered with a layer of polyimide tape was used as a substrate. The polyimide tape forms a step on the substrate otherwise flat surface that can be used as a topographic feature during space resolved experiments. An Arduino Uno microcontroller board (Arduino, Italy) attached to a custom designed potentiostat board, previously described in the literature, was used for all electrochemical measurements.¹⁹⁴ The simple and flexible design (on both hardware and software) allowed for the implementation of multiple electrochemical techniques

including space-resolved measurements. A diagram of the analog part of the potentiostat circuit can be found in Figure A2.1. Although lacking auto current range, the potentiostat current limits could be set to an adequate value by changing the feedback and bias resistors (R_6 and R_5 , respectively, in Figure A2.1) in the transimpedance amplifier (current to voltage converter, Figure A2.1C). In the equipment built and used throughout the experiments portrayed on this manuscript this was done by changing a small custom built circuit board (named “current shields”, See bellow) that attaches to the top of the potentiostat. The implications of the absence of such feature on space resolved electrochemical measurements will be discussed later in the paper. More details regarding the potentiostat operation limits (current and voltage compliance) and analog component values can be found bellow.

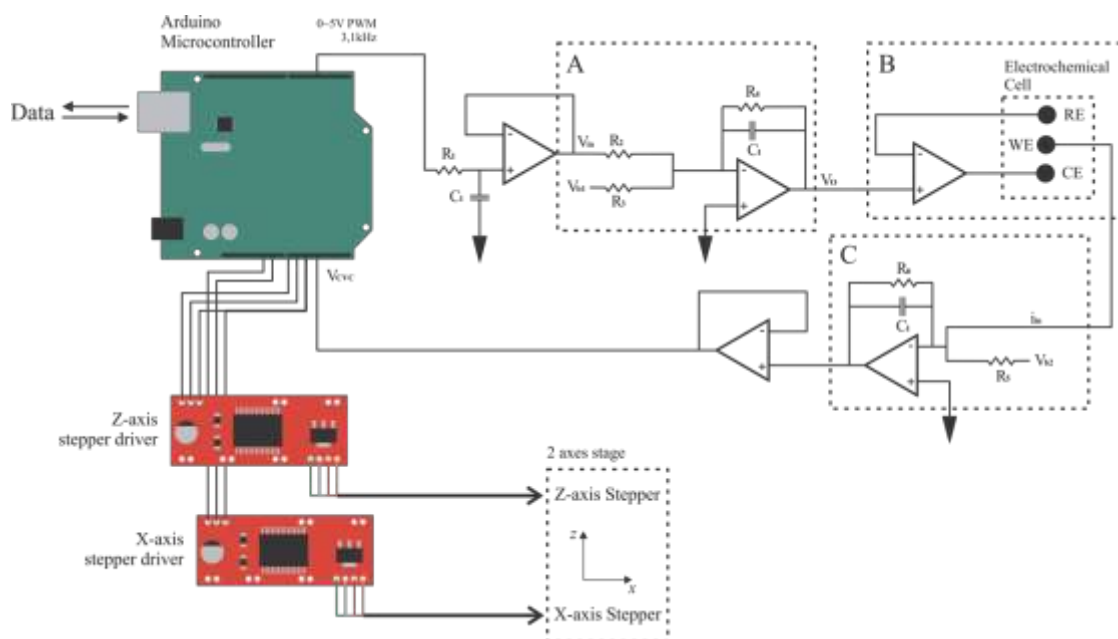


Figure A2.1. Diagram of the principal electronic components of the proposed EC-SPM setup showing the microcontroller board connected to the custom built potentiostat and to the “off-the-shelf” stepper controller boards used to fine control the linear stages during space-resolved electrochemical experiments. Highlighted are (A) the summing amplifier, (B) potential control circuit and electrochemical cell and (C) transimpedance amplifier of the custom built potentiostat.

A2.3.4 EC-SPM electronics construction

Although the electronic construction of the proposed EC-SPM setup could be made entirely using breadboards and jumper wires,¹⁹⁴ the device used to perform the experiments reported on the main manuscript was built using custom etched printed circuit boards (PCB). The PCB design was based on the Arduino Uno board and works as an “Arduino shield” making it easy to connect to an Arduino Uno board without the concern of connecting the pins wrong. Despite being more expensive than the breadboard construction, the PCB construction is sturdier and more reliable, increasing the quality of the experimental data acquired.

This type of construction allowed for the current range of the equipment to be quickly and easily changed by swapping a small PCB that is attached to the top of the potentiostat board. Those small PCBs, named “current shields” contain resistors R_5 and R_6 (figure A2.1) of the potentiostat circuit along with two other resistors (forming a voltage divider) responsible for signaling to the microcontroller board which current shield is set atop of the potentiostat. The relationship between R_5 and R_6 sets the current range of the equipment (Equation A2.1) while the other two resistors on the voltage divider set a specific voltage output that the microcontroller can read and identify the current shield used and change the current range on the software.

$$V_{CVC} = (i_{in} + \frac{V_{b2}}{R_5}) \times R_6 \quad (\text{Equation A2.1})$$

To calculate the resistors value, one should note that the Arduino Uno does not reads negative potentials, hence a bias potential (V_{b2}) should be applied Through R_5 in order to offset the current reading so the maximum values of current, positive and negative, lay between 0V and 5V. Figure A2.2 shows the equipment built using the custom etched PCB and the current shields used to set the current range.

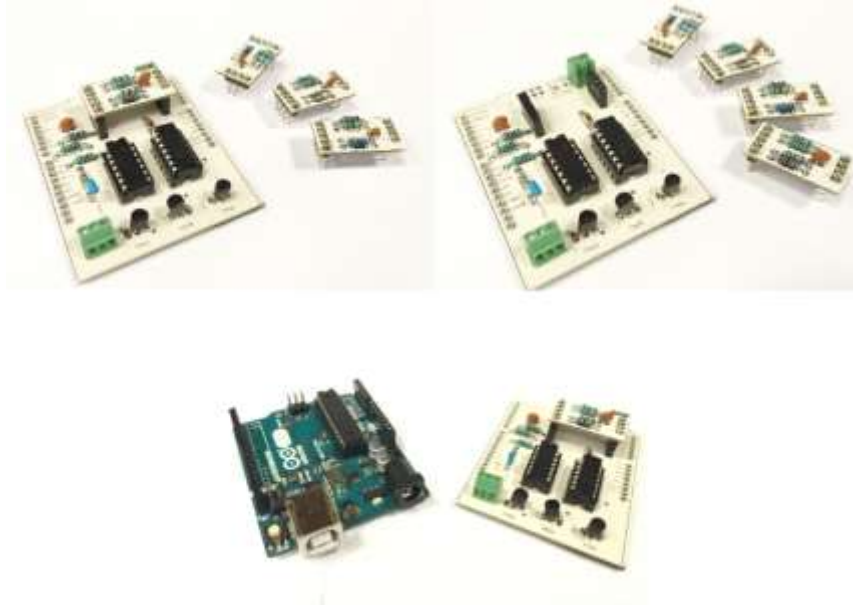


Figure A2.2. Multiple pictures of the proposed potentiostat design fabricated using a custom etched PCB showing the current shields (small PCBs) that allow for fast and easy change of the current limits.

The Arduino custom written sketch (Section SI-5 of the supporting information) recognizes the current shield being used and sets the appropriate current range so the correct current values can be recorded. The recognition of the shield comes from reading a voltage, produced by a voltage divider in the current shield, which should be unique for each current limit. This voltage divider is formed by two resistors, labeled $5V$ and GND (for ground) on the current shield (figure A2.3), and for the sketch presented on section SI-5, the values of those resistor together with resistor R_5 and R_6 , (named $Bias$ and FB respectively on the current shield, Figure A2.3) and the current limits can be seen on Table A2.1.

Potentiostat shield Current shield

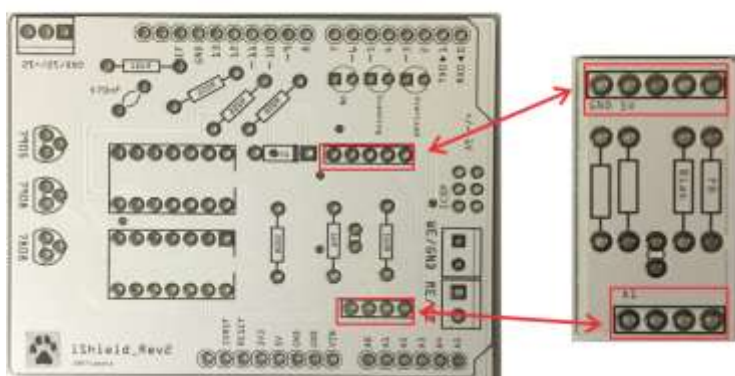


Figure A2.3. Photos of the potentiostat shield and current shield PCBs with component labels without any component solder. Red rectangles correspond to the connection site between the two shields.

Table A2.1. Resistance values for R_5 , R_6 , and voltage divider resistors and the resulting voltage divider voltage for different current limits. Values are the expected on the Arduino sketch on Section SI-5.

Current Limit (μA)	FB resistance/ R_6 (Ω)	Bias resistance/ R_5 (Ω)	R to GND (Ω)	R to 5V (Ω)	Voltage (V)	10bit ADC
200	12k	24k	10k	0k	0	0
100	24k	50k	24k	12k	1,6667	341
50	50k	100k	10k	10k	2,5	512
0,5	5M	10M	0	10k	5	1023

PCB layout files. Layout files (.fzz) for producing custom PCB potentiostat and current shield (Figure A2.3) are available free of charge via the Internet at <http://pubs.acs.org>.

The layout files can be used for production or open modified on a PCB design software (Fritzing is a good free alternative). The layout and routing of the tracks were made in a “functional” manner and are not optimum, use of the layouts should be made at the readers own discretion.

A2.3.5 Potentiostat specifications

The potentiostat used to perform all experiments presented on the main manuscript was custom design and built according to experimental needs. Limits of operation (current limits, voltage compliance and maximum scan rate) and component values follow. More detailed information can be found elsewhere (see Appendix I).¹⁹⁴

Table A2.2. Current, voltage and scan rate limits for the potentiostat used during the experiments performed in the main manuscript.

	Min.	Max.
Potential (V)	-1	1
Current (μA)	-0.5	0.5
Voltage compliance (V)	-5	5
Scan rate (Vs^{-1})		0.780

Table A2.3. Component values used during the electrochemical experiments on the main manuscript. Components are labelled as on Figure A2.1.

Component label on Figure S1	Component Value
<i>R1</i>	<i>10kΩ</i>
<i>R2</i>	<i>510Ω</i>
<i>R3</i>	<i>1kΩ</i>
<i>R4</i>	<i>200Ω</i>
<i>R5</i>	<i>10MΩ</i>
<i>R6</i>	<i>5MΩ</i>
<i>C1</i>	<i>470nF</i>
<i>C2</i>	<i>100nF</i>

A2.3.6 EC-SPM mechanical construction

The mechanical part of the proposed EC-SPM is comprised of the linear stages used in each one of the axis of movement which are mostly 3D printed. Figure A2.4 shows different views of the fully assembled linear stages used during the experiments reported on the main manuscript. 3D files (.stl) for the linear stages and electrode holder can be found on section SI-1 of the supporting information.



Figure A2.4. Pictures of two 3D printed linear stages fully assembled showing the placement of the electrochemical cell and the 3D printed UME holder.

A2.3.7 Tip positioning control

Tip positioning during the SECM experiments was achieved through 3D printed linear stages, one for each axis of movement, powered by “off-the-shelf” nema 17 stepper motors (Figure A2.4). Precise motor control was achieved through EasyDriver (Brian Schmalz and Sparkfun) stepper motor drive boards (one for each axis) connected to and controlled by the Arduino Uno microcontroller, as shown in Figure A2.1. The Linear stages were fabricated using both “off-the-shelf” and 3D printed parts. The stage body, consisting of a moving platform and a fixed base, was 3D printed. The linear motion of the stages was performed by a nema 17 stepper motor attached to the stage

body and connected to a M5 fine threaded rod through a 3D printed motor coupler. The moving platform of the stage couples to the threaded rod using a M5 nut. With a nominal thread pitch of 500 μm per revolution, advancing the rod by one full rotation would advance the stage by 500 μm . Without micro-stepping the motor, the theoretical resolution of the fabricated stages was calculated to be 2.5 μm . A representation of the individual parts and the whole assembly of the stage can be seen in Figure A2.5.

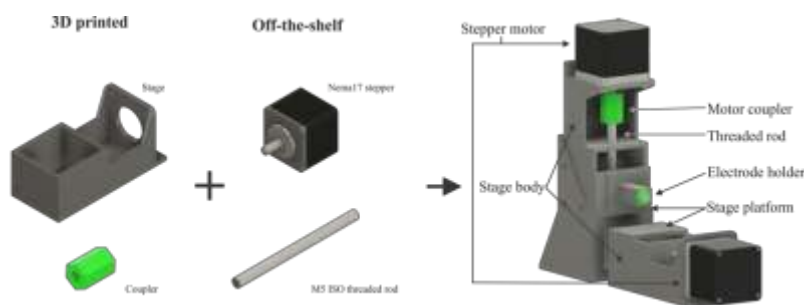


Figure A2.5. Exploded and assemble views of the linear stages used during SECM experiments showing both the 3D printed and “off-the-shelf” parts. Assembled view shows the 2-axes setup used during the SECM experiments.

A2.3.8 Software

The proposed equipment runs a custom Arduino program (also known as a Sketch) that allows the user to input experimental parameters and receive data via a serial terminal window on a computer connected to the Arduino board. The flexibility of the custom sketch allows for multiple electrochemical techniques and scanning techniques (line scan, array scan, and hopping mode) to be implemented quickly. It also allows for the user to develop new techniques and procedures, and to integrate the custom-built EC-SPM setup to different hardware or software. More information on the Arduino sketch can be found on Section SI-5 of the supporting information.

A2.4 Results

A2.4.1 Electrochemical measurements using microelectrodes

Although the simple and flexible design of the custom built potentiostat enables multiple electrochemical techniques to be easily performed in an affordable equipment, some of its characteristics can be unfavorable for performing space-resolved electrochemical experiments, being the lack of auto ranging for the current range the most concerning one. Despite providing an interesting opportunity (especially for teaching purposes) for exploring current amplification (current following/current-to-voltage conversion) and the influence of the current follower time constant when monitoring fast events,²⁹ the lack of such feature is detrimental for performing SECM experiments where an increase in tip current, compared to bulk values, is observed when the tip approaches the substrate, such as in Substrate-Generation/Tip-Collection experiments and when the “positive feedback” phenomena is observed.^{4,124,125} Hence, SECM experiments where the tip approaches towards an insulator (hindered diffusion) are better suited and thus have been carried out in the experiments depicted in the results.

Another concern that should be addressed when using the proposed potentiostat for performing electrochemical experiments using microelectrodes is the current resolution of the circuit. As the equipment is based on a microcontroller board that has an analog-to-digital (ADC) converter of 10 bits, it can only resolve 1024 discrete values of current over its full current range.¹⁹⁴ The electric noise recorded by the proposed equipment, intrinsic of such a simple electronic design, together with the fact that the faradaic currents recorded at microelectrodes are usually relatively low (due to its small electroactive area), require the use of concentrated solutions of redox mediator during the SECM experiments so that the recorded current at the tip (when properly biased) can

meet the current resolution of the equipment. Figure A2.6A shows the recorded current in a cyclic voltammetry experiment performed at a 15 μm platinum UME at the bulk of a 200 mmol.L^{-1} potassium ferricyanide solution where the distinct sigmoidal profile (limiting current) can be seen.

A2.4.2 Space resolved electrochemical measurements

To illustrate the capabilities of the proposed equipment to perform SECM experiments, an insulating substrate (silicon wafer) was positioned at the bottom of an electrochemical cell. The electrochemical cell, filled with the potassium ferricyanide solution, was placed over one of the 3D printed linear stages making for one of the axes of movement, the x-axis (parallel to the substrate plane). The other stage was positioned at 90 degrees from the x-axis forming the second axis of movement, the z-axis (perpendicular to the substrate plane). With the UME attached to the z-axis stage and biased at a potential where ferricyanide reduces at diffusion-limiting conditions, the electrode was approached towards the substrate while the reduction current was recorded. The resulting normalized tip current *vs.* normalized distance plot (approach curve) can be seen in Figure A2.6B. As can be seen, the expected profile of an approach curve over an insulating substrate (decrease of the SECM tip current with a decrease in tip/substrate separation) is observed. The experiment was performed in both directions, approaching to and retracting from the substrate, with both curves superimposing, meaning that there is a minimal amount of backlash on the linear stages.

Even with a minimal amount of backlash, the built linear stages might still suffer from some degree of inaccuracy in their position during displacement. This is especially concerning in the proposed system as it relies on an open-loop design for the positioning system, meaning that there is no positional feedback for the stepper

controller board. One can easily check for positional inaccuracy on the linear stages by fitting the experimental data obtained during the approach curves to the analytical approximation for the hindered diffusion.¹⁹⁶ Although a nice fit between the experimental and theoretical data can be seen in figure A2.6B, it was only obtained by using a factor of two on the amount displaced by each step of the approach curve. This means that whatever displacement step value is set in the software and sent to the stepper control board turns doubled by the linear stage. This can be due to a number of reasons, the most likely being the loose tolerance on the threaded rod pitch as the stages relies on simple “off-the-shelf” rods and the lack of a closed loop control on the steppers position. Also, to increase spatial resolution, a micro-stepping procedure was used on the stepper controller board, which can affect the stepper motor torque and accuracy. Although those are the most obvious sources it is more likely that a combination of factors contributed to the positional inaccuracy. As this inaccuracy remained consistent during all experiments a quick solution would be to treat the data using the correction factor (obtained through fitting the approach curve experimental data to the theory) on the displacement values or embed this correction value on the equipment software to correct the linear stages displacement values.

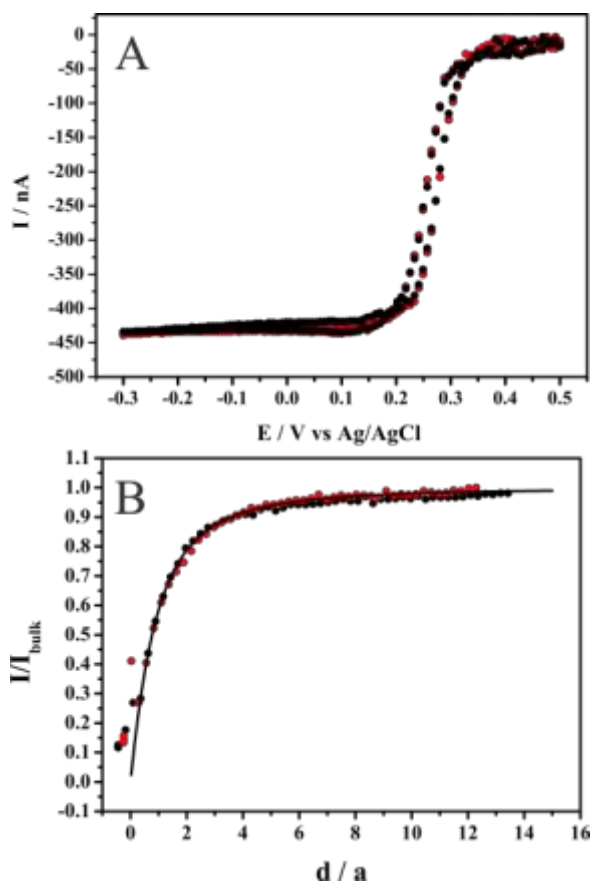


Figure A2.6. (A) Cyclic voltammograms recorded using the proposed equipment. Red and black dots represent two different cycles, before and after the approach curves. Scan rate = $50 \text{ mV}\cdot\text{s}^{-1}$ (B) Normalized approach curve recorded over an insulating substrate. Black dots: approaching the substrate. Red dots: retracting from the substrate. Black line: theoretical curve. $E_{\text{tip}} = -0.2\text{V}$. Step = $2 \mu\text{m}$. All experiments performed in $200 \text{ mmol}\cdot\text{L}^{-1}$ potassium ferricyanide solution using a $15 \mu\text{m}$ diameter platinum UME as the working electrode and a Ag/AgCl QRCE.

To further investigate the capability of the proposed equipment to perform as a SECM equipment, an insulator substrate (silicon wafer) containing a topographical feature (a step made of a polyimide tape layer) was placed at the bottom of the electrochemical cell filled with a $50 \text{ mmol}\cdot\text{L}^{-1}$ methyl viologen (MV) solution. The platinum UME, positioned over the polyimide tape step and biased at a potential where MV reduces at diffusion-limiting conditions, was approached towards the substrate until a tip/substrate separation of $15 \mu\text{m}$. Using the x-axis stage, the UME was scanned at a

constant height over the polyimide step edge while the MV reduction current was recorded. The line scan was repeatedly performed in both directions, up and down the polyimide step (Figure A2.7A). The resulting line scans can be seen in Figure A2.7B (scan up the step) and Figure A2.7C (scan down the step).

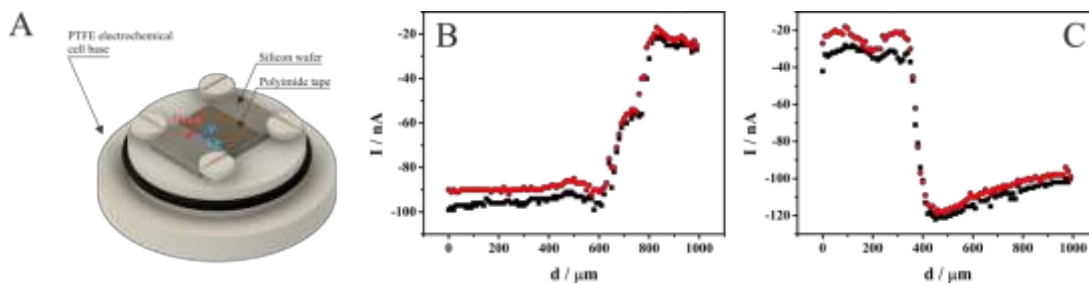


Figure A2.7. (A) Schematic representation of the substrate (attached to the electrochemical cell bottom) showing the insulating substrate and the polyimide tape step. Arrows indicate the scanning direction over the step edge. (B) Line scans performed up to the step edge. (C) Line scans performed down the step edge. Scans were performed in duplicate (red and black dots) using a 50 mmolL^{-1} MV solution. $E_{\text{tip}} = -0.9 \text{ V}$, Step = $10 \mu\text{m}$, Scan speed = $10 \mu\text{ms}^{-1}$.

As expected for a constant height SECM scan over an insulator substrate, the reduction current recorded at the SECM tip (platinum UME) decreases when the electrode scans over the step edge as the tip/separation decreases due to the height of the polyimide tape, hindering the diffusion of MV towards the tip. The difference between the line scans profile when performed up and down the step edge, with the change in the reduction current being more gradual when scanning up the step, results from the tip scan rate employed during the experiment. Even at moderate tip scan rates, such as the one used during the experiments here portrayed, true steady state behavior at the scanning tip (*i.e.* diffusion limited current) is hardly achievable, resulting in the current asymmetry observed in Figure A2.7 (B and c).^{197–199} Although this asymmetry can be mitigated by employing much slower tip scan rates, precise tailored to the tip and substrate geometry, this “edge effect” is always presented, at different extensions, on

SECM scans, even on constant distance experiments.^{199,200} This decrease in current, due to the perturbation of the UME diffusion layer by the substrate, means that the SECM tip “senses” the topography of the substrate, a well known phenomenon that poses a challenge when trying to deconvolve electrochemical and topographical information in a constant height SECM experiment.^{14,16,21,59,61,72,201} Nevertheless, usable information can still be acquired with the proposed equipment through constant height SECM experiments, especially over substrates that are mostly flat.

SECM experiments can also be performed as array scans by moving the tip along more than one axis while acquiring electrochemical information over a plane. This array scan method brings an extra dimension of electrochemical information, allowing one to easily visualize the distribution of such information along the space by creating electrochemical images of the scanned area. Although array scans are usually performed in a plane parallel to the substrate, they can also be performed perpendicular to the substrate plane providing electrochemical information at different tip/substrate separations over a line along the substrate. This can be performed by approaching the SECM tip from bulk to substrate at different locations along a line while recording the current at the UME, effectively recording an approach curve at multiple locations over the substrate. As the electrode is always brought to the bulk solution before approaching a different location over the substrate, the recorded currents could be normalized against the bulk values for every location along the line thus eliminating any influence of concentration changes with time on the recorded information.^{10,12,202} Those “self-referencing” scanning approaches are found in the literature as hopping mode SECM (“hopping”, an allusion to the electrode movement) or 4D SECM and,^{202,203} despite being powerful, are quite simple to implement on the proposed equipment due to the flexibility in hardware and software. Figure A2.8B shows the resulting current map of a

“hopping” array scan performed over a stepped substrate (same as before) using the custom built EC-SPM equipment and MV as a redox mediator.

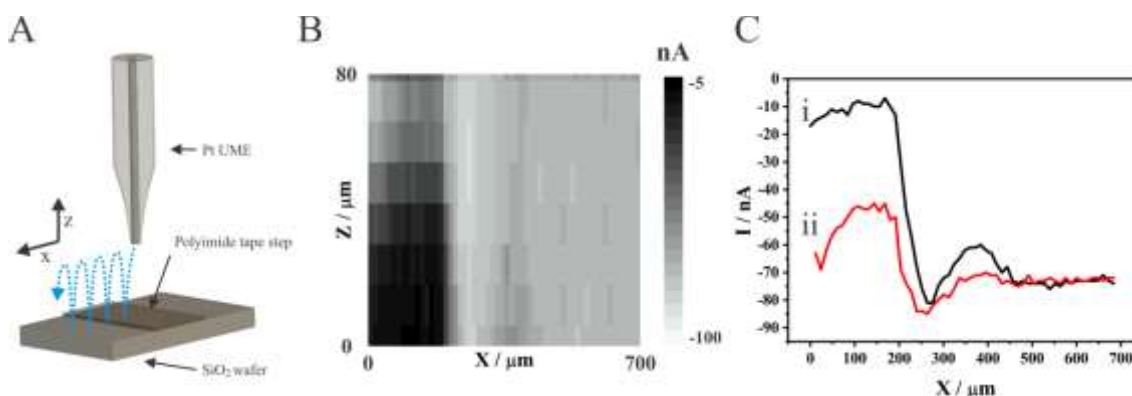


Figure A2.8. (A) Representation of the electrode “hopping” path (blue dotted line) across the substrate step edge. (B) Resulting current map obtained during the array scan over the xz plane. (C) Line scans across the substrate step edge recovered from the current map data at two distinct tip heights (tip separation from the polyimide step), (i) $12\ \mu\text{m}$ and (ii) $24\ \mu\text{m}$. $E_{\text{tip}} = -0.9\text{V}$, Pixel size = $12\ \mu\text{m} \times 12\ \mu\text{m}$, Scan speed = $12\ \mu\text{ms}^{-1}$.

By inspecting the current map on Figure A2.8B, one can note a region of lower current at the bottom left corner. This region corresponds to the location of the stepped feature (polyimide tape) on the substrate, where the tip is near the substrate; hence, the diffusion of material towards the electrode is hindered resulting in a smaller recorded current. When the electrode is scanned off the stepped feature, a sharp increase in current is recorded as the diffusion of material towards the electrode is no longer hindered by the substrate. As the polyimide tape has a relatively large thickness (of the order of hundreds of micrometers), no significant reduction in the recorded current is noticed off the stepped feature with the z -axis scan range used. As this array scan is comprised of data points (pixels on the image) on the xz plane, line scans over the stepped feature, similar to those in figure A2.7, can be easily reconstructed for different tip/substrate separations. A set of two line scans at different tip heights (tip separation from the polyimide step) reconstructed from the data set of the array scan can be seen in

Figure A2.8C. A more significant reduction in recorded current is clearly noticed when the electrode is scanned across the stepped feature at the line scan at a smaller tip height (line i) when compared to the line scan at a larger tip height (line ii). For both line scans (i and ii), no appreciable difference is observed when the electrode is off the stepped feature. Although simple, the results obtained on the hopping scan are in accordance with the expected for the hindered diffusion phenomena and prove the capabilities of the proposed SECM setup for performing such technique. A more suitable application for this scanning method would be to investigate the concentration profile of an electroactive species over an electroactive substrate. Unfortunately, this would require, as discussed previously, a bi-potentiostat and/or auto ranging on the current range, which are lacked by the current design of the proposed setup.

Nevertheless, if one desires, the flexible design of the proposed equipment should allow for an easy implementation of such features. The addition of a third axis of movement (y-axis) would also be straight forward and would add little to the equipment final cost (Section SI-6 of the supporting information). It is worth mentioning that, as a flexible developing platform, other EC-SPM techniques, such as Scanning Ion Conductance Microscopy (SICM) and Scanning Electrochemical Cell Microscopy (SECCM), can be implemented on the proposed equipment with little effort and additional cost.

A2.5 Conclusion

By using 3D printed parts and readily available microcontroller boards, together with a few “off-the-shelf” electronic and mechanical components, a fully functional EC-SPM equipment capable of performing multiple space resolved electrochemical techniques with an adequate spatial resolution was built. The designed equipment was able to record cyclic voltammetry experiments on UME and a series of SECM experiments such as approach curves, line scans and array scans (on hopping mode) were performed, delivering results in agreement with theory and previously reports in the literature. Even though results could only be acquired in situations where hindered diffusion was observed due to the instrumental limitation on the design, it is demonstrated that the proposed equipment can perform simple SECM experiments, thus being a powerful platform for teaching not only the principles behind SECM operation but also basic electrochemical principles such as mass transport. Despite its simplicity, the flexible design and the low cost of the materials (less than \$100.00, Section SI-6 of the supporting information) can make the proposed equipment an attractive platform for developing high-end EC-SPM rigs, especially in places where budget or supply of specialized equipment is at a premium.

A2.6 Acknowledgements

The research upon which this article was based was supported by Conselho Nacional de Desenvolvimento Científico e Tecnológico (CNPq: grant number 48383/2012-2) to which the author is very grateful for the financial support. The author thanks Ms. Carla Santana Santos for helping with the UME fabrication and for the helpful discussions along the development of this manuscript. The author also would like to thanks Dr. Mauro Bertotti for providing support with infrastructure.

Summary

SEPM techniques are powerful tools for investigating, in a space resolved manner, a wide variety of interfacial reactions and interface properties throughout the use of electrochemical probes. Despite its limitation with topography-rich substrates, SECM is among the most versatile SEPM techniques being capable of investigating a broad spectrum of electrochemical species/phenomenon. This versatility arises from the intrinsic chemo-selectivity of electrodes (which are used as SECM probes) achieved by biasing the probe at appropriated potentials. This selectivity can be easily tailored and/or enhanced by simple electrode modifications. SICM, on the other hand, lacks (at a certain extent) selectivity and SICM probes can be employed, as a chemical sensor, on a very narrow range of chemical species/phenomenon. Although insensitive and unselective, SICM strives in imaging topography-rich substrates, especially in soft substrates/interfaces where it can outperform well established topography imaging SPM techniques, such as AFM. The use of multifunctional electrochemical probes, capable of acquiring multiple space resolved electrochemical information, greatly increases the versatility of SEPM and grants those techniques higher spatial resolution and acquired information density than any other bulk electrochemical measurement technique. Employing multifunctional electrochemical probes in SEPM experiments allows the hybridization of different techniques in the same electrochemical probe, enabling experiments relying on the combination of the strengths of those techniques to be performed. This is especially advantageous for performing constant separation SECM experiments where a SICM probe can be used as a substrate topography sensor, allowing the SECM probe to acquire electrochemical information independent of the substrate topography, overcoming the biggest limitation of SECM, the entanglement of electrochemical and topographical information.

Multifunctional probes are particularly useful for investigating complex systems where, by acquiring multiple electrochemical information, different set of data (monitoring of different species) can be used to help elucidate such systems. They can even be employed to investigate systems where a non-electroactive species takes part by indirect measuring such species throughout a generation/collection system. Multifunctional electrochemical probes act upon increasing the density of electrochemical information acquired and also, indirectly by enabling a precise substrate topography feedback, in increasing the spatial resolution of SEPM techniques. This is achieved by allowing the precise positioning and maintenance of an electrochemical probe at close proximity to a substrate/interface, which is essential for employing small (nanometer sized) electrochemical probes in electrochemical imaging experiments.

Nevertheless, most SEPM lags other SPM techniques regarding its spatial resolution, despite outputting a higher density of information. This resolution gap needs to be bridged and, in the simplest approach, a higher spatial resolution can be achieved by significantly decreasing the size of the electrochemical probes employed. In this sense, pipette based, pyrolytic carbon electrodes strive as a fast and simple alternative capable of yielding probes with just a few 10s of nanometers in size. These probes can also be used as multifunctional electrochemical probes by simply using a multi-barrel pipette as the base of the electrode and selectively depositing carbon in a few (for a SECM/SICM probe) or in all barrels (for SECM/SECM probe). Although simple, the fabrication of those probes can become challenging when trying to achieve nanometer sized probes with the most common fabrication procedure yielding low reproducibility and often recessed electrodic surfaces. To overcome those issues, a more precise and controlled fabrication method was needed which, despite successfully addressing the tip fabrication limitations, kept the whole process simple. Decreasing the tip size is also a

problem for proper characterization and manipulation of those electrochemical probes which, despite the macroscopic body, can have critical dimensions in the order of a few 10s of nanometers. As mentioned in the introduction (see Section 1.4), increasing the spatial resolution of SEPM is a never-ending pursuit for **the** smallest tip. Or better saying, for the smallest multifunctional electrochemical probe. The smallest tip has yet to be produced and its pursuit should be a tirelessly one backed by an almost naïve creative and innovative though which is necessary when breaking new scientific ground by pushing a (tiny) bit further the knowledge envelope.

CURRICULUM VITAE OF GABRIEL NEGRÃO MELONI

Nationality: Brazilian

Address of residence

Rua Votuporanga, 28, São Paulo, Brasil, 01256-000

Phone: 55 11 982024643

Email: gabrielnmeloni@gmail.com

Education

2012- Expected: September 2017: **PhD, Chemistry**, Universidade de São Paulo

Thesis: “Fabrication and characterization of multifunctional probes for Scanning Electrochemical Microscopy and their applications”

Supervisor: Professor Mauro Bertotti

Highlights:

- **First Brazilian** thesis involving **multifunctional electrochemical probes** for imaging applications in SECM experiments.
- Applied **multiple** electrochemical techniques on **single SEPM** probe for increased density of information and **topography-free** electrochemical measurements.
- Developed **new** and **innovative tools** and **techniques** for fabricating and characterizing nanometer sized multifunctional electrochemical probes.
- Led the work by **designing** and **performing** the experiments **independently** and interpreting the results with **minimal assistance**.
- Independently prepared **2 high quality journal articles** published as the **corresponding** and **only author**.
- One publication (as the only author) is among the **20 most read** publications of the last 12 months of *J. Chem. Ed.* With more than **5000 downloads** worldwide.
- **Independently** prepared **2 high quality journal articles** with results collected over his doctoral candidature.
- Prepared and/or participated in another **6 high quality journal articles** with results collected over his doctoral candidature and also from **collaborations with multiple research groups** in Brazil and elsewhere in the world.
- Spent **1 year** as a visiting PhD student in the UK, resulting in the publication of **1 high quality journal article**.
- Participated on the organizing committee of **3 international scientific events**.

2007-2012: **BSc, Chemistry**, Universidade de São Paulo

Language skills

Portuguese: *Native speaker*

English: *CEFR-C1*

Spanish: *Working knowledge*

Research Interest

Development and application of new electrochemical techniques and electrodes for investigating processes and heterogeneity at interfaces with high spatial resolution (nanometer).

Development and fabrication of low cost and accessible electrochemical instrumentation for teaching and research.

Research Experience

Visiting Graduate Student

Feb. 2015 – Feb 2016 (12 months): *Warwick Electrochemistry and Interfaces group, University of Warwick*

Supervisor: Professor Patrick R. Unwin

- Performed experiments as part of my PhD thesis exploring coupling Scanning Electrochemical Microscopy/ Scanning Ion Conductance Microscopy (SECM/SICM) for investigating surface topography and activity.
- Contributed to multiple research projects in the development of new Electrochemical Scanned Probe Techniques (EC-SPM), leading to a publication in an international journal (*Anal. Chem.*).
- Collaborated and coordinated with faculty, staff scientists, and fellow graduate students in the organization of **two scientific meetings** (2015 Midlands Electrochemistry Group (MEG) meeting and 2016 Warwick-Brazil meeting; *see below*).

Visiting Undergraduate Student

Jan. 2010 – Mar. 2010: *Dipartimento di Scienze Molecolari e Nanosistemi, Università Ca'Foscari di Venezia*

Supervisor: Professor Salvatore Daniele

- Initiated this short secondment to Italy and performed Scanning Electrochemical Microscopy (SECM) experiments detecting soluble copper species in alkaline medium.
- Collaborated with staff scientist and graduate students during the development of the research project acquiring experience in the use and principals of operations of the SECM, which was crucial for the implementation of the technique back in Brazil, at the end of the visiting period.
- Learned to fabricate SECM probes using glass capillary and capillary pullers which was **transferred to the students back to Brazil**, enabling the mass fabrication of SECM tips, crucial for the implementation of the technique in Prof. Bertotti group in Brazil.

Undergraduate Research Project

2008 – 2011: *Laboratório de Sensores Eletroquímicos e Métodos eletroatalíticos, Universidade de São Paulo*

Supervisor: Professor Mauro Bertotti

- Development and fabrication of disposable integrated copper electrodes by chemical etching.

- Simplified previous designs by employing a quasi-reference silver ink based electrode and a Cu/Cu working and counter electrode.
- Prompted the production of highly reproducible integrated electrodes by using computer assisted design of the etching mask which also allowed batch production.
- Investigation of the electrocatalytic cycle between soluble copper species and ethanol in alkaline medium.
- Performed experiments towards the detection of ethanol in exhaled air using disposable integrated copper electrodes.
- Participated in experimental demonstrations of electrochemistry techniques at the laboratory during electrochemistry classes for graduated students.
- Helped to setup-up and run the first SECM at the Universidade de São Paulo.
- Developed protocols for SECM electrode fabrication and performed training sessions to transfer the skill to lab colleagues.

Teaching experience

Dec. 2013: *Demonstrator, São Paulo School of Advanced Sciences on Electrochemistry, Energy Conversion, and Storage (SPASECS).*

Department of Chemistry, Universidade de São Paulo

- Developed and supervised laboratory activities on electrochemical techniques for graduate students from around the world (80 students from >25 countries of all over the globe).
- Developed and supervised laboratory activities specific for Scanning Electrochemical Microscopy together with Prof. Guy Denualt from the University of Southampton.
- Assisted the invited professors of the University of Southampton delegation in laboratory activities.

2013 - 2014: *Teaching Assistant, Electrochemistry and Electroanalytical techniques.*

Department of Chemistry, Universidade de São Paulo

- Prepared laboratory activities focusing on basic electrochemical techniques and their application in chemical analysis for 2nd year Chemistry undergraduates.

Jul. 2012 – Nov. 2012: *Teaching Assistant, Quantitative and Qualitative Analytical Chemistry.*

Department of Chemistry, Universidade de São Paulo

- Supervised laboratory activities in fundamental Quantitative and Qualitative Analytical techniques for 2nd year Chemistry undergraduates.

Feb. 2009 - Jul. 2009: *Teaching Assistant, Quantitative and Qualitative Analytical Chemistry.*

Department of Chemistry, Universidade de São Paulo

- Supervised laboratory activities in fundamental Quantitative and Qualitative Analytical techniques for 1st year Oceanography undergraduates.

2008 - 2016: *Demonstrator, School of Electrochemistry.*

Department of Chemistry, Universidade de São Paulo

- Developed and supervised laboratory activities in electrochemical techniques for graduate students from around the world.
- Developed in 2010 a SECM experimental activity that has since been part of the electrochemistry school.

Academic and Administrative experience

Jan. 2016 – Feb. 2016: *Organization committee for the 2016 Warwick-Brazil meeting.*

Department of Chemistry, University of Warwick

- Responsible for organizing transfer and accommodation for the Brazilian delegation.
- Responsible for the budgeting and timetabling.
- Liaison for the Brazilian delegation.

Jun. 2015: *Organization committee of the Midlands Electrochemistry group meeting (MEG)*

Department of Chemistry, University of Warwick

- Responsible for negotiating and securing financial support from Industry partners.
- Responsible for keeping finances up to date.
- Collaborated with fellow graduate students from the organization committee.

2013 - 2014: *Graduate student representative in the Graduation Program Committee.*

Department of Chemistry, Universidade de São Paulo

- Actively participated from the day-by-day decision making of the Graduation Program Committee been the liaison of the graduate students with the Graduate Program Coordinators.

Dec. 2013: *Staff, São Paulo School of Advanced Sciences on Electrochemistry, Energy Conversion, and Storage (SPASECS).*

Department of Chemistry, Universidade de São Paulo

- Helped the logistic transfer, arrival and departure of the attendees (>80, 40 non-Brazilian) of the 1st SPASECS.
- Liaison student for the Southampton delegation (Full professors and graduation students)

Dec. 2008 – Dec. 2009: *President of the Academic Sports Committee.*

Department of Chemistry, Universidade de São Paulo

- Coordinated the Academic Sports Committee during the academic year of 2009 organizing sport events, social meeting and interstate competitions for undergraduates and graduates Chemistry students.
- Administrated the Academic Sports Committee estate and finances.

2008 - 2016: *Staff, School of Electrochemistry.*

- Organized the logistic for accommodation and transfer, arrival and departure of the attendees of the São Paulo School of Electrochemistry.

Technical skills

Electrochemical methods:

Voltammetry, amperometry, potentiometry, pulse techniques and general electrochemical detection and electrode fabrication.

Electrochemical scanning probe techniques:

Scanning electrochemical microscopy (SECM), Shear force scanning electrochemical microscopy (SF-SECM), Scanning ion conductance microscopy (SICM) and tip fabrication.

Electron microscopy:

Scanning electron microscopy (SEM) and Transmission Scanning electron microscopy (T-SEM).

General fabrication:

Fabrication of electrodes and substrates by chemical etching and heat-transfer masks. Laser cutting and engraving. 3D printing by FDM method. μ PAD fabrication by wax printing.

Electronics:

Analog and digital electronics. Microcontrollers. Breadboard and custom designed Printed circuit board (PCB) construction.

Other skills

Programming: C++ and Arduino sketch.

Data treatment: Origin, Wolfram Mathematica, ImageJ.

Vector drawing: CorelDraw and InkScape.

3D design and drawing: 123D design, Autodesk Inventor and Autodesk Fusion 360.

Publications (*corresponding author)

*1 - **Meloni, G. N.** 3D printed and Microcontrolled: The one hundred dollars Scanning Electrochemical Microscope, *Anal. Chem.* **2017**, 89 (17), 8643-8649

*2 - **Meloni, G. N.**; Bertotti, M. 3D printing scanning electron microscopy sample holders: A quick and cost effective alternative for custom holder fabrication, *PlosOne* **2017**, 12 (2017) e0182000

3 - Lima, A. R.; Lima, A. S.; **Meloni, G. N.**; Santos, C. S.; Bertotti, M. Enhancing the oxygen reduction reaction rate in $\text{La}_{0.6}\text{M}_{0.4}\text{Ni}_{0.6}\text{Cu}_{0.4}\text{O}_3$ (M = Ag, Ba, Ce) perovskite oxides by combining synergistic and structural effects: correlation between crystallographic phase and catalytic activity, *Electrocatalysis* **2017**, *submitted*.

4 - Carneiro, J. F.; Trevelin, L. C.; Lima, A. S.; **Meloni, G. N.**; Bertotti, M.; Hammer, P.; Bertazzoli, R.; Lanza, M. R. V. Synthesis and Characterization of ZrO_2/C as Electrocatalyst for Oxygen Reduction to H_2O_2 , *Electrocatalysis* **2017**, 8 (3), 189–195.

(Citations: 1)

5 - **Meloni, G. N.**; Bertotti, M. Ring-disc Microelectrodes towards Glutathione Electrochemical Detection, *Electroanalysis* **2017**, 29 (3), 787–793.

*6 - **Meloni, G. N.** Building a Microcontroller Based Potentiostat: A Inexpensive and Versatile Platform for Teaching Electrochemistry and Instrumentation, *J. Chem. Educ.* **2016**, 93 (7), 1320–1322.

(Citations: 6 – Downloads: 5500)

7 - Momotenko, D.; McKelvey, K.; Kang, M.; **Meloni, G. N.**; Unwin, P. R. Simultaneous Interfacial Reactivity and Topography Mapping with Scanning Ion Conductance Microscopy, *Anal. Chem.* **2016**, 88 (5), 2838–2846.

(Citations: 12)

8 - Bueno, L.; **Meloni, G. N.**; Reddy, S. M.; Paixão, T. R. L. C. Use of plastic-based analytical device, smartphone and chemometric tools to discriminate amines, *RSC Adv.* **2015**, 5 (26), 20148–20154.

(Citations:9)

9 - Salles, M. O.; **Meloni, G. N.**; de Araujo, W. R.; Paixão, T. R. L. C. Explosive colorimetric discrimination using a smartphone, paper device and chemometrical approach, *Anal. Methods* **2014**, 6 (7), 2047–2052. (**Back cover of the edition**)

(Citations: 41)

10 - Lima, A. S.; **Meloni, G. N.**; Bertotti, M. Determination of paracetamol in presence of ascorbic acid in pharmaceutical products by scanning electrochemical microscopy, *Electroanalysis* **2013**, 25 (6), 1395–1399.

(Citations: 3)

Conference

Oral presentatio:

1 - **Meloni, G. N.** Cheap and accessible electrochemistry: modern fabrication tools towards electrochemistry instrumentation. *International Society of electrochemistry Anual meeting*, **2017**.

Poster presentation:

1 - **Meloni, G. N.** Microcontroled and 3D printed: Low cost space resolved electrochemistry, *Pittsburg Conference & Expo.* **2017**.

2 - **Meloni, G. N.** ; Lima, A. S; Bertotti, M. A study on the use of SECM for electrochemical depletion of ascorbate and selective determination of paracetamol in pharmaceutical formulations. *Pittsburg Conference & Expo.* **2013**.

3 - **Meloni, G. N.**; Salles, M. O. ; Da Costa, E. T. ; Araujo, W. R. ; Paixao, T. R. L. C. . . Development of RGB extraction values software and chamber case to collect information of electronic colorimetric tongues. *Pittsburg Conference & Expo.* **2013**.

4 - **Meloni, G. N.**; Bertotti, M. ; Daniele, S. . Estudo Da Solubilidade E Estabilidade Do Cu (III) Em Meio Alcalino Na Presença De Etanol Utilizando SECM.. *XVIII Simpósio Brasileiro de Eletroquímica e Eletroanalítica*, **2011**.

5 - **Meloni, G. N.**; Paixao, T. R. L. C. ; Bertotti, M. . Fabricação de sensor eletroquímico portátil visando à detecção de etanol em ar exalado. *XVII Simpósio Brasileiro de Eletroquímica e Eletroanalítica*, **2009**.

Organization of scientific events

Jan. 2016 – Feb. 2016: *Organization committee for the 2016 Warwick-Brazil meeting.*

The Warwick-Brazil initiatives started in 2011 with its first meeting taking place at the Universidade de São Paulo, aiming to connect the two universities and their main electrochemistry groups and prompt world leading initiatives in electrochemistry and collaborations. During the first meeting, in Brazil, Gabriel had his first contact with Prof. Patrick Unwin and Prof. Julie Macpherson from the Chemistry Department and Prof. Mark Newton from the Physics Department. The second meeting took place in 2016 while Gabriel was a visiting PhD student at the *Warwick group*. Gabriel was tasked with being the liaison for the Brazilian delegation (3 Professors and 1 PDRA) arranging accommodation, transportation and arrival/departure schedule. Among the Gabriel's responsibilities was arranging and setting up the venue and the coffee-break amenities, and to coordinate with other postgraduate students the presentations (to a group of 50 people) and lab visits. The meeting was a great success and highly rewarding to Gabriel, as it gave him the opportunity to promote the same event that a few years later helped him on his career opportunities and networking. The experience also gave Gabriel valuable experience in **leadership, networking and scientific communication.**

Jun. 2015: *Organization committee of the Midlands Electrochemistry Group meeting (MEG)*

The Midlands Electrochemistry Group meetings are a series of annual meetings of the major electrochemistry groups from the UK Midlands with groups from University of Birmingham, University of Leicester, Loughborough University, University of Nottingham and University of Warwick. The Meeting is held at one of the participating universities. In 2015 the meeting was held at the University of Warwick and Gabriel, as he was a visiting student at the Warwick group by the time, was in the organizing committee. Gabriel took a leading role in the organization, being responsible for establishing sponsorship relations with industry partners and securing financial support for the event (**Metrohm UK, Alvatek, JB Cambria, Uniscan, Royal Society of Chemistry and International Society of Electrochemistry**). Gabriel was also involved in the venue organization for the talks, posters and coffee-break and lunch. The meeting was very successful and gave Gabriel valuable experience in **budgeting, leadership, networking with peer scientist and industrial partners, scientific communication.**

Dec. 2013: *Staff, São Paulo School of Advanced Sciences on Electrochemistry, Energy Conversion, and Storage (SPASECS).*

The São Paulo School of Advanced Sciences on Electrochemistry, Energy Conversion and Storage was the first truly international edition of the Electrochemistry School

which has been held at the Universidade de São Paulo yearly since 2006. The SPASECS was sponsored by the São Paulo Research Foundation and hosted 10 international professors and demonstrators (mostly from the University of Southampton, UK) and 80+ participants from more than 25 different countries. The participants had the opportunity to learn basic and advanced electrochemistry techniques from world leaders in the field and to use the full infrastructure provided by the Universidade de São Paulo. Gabriel was among the Brazilian staff of the organization committee and was responsible for liaising with the Southampton delegation, arranging the transportation from and to the airport and, together with Prof. Guy Denualt from Southampton, teaching the experimental activity on SECM. Gabriel also coordinated, with other staff, the organization and setup of all the practical activities. Gabriel was also the designated security office for all the laboratory activities. The school was a great success and extremely rewarding for Gabriel, who had the opportunity to greatly enlarge his **network, and demonstrate his scientific communication skills, management and organizational skills and leadership characteristics.**

Academic honors and prizes

- **2014:** Invited Back cover of *Analytical Methods* with the article “*Explosive colorimetric discrimination using a smartphone, paper device and chemometrical approach*”

References

- (1) Zoski, C. G. *J. Electrochem. Soc.* **2016**, *163* (4), H3088–H3100.
- (2) Polcari, D.; Dauphin-Ducharme, P.; Mauzeroll, J. *Chem. Rev.* **2016**, *116* (22), 13234–13278.
- (3) Amemiya, S.; Bard, A. J.; Fan, F.-R. F.; Mirkin, M. V.; Unwin, P. R. *Annu. Rev. Anal. Chem.* **2008**, *1* (1), 95–131.
- (4) Bard, A. J.; Fan, F. R. F.; Kwak, J.; Lev, O. *Anal. Chem.* **1989**, *61* (2), 132–138.
- (5) Hansma, P.; Drake, B.; Marti, O.; Gould, S.; Prater, C. *Science (80-.)*. **1989**, *243* (4891), 641–643.
- (6) Ebejer, N.; Schnippering, M.; Colburn, A. W.; Edwards, M. a.; Unwin, P. R. *Anal. Chem.* **2010**, *82* (22), 9141–9145.
- (7) Actis, P.; Tokar, S.; Clausmeyer, J.; Babakinejad, B.; Mikhaleva, S.; Cornut, R.; Takahashi, Y.; López Córdoba, A.; Novak, P.; Shevchuk, A. I.; Dougan, J. A.; Kazarian, S. G.; Gorelkin, P. V.; Erofeev, A. S.; Yaminsky, I. V.; Unwin, P. R.; Schuhmann, W.; Klenerman, D.; Rusakov, D. A.; Sviderskaya, E. V; Korchev, Y. E. *ACS Nano* **2014**, *8* (1), 875–884.
- (8) Takahashi, Y.; Shevchuk, A. I.; Novak, P.; Babakinejad, B.; Macpherson, J.; Unwin, P. R.; Shiku, H.; Gorelik, J.; Klenerman, D.; Korchev, Y. E.; Matsue, T. *Proc. Natl. Acad. Sci.* **2012**, *109* (29), 11540–11545.
- (9) O’Connell, M. A.; Wain, A. J. *Anal. Chem.* **2014**, *86* (24), 12100–12107.
- (10) Page, A.; Kang, M.; Armitstead, A.; Perry, D.; Unwin, P. R. *Anal. Chem.* **2017**, *89* (5), 3021–3028.
- (11) Bentley, C. L.; Kang, M.; Unwin, P. R. *J. Am. Chem. Soc.* **2016**, *138* (39), 12755–12758.
- (12) Perry, D.; Paulose Nadappuram, B.; Momotenko, D.; Voyias, P. D.; Page, A.; Tripathi, G.; Frenguelli, B. G.; Unwin, P. R. *J. Am. Chem. Soc.* **2016**, *138* (9), 3152–3160.
- (13) Güell, A. G.; Meadows, K. E.; Dudin, P. V.; Ebejer, N.; Macpherson, J. V.; Unwin, P. R. *Nano Lett.* **2014**, *14* (1), 220–224.
- (14) Kranz, C. *Analyst* **2014**, *139* (2), 336–352.
- (15) Oja, S. M.; Fan, Y.; Armstrong, C. M.; Defnet, P.; Zhang, B. *Anal. Chem.* **2016**, *88* (1), 414–430.
- (16) Takahashi, Y.; Shevchuk, A. I.; Novak, P.; Zhang, Y.; Ebejer, N.; Macpherson, J. V.; Unwin, P. R.; Pollard, A. J.; Roy, D.; Clifford, C. A.; Shiku, H.; Matsue, T.; Klenerman, D.; Korchev, Y. E. *Angew. Chemie Int. Ed.* **2011**, *50* (41), 9638–9642.
- (17) Şen, M.; Takahashi, Y.; Matsumae, Y.; Horiguchi, Y.; Kumatani, A.; Ino, K.;

- Shiku, H.; Matsue, T. *Anal. Chem.* **2015**, *87* (6), 3484–3489.
- (18) Morris, C. A.; Chen, C.-C.; Baker, L. A. *Analyst* **2012**, *137* (13), 2933–2938.
- (19) Momotenko, D.; McKelvey, K.; Kang, M.; Meloni, G. N.; Unwin, P. R. *Anal. Chem.* **2016**, *88* (5), 2838–2846.
- (20) Morton, K. C.; Morris, C. A.; Derylo, M. A.; Thakar, R.; Baker, L. A. *Anal. Chem.* **2011**, *83* (13), 5447–5452.
- (21) Takahashi, Y.; Shevchuk, A. I.; Novak, P.; Murakami, Y.; Shiku, H.; Korchev, Y. E.; Matsue, T. *J. Am. Chem. Soc.* **2010**, *132* (29), 10118–10126.
- (22) Nebel, M.; Neugebauer, S.; Eckhard, K.; Schuhmann, W. *Electrochem. commun.* **2013**, *27*, 160–163.
- (23) Shao, Y.; Mirkin, M. V.; Fish, G.; Kokotov, S.; Palanker, D.; Lewis, A. *Anal. Chem.* **1997**, *69* (8), 1627–1634.
- (24) Katemann, B.; Schuhmann, W. *Electroanalysis* **2002**, *14* (1), 22–28.
- (25) Perry, D.; Momotenko, D.; Lazenby, R. A.; Kang, M.; Unwin, P. R. *Anal. Chem.* **2016**, *88* (10), 5523–5530.
- (26) Meloni, G. N.; Bertotti, M. *Electroanalysis* **2016**, 1–8.
- (27) Carneiro, J. F.; Trevelin, L. C.; Lima, A. S.; Meloni, G. N.; Bertotti, M.; Hammer, P.; Bertazzoli, R.; Lanza, M. R. V. *Electrocatalysis* **2017**, *8* (3), 189–195.
- (28) Ventosa, E.; Schuhmann, W. *Phys. Chem. Chem. Phys.* **2015**, *17* (43), 28441–28450.
- (29) Ustarroz, J.; Kang, M.; Bullions, E.; Unwin, P. R. *Chem. Sci.* **2016**, *8*, 1841–1853.
- (30) Mauzeroll, J.; Bard, A. J. *Proc. Natl. Acad. Sci. U. S. A.* **2004**, *101* (21), 7862–7867.
- (31) Koley, D.; Bard, A. J. *Proc. Natl. Acad. Sci.* **2012**, *109* (29), 11522–11527.
- (32) Paixão, T. R. L. C.; Bertotti, M. *Quim. Nova* **2009**, *32* (5), 1306–1314.
- (33) Bond, A. M.; Oldham, K. B.; Zoski, C. G. *Anal. Chim. Acta* **1989**, *216*, 177–230.
- (34) Oldham, K. B.; Zoski, C. G. *J. Electroanal. Chem.* **1988**, *256* (1), 11–19.
- (35) Stulik, K.; Amatore, C.; Holub, K.; Marecek, V.; Kutner, W. *Pure Appl. Chem.* **2000**, *72* (8), 1483–1492.
- (36) Zoski, C. G.; Mirkin, M. V. *Anal. Chem.* **2002**, *74* (9), 1986–1992.
- (37) Amphlett, J. L.; Denuault, G. *J. Phys. Chem. B* **1998**, *102*, 9946–9951.
- (38) Cornut, R.; Lefrou, C. *J. Electroanal. Chem.* **2007**, *604* (2), 91–100.

- (39) Kwak, J.; Bard, A. J. *Anal. Chem.* **1989**, *61* (11), 1221–1227.
- (40) Bard, A. J.; Mirkin, M. V.; Unwin, P. R.; Wipf, D. O. *J. Phys. Chem.* **1992**, *96* (4), 1861–1868.
- (41) Cornut, R.; Lefrou, C. *J. Electroanal. Chem.* **2007**, *608* (1), 59–66.
- (42) Sanchez-Sanchez, C. M.; Rodriguez-Lopez, J.; Bard, A. J.; Sánchez-Sánchez, C. M.; Rodríguez-López, J.; Bard, A. J. *Anal. Chem.* **2008**, *80* (9), 3254–3260.
- (43) Eckhard, K.; Chen, X.; Turcu, F.; Schuhmann, W. *Phys. Chem. Chem. Phys.* **2006**, *8* (45), 5359–5365.
- (44) McKelvey, K.; Nadappuram, B. P.; Actis, P.; Takahashi, Y.; Korchev, Y. E.; Matsue, T.; Robinson, C.; Unwin, P. R. *Anal. Chem.* **2013**, *85* (15), 7519–7526.
- (45) Meloni, G. N.; Bertotti, M. *Electroanalysis* **2017**, *29* (3), 787–793.
- (46) Shevchuk, A. I.; Frolenkov, G. I.; Sánchez, D.; James, P. S.; Freedman, N.; Lab, M. J.; Jones, R.; Klenerman, D.; Korchev, Y. E. *Angew. Chemie Int. Ed.* **2006**, *45* (14), 2212–2216.
- (47) Rheinlaender, J.; Geisse, N. a.; Proksch, R.; Schäffer, T. E. *Langmuir* **2011**, *27* (2), 697–704.
- (48) Seifert, J.; Rheinlaender, J.; Novak, P.; Korchev, Y. E.; Schäffer, T. E. *Langmuir* **2015**, *31* (24), 6807–6813.
- (49) Sa, N.; Baker, L. a. *J. Am. Chem. Soc.* **2011**, *133* (27), 10398–10401.
- (50) Momotenko, D.; Girault, H. H. *J. Am. Chem. Soc.* **2011**, *133* (37), 14496–14499.
- (51) Chen, C.-C.; Zhou, Y.; Baker, L. a. *Annu. Rev. Anal. Chem.* **2012**, *5* (1), 207–228.
- (52) Santos, C. S.; Lima, A. S.; Battistel, D.; Daniele, S.; Bertotti, M. *Electroanalysis* **2016**, *28* (7), 1441–1447.
- (53) Nadappuram, B. P.; McKelvey, K.; Byers, J. C.; Güell, A. G.; Colburn, A. W.; Lazenby, R. A.; Unwin, P. R. *Anal. Chem.* **2015**, *87* (7), 3566–3573.
- (54) Momotenko, D.; Page, A.; Adobes-Vidal, M.; Unwin, P. R. *ACS Nano* **2016**, *10* (9), 8871–8878.
- (55) Ebejer, N.; Güell, A. G.; Lai, S. C. S.; McKelvey, K.; Snowden, M. E.; Unwin, P. R. *Annu. Rev. Anal. Chem. (Palo Alto, Calif.)* **2013**, *6*, 329–351.
- (56) Zhao, G.; Giolando, D. M.; Kirchhoff, J. R. *Anal. Chem.* **1995**, *67* (8), 1491–1495.
- (57) Thakar, R.; Weber, A. E.; Morris, C. A.; Baker, L. A. *Analyst* **2013**, *138* (20), 5973–5982.
- (58) Lima, A. S.; Meloni, G. N.; Bertotti, M. *Electroanalysis* **2013**, *25* (6), 1395–1399.

- (59) Hengstenberg, a; Kranz, C.; Schuhmann, W. *Chemistry* **2000**, 6 (9), 1547–1554.
- (60) Holder, M. N.; Gardner, C. E.; Macpherson, J. V.; Unwin, P. R. *J. Electroanal. Chem.* **2005**, 585 (1), 8–18.
- (61) Macpherson, J. V.; Unwin, P. R. *Anal. Chem.* **2000**, 72 (2), 276–285.
- (62) Ossola, D.; Dorwling-Carter, L.; Dermutz, H.; Behr, P.; Vörös, J.; Zambelli, T. *Phys. Rev. Lett.* **2015**, 115 (23), 238103.
- (63) Hirt, L.; Grüter, R. R.; Berthelot, T.; Cornut, R.; Vörös, J.; Zambelli, T. *RSC Adv.* **2015**, 5 (103), 84517–84522.
- (64) Lee, C.; Wipf, D. O.; Bard, A. J.; Bartels, K.; Bovik, A. C. *Anal. Chem.* **1991**, 63 (21), 2442–2447.
- (65) Newbury, D. E.; Ritchie, N. W. M. *J. Anal. At. Spectrom.* **2013**, 28 (7), 973–988.
- (66) Minkoff, I. *J. Mater. Sci.* **1967**, 2 (4), 388–394.
- (67) Nogala, W.; Velmurugan, J.; Mirkin, M. V. *Anal. Chem.* **2012**, 84 (12), 5192–5197.
- (68) Nadappuram, B. P.; McKelvey, K.; Al Botros, R.; Colburn, A. W.; Unwin, P. R. *Anal. Chem.* **2013**, 85 (17), 8070–8074.
- (69) Karhanek, M.; Kemp, J. T.; Pourmand, N.; Davis, R. W.; Webb, C. D. *Nano Lett.* **2005**, 5 (2), 403–407.
- (70) Yuill, E. M.; Shi, W.; Poehlman, J.; Baker, L. A. *Anal. Chem.* **2015**, 87 (22), 11182–11186.
- (71) Mirkin, M. V.; Bard, A. J. *Anal. Chem.* **1992**, 64 (19), 2293–2302.
- (72) Lazenby, R. A.; McKelvey, K.; Peruffo, M.; Baghdadi, M.; Unwin, P. R. *J. Solid State Electrochem.* **2013**, 17 (12), 2979–2987.
- (73) MakerBot 2+ Specification <https://ultimaker.com/en/products/ultimaker-2-plus/specifications>.
- (74) Dhankani, K. C.; Pearce, J. M. *HardwareX* **2016**, No. July.
- (75) Keating, S. J.; Gariboldi, M. I.; Patrick, W. G.; Sharma, S.; Kong, D. S.; Oxman, N. **2016**, 1–12.
- (76) Leigh, S. J.; Bradley, R. J.; Pursell, C. P.; Billson, D. R.; Hutchins, D. A. *PLoS One* **2012**, 7 (11), e49365.
- (77) Morgan, A. J. L.; Hidalgo, L.; Jose, S.; Jamieson, W. D.; Wymant, M.; Song, B.; Stephens, P.; Barrow, D. A.; Castell, O. K. **2016**, 1–17.
- (78) Capel, A. J.; Edmondson, S.; Christie, S. D. R.; Goodridge, R. D.; Bibb, R. J.; Thurstans, M. *Lab Chip* **2013**, 13 (23), 4583.
- (79) Kitson, P. J.; Glatzel, S.; Chen, W.; Lin, C.-G.; Song, Y.-F.; Cronin, L. *Nat. Protoc.* **2016**, 11 (5), 920–936.

- (80) He, Y.; Wu, Y.; Fu, J. Z.; Gao, Q.; Qiu, J. J. *Electroanalysis* **2016**, 28 (8), 1658–1678.
- (81) Sim, S.; Tan, Y. Y.; Lai, M. A.; Tso, C. P.; Lim, W. K. **2010**, 238 (August 2009), 44–56.
- (82) Proto-pasta conductive PLA <https://www.proto-pasta.com/pages/conductive-pla>.
- (83) Conductive Tabs, Tapes & Sheets Comparison Table https://www.tedpella.com/adhesive_html/conductive-tapes-comparison.htm.
- (84) Clausmeyer, J.; Schuhmann, W. *TrAC Trends Anal. Chem.* **2016**, 79, 46–59.
- (85) O’Connell, M. A.; Lewis, J. R.; Wain, A. J. *Chem. Commun.* **2015**, 51 (51), 10314–10317.
- (86) Chen, C.-C.; Baker, L. a. *Analyst* **2011**, 136 (1), 90–97.
- (87) Klein, T.; Buhr, E.; Georg Frase, C. In *Advances in Imaging and Electron Physics*; Elsevier Inc., 2012; Vol. 171, pp 297–356.
- (88) Sato, S.; Gondo, D.; Wada, T.; Kanehashi, S.; Nagai, K. *J. Appl. Polym. Sci.* **2013**, 129 (3), 1607–1617.
- (89) Jones, D. P. *Antioxid. Redox Signal.* **2006**, 8 (9–10), 1865–1879.
- (90) Ballatori, N.; Krance, S. M.; Marchan, R.; Hammond, C. L. *Mol. Aspects Med.* **2009**, 30 (1–2), 13–28.
- (91) N. Ballatori. *Adv. Pharmacol.* **1994**, 27, 271–298.
- (92) H. Sies. In *Oxidative Stress*; Seis, H., Ed.; Academic Press: London, 1985; pp 1–8.
- (93) Agnez-Lima, L. F.; Melo, J. T. a; Silva, A. E.; Oliveira, A. H. S.; Timoteo, A. R. S.; Lima-Bessa, K. M.; Martinez, G. R.; Medeiros, M. H. G.; Di Mascio, P.; Galhardo, R. S.; Menck, C. F. M. *Mutat. Res.* **2012**, 751, 15–28.
- (94) Conlan, X. a; Stupka, N.; McDermott, G. P.; Francis, P. S.; Barnett, N. W. *Biomed. Chromatogr.* **2010**, 24 (5), 455–457.
- (95) Ferin, R.; Pavão, M. L.; Baptista, J. J. *Chromatogr. B. Analyt. Technol. Biomed. Life Sci.* **2012**, 911, 15–20.
- (96) Squellerio, I.; Caruso, D.; Porro, B.; Veglia, F.; Tremoli, E.; Cavalca, V. J. *Pharm. Biomed. Anal.* **2012**, 71, 111–118.
- (97) Lee, P. T.; Compton, R. G. *Electroanalysis* **2013**, 25 (7), 1613–1620.
- (98) Lee, P. T.; Ward, K. R.; Tschulik, K.; Chapman, G.; Compton, R. G. *Electroanalysis* **2014**, 26 (2), 366–373.
- (99) De Cássia Silva Luz, R.; Damos, F. S.; Gandra, P. G.; De MacEdo, D. V.; Tanaka, A. A.; Kubota, L. T. *Anal. Bioanal. Chem.* **2007**, 387 (5), 1891–1897.
- (100) Gong, K.; Zhu, X.; Zhao, R.; Xiong, S.; Mao, L.; Chen, C. *Anal. Chem.* **2005**, 77

- (24), 8158–8165.
- (101) Hou, Y.; Ndamanisha, J. C.; Guo, L. ping; Peng, X. juan; Bai, J. *Electrochim. Acta* **2009**, *54* (26), 6166–6171.
- (102) Ruiz-Díaz, J. J. J.; Torriero, A. A. J.; Salinas, E.; Marchevsky, E. J.; Sanz, M. I.; Raba, J. *Talanta* **2006**, *68* (4), 1343–1352.
- (103) Xu, F.; Wang, L.; Gao, M.; Jin, L.; Jin, J. *Anal. Bioanal. Chem.* **2002**, *372* (7–8), 791–794.
- (104) Oztekin, Y.; Ramanaviciene, A.; Ramanavicius, A. *Electroanalysis* **2011**, *23* (3), 701–709.
- (105) Zaidi, S. A.; Shin, J. H. *Anal. Methods* **2016**, *8*, 1745–1754.
- (106) Wang, Y.; Jiang, L.; Chu, L.; Liu, W.; Wu, S.; Wu, Y.; He, X.; Wang, K. *Biosens. Bioelectron.* **2017**, *87*, 459–465.
- (107) Lee, P. T.; Goncalves, L. M.; Compton, R. G. *Sensors Actuators, B Chem.* **2015**, *221*, 962–968.
- (108) Zhao, L.; Zhao, L.; Miao, Y.; Zhang, C. *Electrochim. Acta* **2016**, *206*, 86–98.
- (109) Wang, Z.; Han, P.; Mao, X.; Yin, Y.; Cao, Y. *Sensors Actuators B Chem.* **2017**, *238*, 325–330.
- (110) Wang, Y.; Jiang, L.; Leng, Q.; Wu, Y.; He, X.; Wang, K. *Biosens. Bioelectron.* **2016**, *77*, 914–920.
- (111) Harfield, J. C.; Batchelor-McAuley, C.; Compton, R. G. *Analyst* **2012**, *137* (10), 2285–2296.
- (112) White, P. C.; Lawrence, N. S.; Davis, J.; Compton, R. G. *Electroanalysis* **2002**, *14* (2), 89.
- (113) Lowinsohn, D.; Lee, P. T.; Compton, R. G. *J. Braz. Chem. Soc.* **2014**, *25* (9), 1614–1620.
- (114) Mauzeroll, J.; Schougaard, S. In *Scanning Electrochemical Microscopy*; Press, C., Ed.; 2012; pp 379–411.
- (115) Bergner, S.; Vatsyayan, P.; Matysik, F.-M. *Anal. Chim. Acta* **2013**, *775*, 1–13.
- (116) Schulte, A.; Schuhmann, W. *Angew. Chemie Int. Ed.* **2007**, *46* (46), 8760–8777.
- (117) Sun, P.; Laforge, F. O.; Abeyweera, T. P.; Rotenberg, S. a; Carpino, J.; Mirkin, M. V. *Proc. Natl. Acad. Sci. U. S. A.* **2008**, *105* (2), 443–448.
- (118) Mauzeroll, J.; Bard, A. J.; Owhadian, O.; Monks, T. J. *Proc. Natl. Acad. Sci. U. S. A.* **2004**, *101* (51), 17582–17587.
- (119) Liljeroth, P.; Johans, C.; Slevin, C. J.; Quinn, B. M.; Kontturi, K. *Electrochem. commun.* **2002**, *4* (1), 67–71.
- (120) Harvey, S. L. R.; Coxon, P.; Bates, D.; Parker, K. H.; O'Hare, D. *Sensors*

- Actuators B Chem.* **2008**, *129* (2), 659–665.
- (121) Kim, L. T. T.; Girard, A.; Griscom, L.; Razan, F.; Griveau, S.; Bedioui, F. *Electrochem. commun.* **2011**, *13* (7), 681–684.
- (122) Liljeroth, P.; Johans, C.; Slevin, C. J.; Quinn, B. M.; Kontturi, K. *Anal. Chem.* **2002**, *74* (9), 1972–1978.
- (123) Harvey, S. L. R.; Parker, K. H.; O'Hare, D. *J. Electroanal. Chem.* **2007**, *610* (2), 122–130.
- (124) Bard, A. J.; Denuault, G.; Lee, C.; Mandler, D.; Wipf, D. O. *Acc. Chem. Res.* **1990**, *23* (5), 357–363.
- (125) Sánchez-Sánchez, C. M.; Rodríguez-López, J.; Bard, A. J. *Anal. Chem.* **2008**, *80* (9), 3254–3260.
- (126) Paixão, T. R. L. C.; Matos, R. C.; Bertotti, M. *Talanta* **2003**, *61* (5), 725–732.
- (127) Tomčík, P.; Mesároš, Š.; Bustin, D. *Anal. Chim. Acta* **1998**, *374* (2–3), 283–289.
- (128) Smirnov, W.; Kriele, A.; Hoffmann, R.; Sillero, E.; Hees, J.; Williams, O. A.; Yang, N.; Kranz, C.; Nebel, C. E. *Anal. Chem.* **2011**, *83* (12), 4936–4941.
- (129) Oja, S. M.; Fan, Y.; Armstrong, C. M.; Defnet, P.; Zhang, B. *Anal. Chem.* **2015**, 10.1021/acs.analchem.5b04542.
- (130) Yu, Y.; Gao, Y.; Hu, K.; Blanchard, P.-Y.; Noël, J.-M.; Nareshkumar, T.; Phani, K. L.; Friedman, G.; Gogotsi, Y.; Mirkin, M. V. *ChemElectroChem* **2015**, *2* (1), 58–63.
- (131) Zhang, Y.; Clausmeyer, J.; Babakinejad, B.; López Córdoba, A.; Ali, T.; Shevchuk, A.; Takahashi, Y.; Novak, P.; Edwards, C.; Lab, M.; Gopal, S.; Chiappini, C.; Anand, U.; Magnani, L.; Coombes, R. C.; Gorelik, J.; Matsue, T.; Schuhmann, W.; Klenerman, D.; Sviderskaya, E. V.; Korchev, Y. *ACS Nano* **2016**, acsnano.5b05211.
- (132) Zhang, W.; Zhu, S.; Luque, R.; Han, S.; Hu, L.; Xu, G. *Chem. Soc. Rev.* **2016**, 10.1039/c5cs00297d.
- (133) Hao, R.; Zhang, B. *Anal. Chem.* **2015**, 10.1021/acs.analchem.5b03548.
- (134) Fu-Ren F. Fan and Christophe Demaille. In *Scanning Electrochemical Microscopy*; Bard, Allen J., Mirkin, M. V., Ed.; CRC Press: Boca Raton, 2012; pp 25–51.
- (135) Yu, Y.; Noël, J.-M.; Mirkin, M. V.; Gao, Y.; Mashtalir, O.; Friedman, G.; Gogotsi, Y. *Anal. Chem.* **2014**, *86* (7), 3365–3372.
- (136) Weber, A. E.; Baker, L. A. *J. Electrochem. Soc.* **2014**, *161* (14), H924–H929.
- (137) Yuill, E. M.; Sa, N.; Ray, S. J.; Hieftje, G. M.; Baker, L. A. *Anal. Chem.* **2013**, *85* (18), 8498–8502.
- (138) Wang, Y.; Alsmeyer, D. C.; McCreery, R. L. *Chem. Mater.* **1990**, *2* (5), 557–563.

- (139) Wang, Y.; Serrano, S.; Santiago-Aviles, J. J. *Synth. Met.* **2003**, *138*, 423–427.
- (140) Ranganathan, S.; McCreery, R.; Majji, S. M.; Madou, M. *J. Electrochem. Soc.* **2000**, *147* (1), 277.
- (141) Chen, R.; Hu, K.; Yu, Y.; Mirkin, M. V.; Amemiya, S. *J. Electrochem. Soc.* **2016**, *163* (4), H3032–H3037.
- (142) Sun, P.; Mirkin, M. V. *Anal. Chem.* **2007**, *79* (15), 5809–5816.
- (143) Nioradze, N.; Chen, R.; Kim, J.; Shen, M.; Santhosh, P.; Amemiya, S. *Anal. Chem.* **2013**, *85*, 6198–6202.
- (144) Korchev, Y. E.; Milovanovic, M.; Bashford, C. L.; Bennett, D. C.; Sviderskaya, E. V.; Vodyanoy, I.; Lab, M. J. *J. Microsc.* **1997**, *188* (Pt 1), 17–23.
- (145) Happel, P.; Hoffmann, G.; Mann, S. A.; Dietzel, I. D. *J. Microsc.* **2003**, *212* (2), 144–151.
- (146) Takahashi, Y.; Murakami, Y.; Nagamine, K.; Shiku, H.; Aoyagi, S.; Yasukawa, T.; Kanzaki, M.; Matsue, T. *Phys. Chem. Chem. Phys.* **2010**, *12* (34), 10012–10017.
- (147) Rheinlaender, J.; Schäffer, T. E. *Soft Matter* **2013**, *9* (12), 3230.
- (148) Gorelik, J.; Shevchuk, A. I.; Frolenkov, G. I.; Diakonov, I. A.; Lab, M. J.; Kros, C. J.; Richardson, G. P.; Vodyanoy, I.; Edwards, C. R. W.; Klenerman, D.; Korchev, Y. E. *Proc. Natl. Acad. Sci. U. S. A.* **2003**, *100* (10), 5819–5822.
- (149) Comstock, D. J.; Elam, J. W.; Pellin, M. J.; Hersam, M. C. *Anal. Chem.* **2010**, *82* (4), 1270–1276.
- (150) Korchev, Y. E.; Raval, M.; Lab, M. J.; Gorelik, J.; Edwards, C. R.; Rayment, T.; Klenerman, D. *Biophys. J.* **2000**, *78* (5), 2675–2679.
- (151) Gorelik, J.; Shevchuk, a; Ramalho, M.; Elliott, M.; Lei, C.; Higgins, C. F.; Lab, M. J.; Klenerman, D.; Krauzewicz, N.; Korchev, Y. *Proc. Natl. Acad. Sci. U. S. A.* **2002**, *99* (25), 16018–16023.
- (152) Salles, M. O.; Meloni, G. N.; de Araujo, W. R.; Paixão, T. R. L. C. *Anal. Methods* **2014**, *6* (7), 2047–2052.
- (153) Wang, Y.; Kececi, K.; Velmurugan, J.; Mirkin, M. V. *Chem. Sci.* **2013**, *4* (9), 3606–3616.
- (154) Williams, C. G.; Edwards, M. A.; Colley, A. L.; Macpherson, J. V.; Unwin, P. R. *Anal. Chem.* **2009**, *81* (7), 2486–2495.
- (155) Takahashi, Y.; Kumatani, A.; Munakata, H.; Inomata, H.; Ito, K.; Ino, K.; Shiku, H.; Unwin, P. R.; Korchev, Y. E.; Kanamura, K.; Matsue, T. *Nat. Commun.* **2014**, *5*, 5450.
- (156) McKelvey, K.; Perry, D.; Byers, J. C.; Colburn, A. W.; Unwin, P. R. *Anal. Chem.* **2014**, *86* (V), 3639–3646.

- (157) McKelvey, K.; Kinnear, S. L.; Perry, D.; Momotenko, D.; Unwin, P. R. *J. Am. Chem. Soc.* **2014**, *136* (39), 13735–13744.
- (158) Perry, D.; Al Botros, R.; Momotenko, D.; Kinnear, S. L.; Unwin, P. R. *ACS Nano* **2015**, *9* (7), 7266–7276.
- (159) Proksch, R.; Lal, R.; Hansma, P. K.; Morse, D.; Stucky, G. *Biophys. J.* **1996**, *71* (4), 2155–2157.
- (160) Chen, C. C.; Derylo, M. A.; Baker, L. A. *Anal. Chem.* **2009**, *81* (12), 4742–4751.
- (161) Zhou, Y.; Chen, C. C.; Baker, L. A. *Anal. Chem.* **2012**, *84* (6), 3003–3009.
- (162) Prater, C. B.; Hansma, P. K.; Tortonese, M.; Quate, C. F. *Rev. Sci. Instrum.* **1991**, *62* (11), 2634–2638.
- (163) Dmitry Momotenko, Fernando Cortés-Salazar, Jacques Josserand, Shujuan Liu, Yuanhua Shao, H. H. G. *Phys.Chem.Chem.Phys.* **2011**, *13*, 5430–5440.
- (164) Wei, C.; Bard, A. J.; Feldberg, S. W. *Anal. Chem.* **1997**, *69* (22), 4627–4633.
- (165) Sa, N.; Lan, W. J.; Shi, W.; Baker, L. A. *ACS Nano* **2013**, *7* (12), 11272–11282.
- (166) Szentirmay, M. N.; Martin, C. R. *Anal. Chem.* **1984**, *56*, 1898–1902.
- (167) Shevchuk, A. I.; Gorelik, J.; Harding, S. E.; Lab, M. J.; Klenerman, D.; Korchev, Y. E. *Biophys. J.* **2001**, *81* (3), 1759–1764.
- (168) Li, C.; Johnson, N.; Ostanin, V.; Shevchuk, A.; Ying, L.; Korchev, Y.; Klenerman, D. *Prog. Nat. Sci.* **2008**, *18* (6), 671–677.
- (169) Kim, J.; Shen, M.; Nioradze, N.; Amemiya, S. *Anal. Chem.* **2012**, *84* (8), 3489–3492.
- (170) Laslau, C.; Williams, D. E.; Wright, B. E.; Travas-Sejdic, J. *J. Am. Chem. Soc.* **2011**, *133* (15), 5748–5751.
- (171) Edwards, M. a.; Williams, C. G.; Whitworth, A. L.; Unwin, P. R. *Anal. Chem.* **2009**, *81* (11), 4482–4492.
- (172) Guerrette, J. P.; Zhang, B. **2010**, 17088–17091.
- (173) Chen, C. H.; Jacobse, L.; McKelvey, K.; Lai, S. C. S.; Koper, M. T. M.; Unwin, P. R. *Anal. Chem.* **2015**, *87* (11), 5782–5789.
- (174) Aldous, L.; Compton, R. G. *Phys. Chem. Chem. Phys.* **2011**, *13* (12), 5279–5287.
- (175) Wittstock, G.; Burchardt, M.; Pust, S. E.; Shen, Y.; Zhao, C. *Angew. Chemie - Int. Ed.* **2007**, *46* (10), 1584–1617.
- (176) Burt, D. P.; Wilson, N. R.; Janus, U.; Macpherson, J. V.; Unwin, P. R. *Langmuir* **2008**, *24* (17), 12867–12876.
- (177) Momotenko, D.; Byers, J. C.; McKelvey, K.; Kang, M.; Unwin, P. R. *ACS Nano* **2015**, *9* (9), 8942–8952.

- (178) Resnick, M.; Berg, R.; Eisenberg, M. *J. Learn. Sci.* **2000**, 9 (1), 7–30.
- (179) Kubínová, Š.; Šlégr, J. *J. Chem. Educ.* **2015**, 92 (10), 1751–1753.
- (180) McClain, R. *J. Chem. Educ.* **2014**, 91, 747–750.
- (181) Mabbott, G. A. *J. Chem. Educ.* **2014**, 91 (9), 1458–1463.
- (182) Urban, P. L. *J. Chem. Educ.* **2014**, 91 (5), 751–752.
- (183) Mott, J. R.; Munson, P. J.; Kreuter, R. a.; Chohan, B. S.; Sykes, D. G. *J. Chem. Educ.* **2014**, 91 (7), 1028–1036.
- (184) Rowe, A. a.; Bonham, A. J.; White, R. J.; Zimmer, M. P.; Yadgar, R. J.; Hobza, T. M.; Honea, J. W.; Ben-Yaacov, I.; Plaxco, K. W. *PLoS One* **2011**, 6 (9).
- (185) Bard, A. J.; Faulkner, L. R. *Electrochemical methods : fundamentals and applications*; 2001.
- (186) LM324 datasheet <http://www.ti.com/lit/ds/symlink/lm324.pdf>.
- (187) Arduino Playground - PwmFrequency
<http://playground.arduino.cc/Code/PwmFrequency> (accessed Aug 24, 2015).
- (188) Scherz, P. Practical Electronics for Inventors
[http://www.ee.iitb.ac.in/student/~bhagwan/Basic Electrical Engineering/Practical Electronics for Inventors.pdf](http://www.ee.iitb.ac.in/student/~bhagwan/Basic%20Electrical%20Engineering/Practical%20Electronics%20for%20Inventors.pdf).
- (189) Kissinger, P. T.; Heineman, W. R. *J. Chem. Educ.* **1983**, 60 (9), 702.
- (190) Stackelberg, M. V. *Zeitschrift für Elektrochemie, Berichte der Bunsengesellschaft für Phys. Chemie* **1953**, 57 (5), 338–342.
- (191) Flaxer, E.; Academic, A. T. *Education* **2010**, 1280–1286.
- (192) Gerritsen, J. W.; Boon, E. J. G.; Janssens, G.; Van, H. *Appl. Phys. A Mater. Sci. Process.* **1998**, 66 (7), S79–S82.
- (193) Famularo, N.; Kholod, Y.; Kosenkov, D. *J. Chem. Educ.* **2016**, 93 (1), 175–181.
- (194) Meloni, G. N. *J. Chem. Educ.* **2016**, 93 (7), 1320–1322.
- (195) Sun, P.; Mirkin, M. V. *Anal. Chem.* **2006**, 78 (18), 6526–6534.
- (196) Lefrou, C.; Cornut, R. *ChemPhysChem* **2010**, 11 (3), 547–556.
- (197) Santana, J. J.; González-Guzmán, J.; Fernández-Mérida, L.; González, S.; Souto, R. M. *Electrochim. Acta* **2010**, 55 (15), 4488–4494.
- (198) Macpherson, J. V.; Slevin, C. J.; Unwin, P. R. *J. Chem. Soc. Faraday Trans.* **1996**, 92 (20), 3799.
- (199) Xiong, H.; Guo, J.; Amemiya, S. *Anal. Chem.* **2007**, 79 (7), 2735–2744.
- (200) Sklyar, O.; Wittstock, G. *J. Phys. Chem. B* **2002**, 106 (30), 7499–7508.
- (201) Oja, S. M.; Fan, Y.; Armstrong, C. M.; Defnet, P.; Zhang, B. *Anal. Chem.* **2016**,

88 (1), 414–430.

(202) Lazenby, R. A.; McKelvey, K.; Unwin, P. R. *Anal. Chem.* **2013**, 85 (5), 2937–2944.

(203) Nebel, M.; Eckhard, K.; Erichsen, T.; Schulte, A.; Schuhmann, W. *Anal. Chem.* **2010**, 82 (18), 7842–7848.